National Renewable Energy Laboratory
Innovation for Our Energy Future

A national laboratory of the U.S. Department of Energy
Office of Energy Efficiency & Renewable Energy

Efficiency Improvement of Crystalline Solar Cells

Final Subcontract Report
1 January 2002 – 30 September 2006

E.R. Weber
University of California, Berkeley
Berkeley, California

Subcontract Report
NREL/SR-520-42323
November 2007

NREL is operated by Midwest Research Institute • Battelle Contract No. DE-AC36-99-GO10337

Efficiency Improvement of Crystalline Solar Cells

Final Subcontract Report
1 January 2002 – 30 September 2006

E.R. Weber
University of California, Berkeley
Berkeley, California

NREL Technical Monitor: R. Matson/F. Posey-Eddy

Prepared under Subcontract No. AAT-2-31605-03

Subcontract Report
NREL/SR-520-42323
November 2007

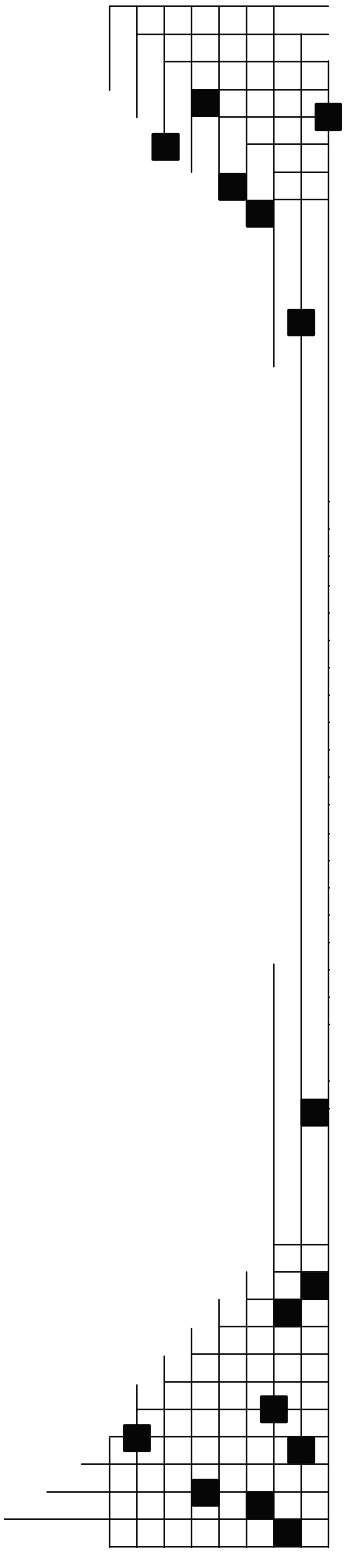

National Renewable Energy Laboratory
1617 Cole Boulevard, Golden, Colorado 80401-3393
303-275-3000 • www.nrel.gov

Operated for the U.S. Department of Energy
Office of Energy Efficiency and Renewable Energy
by Midwest Research Institute • Battelle

Contract No. DE-AC36-99-GO10337

Table of Contents

List of Figures

List of Tables

A. Motivation And Objectives of Research

Crystalline silicon (c-Si) accounts for over 90% of the total photovoltaic (PV) production worldwide and fuels the average 30% industry-wide growth rate. According to P. Maycock's PV News newsletter, in 2005 the worldwide PV industry grew 44% and reached an estimated 1.7 GW_p of installed capacity. Solar cells produced from high-purity single-crystalline silicon have achieved nearly 25% laboratory efficiencies; high-purity multicrystalline silicon (mc-Si) material has achieved about 20% record efficiency, whereas mc-Si produced from lower-quality feedstock, although much cheaper, typically results in solar cells with efficiencies between 12-15%. To be competitive on the energy market dominated by hydroelectric, nuclear, and fossil fuel power plants, the price per kWh of the installed PV modules should continue decreasing. To achieve the lowest possible production cost combined with acceptable efficiency, many PV companies prefer to work with the low-cost mc-Si, cognizant that the loss of efficiency relative to single-crystalline silicon is offset by the lower production cost of solar cells.

The lower efficiency of mc-Si solar cells is caused by the presence of impurities and structural defects, which severely degrade the electrical properties of the material. If control over efficiency-limiting defects in mc-Si were to be achieved without substantially raising the production costs, then a significant reduction of cost per kWh could be realized. Such an improvement would further increase the competitive advantage of mc-Si, hastening the introduction of PV into the mainstream energy market. A formidable challenge to removing or passivating efficiency-limiting defects, especially metal-related ones, lies in the fact that, until very recently, a comprehensive understanding of metals' chemical state, distribution, and impact on cell efficiency was lacking. This was mainly because these defects can be very small (often tens or hundreds of nanometers in size) and separated by comparatively large distances (often several microns), making their study very challenging for conventional analytical techniques.

The objective of this subcontract was to gain fundamental physical understanding of the transition metal related defects in PV-grade multicrystalline silicon through elucidating the pathways of their introduction into solar cells, their chemical state and distribution within mc-Si, and their interaction with structural defects. The further objective was to assess the possibilities of reduction of detrimental impact of these defect clusters on the cell performance via defect engineering.

B. Approach

The approach used in this subcontract was to use unique analytical tools available at Berkeley, at other National Laboratories, and at research institutions involved in solar cell research to perform systematic fundamental physical studies of distribution and chemical state of metal clusters in a variety of multicrystalline silicon materials.

Two analytical techniques were essential for the success of this project. The total metal concentration in the areas of multicrystalline silicon with high and low lifetime was determined by Neutron Activation Analysis (NAA), the technique which involves irradiation of the samples with neutrons in a nuclear reactor and analysis of its residual radioactivity. The distribution and chemical state of metal clusters was characterized by synchrotron radiation based x-ray microscopes available at the Advanced Light Source (Beamlines 10.3.1 and 10.3.2) at Lawrence Berkeley National Laboratory and Advanced Photon Source (Beamlines 2-ID-D and 20-ID-B) at Argonne National Laboratory. At these beamlines, x-rays can be focused into spot sizes from 200 nm to 5 μm in diameter (depending on the beamline). A small beam size, high flux, and ultra-low Bremsstrahlung background allow one to achieve the high sensitivity necessary to detect very small metal clusters. For example, for experimental conditions with a 200 nm diameter beam and an accumulation time of 1 second, we have detected iron silicide clusters of radius 23±5 nm, while the noise-limited detection limit for the same conditions was estimated to be 16±3 nm. After metal-rich clusters of interest were located via microprobe x-ray fluorescence (μ-XRF), their chemical state (e.g., oxide vs silicide) was assessed via X-ray absorption microspectroscopy (μ-XAS). By using a monochromator to vary the energy of the X-ray beam with an energy resolution of 1 eV or better, the X-ray absorption spectrum of the metal particle was compared against the absorption spectra of commercially available standard materials such as metal-oxides or metal-silicides. Recombination activity of metal clusters could be assessed by in-situ x-ray beam induced current measurements (XBIC).

We analyzed and compared mc-Si materials grown using different technologies, including samples of sheet, cast, and ribbon-grown mc-Si, as well as multicrystalline silicon grown by the float zone technique at NREL. From these data, we were able to identify statistically meaningful trends, those material-specific as well as those generic to all mc-Si materials, in the distribution and properties of metal clusters, and their response to heat treatments and gettering.

The success of this project owes to numerous discussions at NREL crystalline silicon solar cells workshops, DOE program review meetings, IEEE and European photovoltaic conferences. Collaboration with various solar cell companies and research institutes helped us to obtain precharacterized samples of as-grown mc-Si materials and processed solar cells. The list below, which is not necessarily complete, lists some of the collaborations with partner institutes and companies:

Evergreen Solar – provided samples of string ribbon silicon for analysis with synchrotron x-ray techniques to identify locations and density of metal clusters and to compare string ribbons with other mc-Si materials.

RWE Schott Solar – provided samples of production quality EFG silicon for neutron activation analysis and for XRF analyses of distribution and sizes of metal clusters. Many helpful

discussions with Juris Kalejs helped us with interpretation of our results and helped to define future directions of work.

Astropower (currently **GE Energy**) – provided samples of sheet material for neutron activation analyses. Their samples were also used in our study of origins and preferred chemical states of iron and copper in mc-Si and in comparative analysis of metal clusters in various mc-Si materials. Some of these samples were precharacterized by EBIC at North Carolina State University.

BP Solar – provided samples of cast mc-Si silicon for XRF analyses.

Renewable Energy Corporation, Norway – provided a set of cast mc-Si sister-wafers which included as-grown, P-gettered, hydrogen passivated, and P-gettered and hydrogen passivated samples to compare how the distribution of metal clusters changes during these processing steps.

Deutsche Solar, Germany (former **Bayer Solar AG**) – offered samples of cast mc-Si for neutron activation analyses and provided samples of cast mc-Si from different areas of the ingot used to clarify the pathways of introduction of metals into silicon ingots.

ECN Solar Energy (the Netherlands) – provided us through the University of Konstanz samples of processed and precharacterized with thermography RGS material for study of shunts in mc-Si solar cells.

Sumco USA provided samples of polysilicon deposited on top of single crystalline CZ wafers which were used for our analyses of relaxation and segregation gettering of iron in mc-Si. It was found that gettering of iron by polysilicon has both segregation and relaxation component. This confirms that grain boundaries in mc-Si provide significant reservoirs for transition metals, which can be removed only by segregation gettering at high temperatures.

NREL provided us with clean and metal contaminated mc-Si FZ samples grown by T.F.Ciszek.

North Carolina State University – group of Prof. G.Rozgonyi provided us sheet mc-Si material pre-characterized with EBIC, performed microwave PCD mapping on cast mc-Si samples provided by BP Solar, and worked with us on the project on high resolution mapping of oxygen and carbon content in mc-Si samples at the ALS beamline 1.4.

Georgia Tech - Prof. A. Rohatgi's group assisted with SiN hydrogen passivation of our samples.

University of Konstanz, Germany – Dr. G. Hahn provided samples of RGS solar cells with shunts precharacterized with thermography for analyses of metal content in the shunt locations. His group processed some of our samples using their remote plasma hydrogenation equipment.

Fraunhofer ISE, Germany – offered us mc-Si sister-wafers (samples with similar defect structure sawed from adjacent areas of the ingot) which were RTA-processed for different times at different temperatures. Another set of precharacterized mc-Si samples was used for development of SR-XBIC.

MPI Halle, Germany – shared with us data on SiC precipitates in cast mc-Si ingots which helped us to understand the role of crucible coating in incorporation of impurities into silicon ingots, and assisted us in the area of thermography and characterization of shunts in solar cells..

Australian National University – Dan Macdonald measured injection level dependence on samples of n-type and p-type single crystal silicon, which we used to estimate the injection level of our SR-XBIC technique, and collaborated with us on the study of injection level dependence of recombination activity of Cu precipitates in silicon.

Lawrence Berkeley National Laboratory – scientists from Advanced Light Source, Nuclear Physics Division, and National Center for Electron Microscopy guided us in our work with x-ray microscopes, FTIR system, neutron activation analyses, with the use of scanning and transmission electron microscopes, and provided access to the equipment.

Argonne National Laboratory – scientists from Advanced Photon Source assisted us with the measurements at the APS beamlines.

St.-Petersburg State University, Russia – Prof. Oleg Vyvenko participated in our first experiments at the synchrotron and initiated implementation of the XBIC technique at the XRF beamline.

Institute for Semiconductor Physics, Frankfurt-Oder, Germany, provided us samples of metal-contaminated Si/SiGe structures precharacterized with EBIC for our studies of the clustering of transition metals at misfit dislocations.

The last but not least, we would like to acknowledge the guidance and encouragement of our NREL technical monitor, Rick Matson, and well as his efforts to keep the University Crystalline Silicon Research program running.

C. Tasks of The Project And Compliance With The Expected Deliverables

The project was initially funded for three years, and then was extended for another two years. The tasks were grouped in phases as follows:

Phase 1 (1/01/2002 – 9/30/2004).
1.1. Identify the dominant metal impurities in bad regions.
1.2. Determine which metals in bad regions cannot be removed by aluminum gettering.
1.3. Compare different growth techniques in terms of metal contamination.
1.4. Determine the role of metal impurities in the formation of shunts.

Phase 2 (1/01/2002 – 9/30/2004).
2.1. Perform systematic studies of interactions of metals with lattice defects and oxygen.
2.2. Study recombination activity and thermal stability of the complexes that metals form in mc-Si.
2.3. Apply Advanced Light Source x-ray techniques to determine the chemical nature of the precipitates/agglomerates.

Phase 3 (1/01/2002 – 9/30/2004).
3.1. Identify the factors which favor the formation of the most gettering resistant clusters/precipitates.
3.2. Generate data on how the gettering/passivation resistant metal clusters are formed and how the growth process can be modified to avoid the formation of such clusters.
3.3. Compare the efficiency of gettering and SiN passivation.

Phase 4 (10/1/2004 – 6/30/2005) (Extension of the subcontract).
4.1. Develop theoretical basis for quantitative XBIC. Further, develop the quantitative XBIC technique and apply it to characterization of recombination properties of metal clusters in solar cell materials.
4.2. Apply the ALS Beamline 1.4.3 (Infrared Spectromicroscopy) to analysis of solar cell materials.
4.3. Apply quantitative XBIC to multicrystalline silicon samples and establish correlations between the local amount of metals within precipitates and degradation of minority carrier diffusion length within these precipitates.

Phase 5 (7/1/2005 – 9/30/2006) (Extension of the subcontract)
5.1. Establish correlations between feedstock quality, crystal growth parameters, spatial distribution, and chemical state of metals in multicrystalline silicon.
5.2. Investigate the feasibility of contamination of cast mc-Si from the silicon nitride crucible coating.
5.3. Investigate interaction between different metals in solar-grade multicrystalline silicon with the formation of intermetallic silicides.

During the performance period, we demonstrated 100% compliance with the goals outlined in the statements of work and contract materials, and in many cases exceeded the expectations by performing studies beyond the expected deliverables. In particular, the following additional tasks were performed and reported:

6.1. A concept of defect engineering of transition metals in multicrystalline silicon solar cells.
6.2. Segregation of metals at structural defects.
6.3. Impact of the cooling rate on metal distribution in mc-Si.
6.4. Analysis of impurity concentrations in metallurgical-grade and solar-grade silicon.

D. Publications And Presentations In Which Results Obtained With The Financial Support Through Were Published or Presented.

The results of our research were presented in 2002-2006 quarterly technical status reports and were published in the following journal articles and conference proceedings:

Journal articles

T. Buonassisi, A.A. Istratov, M.D. Pickett, M.A. Marcus, T.F. Ciszek, E.R. Weber, "Metal precipitation at grain boundaries in silicon: dependence on grain boundary character and dislocation decoration", Applied Physics Letters, **89**, no.4, pp. 42102-1-3 (2006).

A.A. Istratov, T. Buonassisi, M. D. Pickett, M. Heuer, and E.R. Weber, "Control of metal impurities in "dirty" multicrystalline silicon for solar cells", Materials Science and Engineering B, in press (2006).

M. Heuer, T. Buonassisi, M. A. Marcus, A. A. Istratov, M. D. Pickett, T. Shibata, E. R. Weber, "Identification of a complex intermetallic phase in multicrystalline silicon", Physical Review B **73**, no.23, pp. 235204-1-5 (15 June 2006).

T.Buonassisi, A.A.Istratov, M.D.Pickett, J.-P.Rakotoniaina, O.Breitenstein, M.A.Marcus, S.M.Heald, and E.R.Weber, "Transition metals in photovoltaic-grade ingot-cast multicrystalline silicon: accessing the role of impurities in silicon nitride crucible lining material", Journal of Crystal Growth 287, 402 (Jan. 2006).

T. Buonassisi, A. A. Istratov, M.D. Pickett, M. Heuer, J.P. Kalejs, G. Hahn, M.A. Marcus, B. Lai, Z. Cai, S.M. Heald, T.F. Ciszek, R.F. Clark, D.W. Cunningham, A.M. Gabor, R. Jonczyk, S. Narayanan, E. Sauar, and E. R. Weber, "Metal impurities in multicrystalline silicon materials: Similarities and differences in distribution, elemental and chemical natures", Progress in Photovoltaics (2006, in print).

T. Buonassisi, M. D. Pickett, M. A. Marcus, A. A. Istratov, G. Hahn, T. F. Ciszek, S. Riepe, J. Isenberg, W. Warta, R. Schindler, and E. R. Weber, "Quantifying the recombination activity of metal precipitates in multicrystalline silicon using synchrotron-based spectrally-resolved X-ray beam induced current", Applied Physics Letters 87, 044101 (25 July 2005).

T.Buonassisi, A.A.Istratov, S.Peters, C.Ballif, J.Isenberg, S.Riepe, W.Warta, R.Schindler, Z.Cai, B.Lai, E.R.Weber, "Impact of metal silicide precipitate dissolution during rapid thermal processing of multicrystalline silicon solar cells", Applied Physics Letters, **87**, 121918 (19 Sept 2005).

T.Buonassisi, A.A.Istratov, M.A.Marcus, B.Lai, Z.Cai, S.Heald, and E.R.Weber, "Engineering metal-impurity nanodefects for low-cost solar cells", Nature Materials **4**, 676-679 (01 Sep 2005)

T. Buonassisi, A.A. Istratov, M. Heuer, M.A. Marcus, R.Jonczyk, J.Isenberg, B. Lai, Z. Cai, S.Heald, W. Warta, R. Schindler, and E. R. Weber, "Synchrotron-based investigations of the nature and impact of iron contamination in multicrystalline silicon solar cell materials", J. Appl. Phys. **97**, 074901 (1 April 2005)

T. Buonassisi, M.A. Marcus, A.A. Istratov, M. Heuer, T. F. Ciszek, B. Lai, Z. Cai, and E.R. Weber, "Analysis of copper-rich precipitates in silicon: chemical state, gettering, and impact on multicrystalline silicon solar cell material", J.Appl.Phys. **97**, 063503 (15 March 2005)

O.F.Vyvenko, T.Buonassisi, A.A.Istratov, and E.R.Weber, "X-ray beam induced current/microprobe x-ray fluorescence: synchrotron radiation based x-ray microprobe techniques for analysis of the recombination activity and chemical nature of metal impurities in silicon", J.Phys: Condens. Matter **16**, S141-S151 (21 Jan 2004).

T.Buonassisi, O.F.Vyvenko, A.A.Istratov, E.R.Weber, G.Hahn, D.Sontag, J.P.Rakotoniaina, O.Breitenstein, J.Isenberg, and R.Schindler, "Observation of transition metals at shunt locations in multicrystalline silicon solar cells", J. Appl. Phys. **95**, no. 3, pp. 1556-1561 (February 1, 2004)

A.A.Istratov, T.Buonassisi, R.J.McDonald, A.R.Smith, R.Schindler, J.A.Rand, J.Kalejs, and E.R.Weber, "Metal content of multicrystalline solar cells and its impact on minority carrier diffusion length", J. Appl.Phys. **94**, 6552-9 (15 Nov 2003).

T. Buonassisi, M. Heuer, O.F. Vyvenko, A.A. Istratov, E.R. Weber, Z.Cai, B.Lai, T. Ciszek, and R.Schindler, "Applications of synchrotron radiation x-ray techniques on the analysis of the behavior of transition metals in solar cells and single crystalline silicon with extended defects", Physica B **340-342**, 1137-41 (31 Dec 2003).

O.F.Vyvenko, T.Buonassisi, A.A.Istratov, E.R.Weber, M.Kittler, and W.Seifert, "Application of synchrotron radiation based X-ray microprobe techniques for the analysis of recombination activity of metals precipitated at Si/SiGe misfit dislocations", Journal of Physics: Condensed Matter **14**, 13079 (16 Dec 2002).

Publications in Conference Proceedings

T. Buonassisi, M.D. Pickett, A.A. Istratov, E. Sauar, T.C. Lommasson, E. Marstein, T. Pernau, R.F. Clark, S. Narayanan, S.M. Heald, E.R. Weber, Interactions between metals and different grain boundary types and their impact on multicrystalline silicon device performance, Proc. 4th World Conference on Photovoltaic Energy Conversion (Waikoloa, Hawaii) (in press, 2006).

T. Buonassisi, A.A. Istratov, M. Heuer, M.D. Pickett, and E.R. Weber, "Distinguishing the impacts of individual metal species on multicrystalline silicon performance in a multiple metal environment", Proc. 20th European Photovoltaic Solar Energy Conference and Exhibition, Barcelona, Spain (2005).

T. Buonassisi, G. Hahn, A.M. Gabor, J. Schischka, A.A. Istratov, M.D. Pickett, and E.R. Weber, "Correlations between structural, impurity, and electrical properties in efficiency-limiting "defect bands" in string ribbon silicon", Proc. 20th European Photovoltaic Solar Energy Conference and Exhibition, Barcelona, Spain (2005).

T.Buonassisi, A.A.Istratov, M.A.Marcus, M.Heuer, M.D.Pickett, B.Lai, Z.Cai. S.M.Heald, and E.R.Weber, "Local measurements of diffusion length and chemical character of metal clusters in multicrystalline silicon", (GADEST-2005), Solid State Phenomena **108-109**, 577-584 (2005).

T. Buonassisi, A. A. Istratov, M.A. Marcus, S.Peters, C.Ballif, M.Heuer, T.F. Ciszek, Z.Cai, B.Lai, R.Schindler, E.R. Weber, "Synchrotron-based investigations into metallic impurity distribution and defect engineering in multicrystalline silicon via thermal treatments", Proc. of 31st IEEE Photovoltaic Specialists conference (IEEE, 2005).

A.A.Istratov, T.Buonassisi, R.J.McDonald, A.R.Smith, R.Schindler, J.Rand, J.P.Kalejs, and E.R.Weber, "Metal content of multicrystalline silicon for solar cells and its impact on minority carrier diffusion length", Solid State Phenomena **95-96**, 175-180 (2004) (ISBN: 3-908450-82-9).

T.Buonassisi, O.F.Vyvenko, A.A.Istratov, E.R.Weber, and R.Schinler, "Application of X-ray synchrotron techniques to the characterization of the chemical nature and recombination activity of lifetime limiting defects in solar cells", in "Defects and Impurity Engineered Semiconductors and Devices III", Edited by S. Ashok, J. Chevallier, N.M. Johnson, B.L. Sopori, and H. Okushi, MRS Symp. Proc. Vol. 719, p. 179-184 (2002).

A.A.Istratov, T.Buonassisi, M.Heuer, M.D.Pickett, and E.R.Weber, "Transition metals in silicon solar cells: from understanding to defect engineering", in the proceedings of the DOE Solar Energy Technologies Program Review Meeting (November 7 – 10, 2005, Denver, CO).

The impact of metal impurity clusters on solar cell performance in multicrystalline silicon**,** T.Buonassisi, A. A. Istratov, and E. R. Weber. *Proc. 2004 National Center for Photovoltaics Review Meeting*, Denver, USA (October 25-28, 2004), page 49 (NREL, Golden, CO, 2004).

T.Buonassisi, A.A.Istratov, and E.R.Weber, "The impact of metal impurity clusters on solar cell performance in multicrystalline silicon", proceedings of the Solar Energy Technologies Program Review Meeting (October 25-28, 2003), page 49 (published by NREL, Golden, Colorado, NREL/CR-520-36821)

A.A.Istratov, T.Buonassisi, M.A.Marcus, T.F.Ciszek, and E.R.Weber, "Dependence of precipitation behavior of Cu and Ni in CZ and multicrystalline silicon on cooling conditions", in: "14th workshop on Crystalline Silicon Solar Cells & Modules: Materials and Processes", Editor: B.L.Sopori, NREL, Golden, CO, 2004, p.165-169.

T.Buonassisi, A.A.Istratov, T.F.Ciszek, D.W.Cunningham, A.Gabor, R.Jonczyk, R.Schindler, A.Upadhyaya. B.Lai, Z.Cai, M.A.Marcus, and E.R.Weber, "Differences and similarities between metal clusters in mc-Si materials from different manufacturers", in: "14th workshop on Crystalline Silicon Solar Cells & Modules: Materials and Processes", Editor: B.L.Sopori, NREL, Golden, CO, 2004, p.226-229.

T.Buonassisi, A.A.Istratov, M.A.Marcus, and E.R.Weber , "Aluminum gettering and dissolution of Cu_3Si precipitates in silicon", in: "14th workshop on Crystalline Silicon Solar Cells & Modules: Materials and Processes", Editor: B.L.Sopori, NREL, Golden, CO, 2004, pp.222-225.

T.Buonassisi, M.A.Marcus, A.A.Istratov, M.Heuer, T.F.Ciszek, B.Lai, Z.Cai, and E.R.Weber, "Distribution and chemical state of Cu-rich clusters in silicon", in: "14th workshop on Crystalline Silicon Solar Cells & Modules: Materials and Processes", Editor: B.L.Sopori, NREL, Golden, CO, 2004, pp 161-164.

A.A.Istratov, T.Buonassisi, W.Huber, and E.R.Weber, "Evidence for segregation of iron at grain boundaries in polycrystalline and multicrystalline silicon" , in: "14th workshop on Crystalline Silicon Solar Cells & Modules: Materials and Processes", Editor: B.L.Sopori, NREL, Golden, CO, 2004, pp. 230-233.

T.Buonassisi, A.A.Istratov, and E.R.Weber, "Transition metals in multicrystalline solar cells: understanding the nature, origins, and impacts of metal contamination in mc-Si and minimizing its impact on solar cell performance", in: "14th workshop on Crystalline Silicon Solar Cells & Modules: Materials and Processes", Editor: B.L.Sopori, NREL, Golden, CO, 2004, pages 17-26.

T.Buonassisi, M.Heuer, A.A.Istratov, M.A.Marcus, R.Jonczyk, B.Lai, Z.Cai, J.Isenberg, W.Warta, R.Schindler, and E.R.Weber, "Impact of iron contamination in multicrystalline silicon solar cells: origins, chemical states, and device impacts", proceedings of the 19th photovoltaic solar energy conference (Paris, France, June 2004)

T.Buonassisi, M.Heuer, A.A.Istratov, E.R.Weber, Z.Cai, B.Lai, M.Marcus, J.Lu, G.Rozgonyi, R.Schindler, R.Jonczyk, and J.Rand, "Statistically meaningful data on the chemical state of iron precipitates in processed multicrystalline silicon using synchrotron-based x-ray absorption spectroscopy", P. 96-99 in: "13th workshop on crystalline silicon solar cell materials and processes", editor: B.L.Sopori, NREL, Golden, CO, 2003.

O.F.Vyvenko, T.Buonassisi, A.A.Istratov, and E.R.Weber, "Experimental procedure for determination of the depth of metal clusters in XBIC/μ-XRF mapping of metal clusters in silicon solar cells", P.102-105 in: "13th workshop on crystalline silicon solar cell materials and processes", editor: B.L.Sopori, NREL, Golden, CO, 2003.

A.A.Istratov, T.Buonassisi, R.J.McDonald, A.R.Smith, R.Schindler, J.A.Rand, J.Kalejs, and E.R.Weber, "Neutron activation analysis study of metal content of multicrystalline slicon for cost-efficient solar cells", P. 158-161 in: "13th workshop on crystalline silicon solar cell materials and processes", editor: B.L.Sopori, NREL, Golden, CO, 2003.

T.Buonassisi, O.F.Vyvenko, A.A.Istratov, E.R.Weber, G.Hahn, D.Sontag, J.P.Rakotoniaina, O.Breitenstein, J.Isenberg, and R.Schindler, "Assessing the role of transition metals in shunting mechanisms using synchrotron-based techniques", 3rd World Photovoltaic Specialists Conference (WCPEC-3), Osaka, Japan (2003), in: Proceedings of 3rd World Conference on Photovoltaic Energy Conversion (IEEE Cat. No.03CH37497). (Arisumi Printing Inc., Japan, 2003), Vol.2, pp.1120-3 (editors: Kurokawa K; Kazmerski LL; McNelis B; Yamaguchi M; Wronski C; Sinke WC)

A.A.Istratov, T.Buonassisi, E.R.Weber, R.J.McDonald, A.R.Smith, R.Schindler, J.Isenberg, J.Kalejs, J.Rand, P.Geiger, G.Hahn, J.P.Rakotoniaina, and O.Breitenstein, "Impact of metal impurities on solar cell performance", proceedings of the NCPV and Solar Program Review Meeting (March 24-26, 2003), pp. 228-230, published by NREL, Golden, Colorado, 2003. Available in electronic form, NREL/CD-520-33586.

O.F.Vyvenko, T.Buonassisi, A.A.Istratov, and E.R.Weber, "Application of synchrotron radiation based X-ray microprobe technique for the analysis of recombination activity of metals precipitated at Si/SiGe misfit dislocations. P. 111-116 in "12th workshop on crystalline silicon solar cell materials and processes", editor: B.L.Sopori, NREL, Golden, CO, 2002.

D.Macdonald, W.Brendle, A.Cuevas, and A.A.Istratov, "Injection-level dependent lifetime studies of copper precipitates in silicon, P. 202-205 in "12th workshop on crystalline silicon solar cell materials and processes", editor: B.L.Sopori, NREL, Golden, CO, 2002.

T.Buonassisi, O.F.Vyvenko, A.A.Istratov, E.R.Weber, R.Schindler, and G.Hahn, "Analysis of shunts in multicrystalline silicon solar cells using microprobe X-ray fluorescence technique, p. 266-270 in "12th workshop on crystalline silicon solar cell materials and processes", editor: B.L.Sopori, NREL, Golden, CO, 2002.

O.F.Vyvenko, T.Buonassisi, A.A.Istratov, and E.R.Weber, "Application of X-ray fluorescence technique to studies of aluminum gettering iu silicon", P. 271-274 in "12th workshop on crystalline silicon solar cell materials and processes", editor: B.L.Sopori, NREL, Golden, CO, 2002.

E. Major Results

E.1. Identification of the dominant metal impurities in bad regions; Comparison of different growth techniques on terms of metal contamination *(tasks 1.1 and 1.3)*

Neutron activation analysis (NAA) was used to determine the total metal content in three types of commercially available multicrystalline silicon – Astropower sheet material, Baysix cast material, and EFG ribbon. Besides determination of the average metal concentration in each of these three types of material, we compared the metal contents of samples cleaved from the areas with relatively high ("good regions") and relatively low ("bad regions") minority carrier diffusion length for each of the three materials.

The NAA results are presented in the Tables E.1.I-E.1.IV below. The dominant metal impurities were found to be Fe (6×10^{14} cm^{-3} to 1.5×10^{16} cm^{-3}, depending on the material), Ni (up to 1.8×10^{15} cm^{-3}), Co (1.7×10^{12} cm^{-3} to 9.7×10^{13} cm^{-3}), Mo (6.4×10^{12} cm^{-3} to 4.6×10^{13} cm^{-3}), and Cr (1.7×10^{12} cm^{-3} to 1.8×10^{15} cm^{-3}) (see Table E.1.I). The primary contaminants in all three materials were Fe, Ni, and Cr, which may be an indication of contamination with stainless steel. Copper was also detected (less than 2.4×10^{14} cm^{-3}), but its concentration could not be accurately determined because of a very short decay time of the corresponding radioactive isotope.

Remarkably, the total concentration of transition metals observed in all three mc-Si materials was much higher than necessary to explain the minority carrier lifetime degradation in these materials: the average concentration of iron alone was at least ten times higher than it would be sufficient, if all iron were in the interstitial state, to account for the carrier recombination responsible for the measured minority carrier diffusion length. Therefore, either transition metals are present in relatively recombination inactive chemical/structural state, or they are extremely inhomogeneously distributed in the wafer, or both.

Analysis of samples cleaved from the areas with high and low minority carrier diffusion length (Tables E.1.II-E.1.IV) revealed that the difference in metal concentration in "good" and "bad" areas is small. Only gold was consistently found in the "bad" areas in 1.5 to 5 times higher concentrations than in the "good" areas of all three materials. The rest of the metals detected by NAA showed either no trend at all, or, in some cases, metals were even found in slightly higher concentration in the "good" areas. Therefore, it is likely that it is not the total metal content but rather a variation in the spatial distribution and/or chemical/structural state of metals that leads to a change in their recombination properties.

Table E.1.I. Average metal concentration found by neutron activation analysis of three types of multicrystalline silicon material: Astropower (sheet technology), BaySix (cast), and EFG (ribbon growth). DL stands for “detection limit”.

Element	ASTROPOWER (cm^{-3})	BaySix (cm^{-3})	EFG (cm^{-3})
Fe	1.50×10^{16}	4.00×10^{14}	6.00×10^{14}
Ni	1.80×10^{15}	*less than DL (3e14)*	*less than DL (1.1e14)*
Co	9.70×10^{13}	2.10×10^{13}	1.70×10^{12}
Cu	*less than DL (7.8×10^{12})*	$<2.4\times10^{14}$	$<1.3\times10^{14}$
Cr	1.80×10^{15}	1.00×10^{13}	1.70×10^{12}
Hf	*less than DL (1.8×10^{12})*	7.80×10^{12}	*less than DL (6.8×10^{11})*
Mo	4.60×10^{13}	1.50×10^{13}	6.40×10^{12}
W	2.00×10^{13}	*less than DL (2.2×10^{11})*	*less than DL (8×10^{10})*
Au	4.80×10^{11}	6.50×10^{10}	2.00×10^{10}
As	4.70×10^{13}	3.40×10^{12}	*less than DL (9.3×10^{10})*
Sb	2.40×10^{14}	1.70×10^{12}	1.20×10^{11}
Ga	2.50×10^{13}	*less than DL*	9.00×10^{12}

Table E.1.II. Metal concentration in the areas of EFG samples with higher than average (“good regions”) and lower than average (“bad regions”) minority carrier diffusion lengths. Due to different irradiation and counting conditions, the detection limits of this measurement run were lower than of the runs presented in Tables I, III, IV. Therefore, iron and some other metals were below the detection limits.

Element	"Good" areas (cm^{-3})	"Bad" areas (cm^{-3})
Cr	2.97×10^{12}	5.94×10^{11}
Mo	7.09×10^{13}	6.00×10^{13}
Sb	8.20×10^{10}	9.00×10^{10}
Au	5.00×10^{11}	3.00×10^{12}

Table E.1.III. Metal concentration in BaySix wafers with relatively high (middle of the ingot) and relatively low (bottom of the ingot) minority carrier diffusion length. DL stands for “detection limit”.

Element	Sample A (middle of the ingot, better cell performance) (cm^{-3})	Sample B (bottom of the ingot, lower cell performance) (cm^{-3})
Ag	3×10^{12}	*less than DL (5×10^{11})*
Cr	1.9×10^{13}	*less than DL (3×10^{12})*
Fe	4.7×10^{14}	*less than DL (4.5×10^{14})*
Ni	*less than DL (3×10^{14})*	*less than DL (2.3×10^{14})*
Co	8×10^{12}	2.80×10^{13}
As	3.80×10^{12}	2.90×10^{12}
Sb	3.70×10^{11}	3.20×10^{12}
W	*less than DL (1×10^{11})*	*less than DL (3.6×10^{11})*
Au	1.50×10^{10}	1.20×10^{11}
Zr	3.3×10^{14}	3.5×10^{14}
Hf	1.40×10^{13}	*less than DL (1.1×10^{12})*
Cu	<1.6e14	$<3.2\times10^{14}$
Se	2×10^{13}	4×10^{12}
Mo	1.50×10^{13}	*less than DL (5.4×10^{13})*

Table E.1.IV. Metal concentration in Astropower wafers with relatively high (“wafer A”) and relatively low (“wafer B”) minority carrier diffusion length areas.

Element	Wafer A (better cell performace) (cm^{-3})	Wafer B (lower cell performance) (cm^{-3})
Cr	3×10^{15}	5×10^{13}
Fe	1.6×10^{16}	8.7×10^{15}
Ni	2.8×10^{15}	*less than DL (5e15)*
Co	1.3×10^{14}	6.1×10^{13}
Cu	*less than DL (5e12)*	*less than DL (1e13)*
Ga	2×10^{12}	*less than DL(3e12)*
As	9×10^{13}	3.5×10^{12}
Zr	*less than DL (1.5×10^{15})*	*less than DL (4×10^{15})*
Hf	*less than DL (1.1×10^{12})*	*less than DL (3×10^{12})*
Mo	6×10^{13}	3×10^{13}
Sb	2×10^{13}	5×10^{14}
W	2×10^{13}	2×10^{13}
Au	3.5×10^{11}	4×10^{11}

E.2. Removal of metals from mc-Si by aluminum gettering; metals in bad regions which cannot be removed by aluminum gettering *(task 1.2)*.

700 μm-thick CZ sample containing 10^6 cm^{-3} oxygen precipitates was intentionally contaminated with copper at 1200°C. A 5 μm aluminum layer was evaporated onto one surface of the sample through a wire mesh. Gettering anneal was performed at 800°C for 2 hours in forming gas ambient.

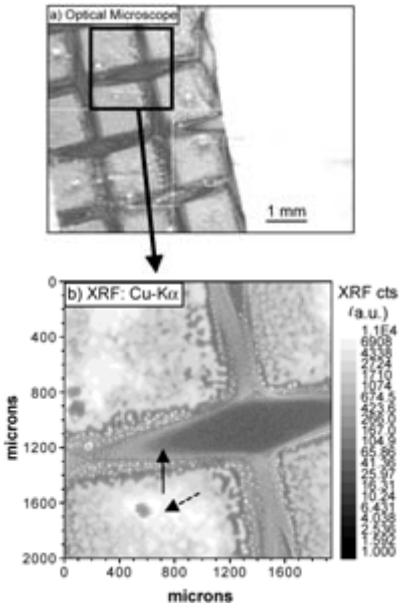

Figure E.2.1: (a) Optical microscope image of the surface of a Cu-contaminated CZ-Si sample with 106 cm-3 oxygen precipitates. This sample was annealed at 800°C for 2 hours after squares of aluminum were evaporated onto the surface through a wire mesh. (b) Cu-Ka x-ray fluorescence microscopy image for the region highlighted in (a) shows the high concentration of Cu gettered to the thick Al squares (note log XRF scale), and the fine dusting of Cu in tiny Al particles between the squares, indicative that even a tiny bit of Al is a very effective getter of Cu. The dashed arrow denotes location of μ-EXAFS scans in Figure E.2.2/

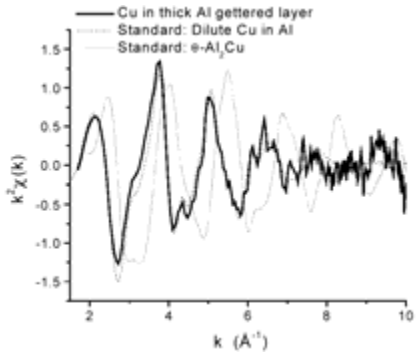

Figure E.2.2: EXAFS of Cu gettered to thick regions of Al (dashed arrow in Figure E.2.1b). Notice the good agreement with the standard material of dilute Cu dissolved in Al

μ-XRF mapping of the aluminum layer (Figure E.2.1) revealed that copper was present only where aluminum was deposited through the wire mesh. Chemical identification performed by μ-XAS revealed that copper gettered to the thicker regions of Al (indicated by a dashed arrow in Figure E.2.1b) had formed a dilute Cu solution in Al (Figure E.2.2) identified in [1]. This confirms that the mechanism of segregation in aluminum is a higher metal solubility in the liquid phase.

The segregation coefficient of Cu in aluminum, $k = C_{Al} / C_{bulk}$, was derived from the µ-XRF map in Figure E.2.1b as *at least* (1-2)×10^3.

Despite the high segregation coefficient in Al, not all metal clusters can be removed by gettering of solar cell materials. Figure E.2.3 shows an example of results obtained on as-grown Astropower sheet material which was subject to a backside aluminum gettering sequence for 4 hrs at 800°C. A coarse XBIC scan over the front surface reveals two prominent features of low minority carrier diffusion length that have persisted despite the Al gettering treatment: (a) strongly recombination-active grain boundaries, appearing as dark lines, and (b) localized intragranular defects, appearing as dark dots within the grains.

µ-XRF point spectra revealed that Fe was present en masse at both these locations, with a small contribution from Cr in the case of certain intragranular defects. It was found from high-resolution µ-XRF maps that the intragranular defects are irregular in shape and consist of an agglomeration of many nanoparticles, as shown in Figs. E.2.4a and E.2.4b. The grain boundaries were also decorated by Fe-rich nanoparticles, as shown in Figure E.2.4c. The chemical states of these particles were measured by µ-XAS; by comparison with standard material, it was deduced that Fe was in the form of iron silicide, as shown in Figure E.2.4d. The spacing and average size of the iron silicide precipitates along the grain boundaries of this material were significantly homogeneous. The particle density along the surface of the grain boundary was determined to be within the range of (1-2)×10^7 cm^{-2}. The average iron content of each of these precipitates at the grain boundaries was determined to be (0.69-2.1)×10^6 Fe atoms; if these precipitates assumed to be spherical, they would have radii of approximately 23±5 nm.

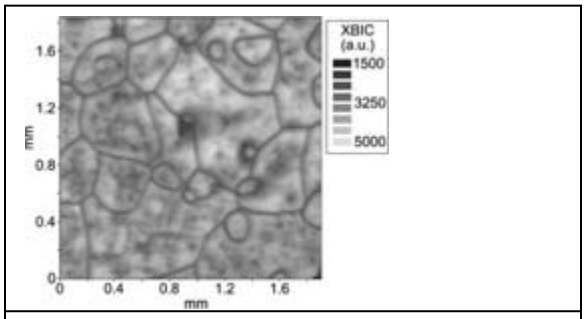

Figure E.2.3: XBIC map of a typical region of Al-gettered sheet material. Features of interest include recombination active grain boundaries and point-like intragranular defects. Dark regions in the map correspond to the areas with high recombination activity.

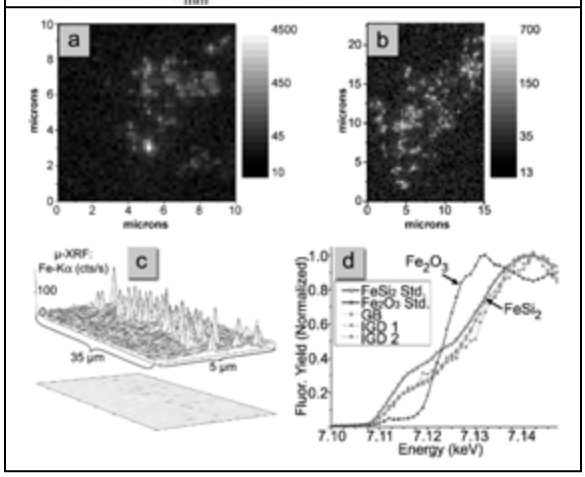

Figure E.2.4: (a, b) µ-XRF maps of the Fe distribution within typical intragranular defects in sheet material, noted by points of lower XBIC signal in Figure E.2.3. These defects consist of irregularly-shaped, micron-sized clusters of Fe nanoparticles, and make the largest contribution to the total metal content in this sample. (c) µ-XRF map of Fe nanoparticles within a typical grain boundary, shown in 3D (above) and in 2D projection (below). Although each Fe nanoparticle at the grain boundary is only ~23±5 nm in radius, these nanoparticles are also believed to contain a sizeable fraction of the total Fe in this sample, due to their high spatial density. (d) The chemical state of the Fe particles shown in (a-c) is revealed by µ-XAS to be most similar to $FeSi_2$.

There are four possible explanations to the question why some metal clusters cannot be removed by gettering.

The first one is a high binding energy of metals in clusters of metal-oxides or metal-silicates [2]. Our data presented in Section E.4 of this report confirmed that such precipitates were observed in some types of mc-Si. However, the numerical majority of precipitates found in our experiments in mc-Si wafers both before and after gettering were metal-silicides.

The second mechanism, suggested by Plekhanov and Tan [3], is kinetically limited precipitate dissolution, which is observed when metal solubility at the gettering temperature is much lower than the total metal concentration in the sample. This mechanism implies that the precipitates can be gettered, but it may take many hours.

The third mechanism is stabilization of metal clusters either by lattice strains of structural defects [4, 5] or due to limited diffusivity of silicon self-interstitials which are needed to counterbalance the volumetric shrinkage associated with the dissolving Cu_3Si precipitates [6, 7].

Finally, the fourth possible mechanism is the limited capacity of the gettering layer. With the estimated segregation coefficient $k = 2\times10^3$ and typical solar cell parameters for wafer thickness $d = 240$ μm and Al layer thickness $w = 1$ μm, one can use the following equation:

$$\frac{\text{[Cu] in Bulk After Gettering}}{\text{[Cu] in Bulk Before Gettering}} \equiv \frac{c_{\text{bulk}}}{c_{\text{o}}} = \frac{c_{\text{bulk}}}{\left(\frac{c_{\text{bulk}} \cdot d + c_{\text{Al}} \cdot w}{d}\right)} = \frac{1}{1+\frac{k \cdot w}{d}}$$

to predict that an upper limit of about 90% of the total metal content can be gettered from the bulk by segregation to the Al layer with $k=10^3$.

While all four mechanisms can play a role in limiting the efficiency of gettering of mc-Si, our experimental data suggest that main contributions are due to the fourth, second, and third mechanisms.

E.3. Role of metal impurities in the formation of shunts (*task 1.4*).

Shunts were analyzed in two types of solar cells, cast and RGS. The samples were pre-characterized with lock-in thermography and LBIC. The areas of interest for μ-XRF analyses were found by in-situ XBIC by correlating LBIC and XBIC maps. Upon a μ-XRF analysis at the shunt location (shown as a small black box in Figs. E.3.1a,b,c), high concentrations of silver (Figure E.3.1d) and titanium (Figure E.3.1e) were detected. These metals are used to form the contact fingers of the metallization grid. Despite being found at the shunt location a millimeter away from the nearest contact finger, these metals were present in nearly the same proportions as in the contact strips themselves, which are visible in the lower part of Figures E.3.1d and E.3.1e.

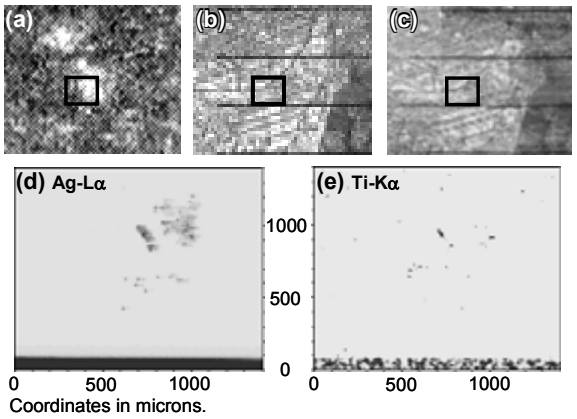

Figure E.3.1: The procedure followed to determine the presence of metals at a shunting location in a fully-processed cast multicrystalline solar cell: A lock-in thermography map (a) of a 7×9 mm^2 region of the solar cell containing two shunts is correlated with LBIC (b). At the synchrotron, an XBIC map (c) is made over the same region. X-ray fluorescence microscopy (d & e) is performed on the small sub-region containing one shunt (denoted by the box in a, b, and c). Silver (d) and titanium (e) appear in quantities comparable to their concentrations in the contact strips (visible at the bottom of the μ-XRF maps). Residues of the contact metallization are likely the cause of this shunt.

These facts indicate that this shunt is most likely a process-induced defect that was formed during metallization grid deposition, which may form if silver or palladium is deposited directly on the surface of the wafer without a properly-placed titanium buffer layer, or in an event of overfiring. Such a process-induced defect, while not material-specific, can be especially deleterious for solar cells with shallow emitters.

The second group of experiments was performed on RGS material containing current collecting channels. These channels are unique to RGS material and are known, when present in high concentration, to have detrimental effect (lower fill-factor and open-circuit voltage) similar to shunting. The current collecting channels, observed in LBIC with large light penetration depth and as heat-generating spots in thermography maps (see Figure E.3.2), were found in XBIC maps and analyzed with μ-XRF. As shown in Figure E.3.3, copper and iron were found to be present at the current collecting channel (bounded between the dashed lines). Lower bounds for the peak metal concentrations (measured in the units of metal atoms per cm^2 of the sample surface) were determined to be 1.7×10^{14} cm^{-2} for Fe and 1.5×10^{14} cm^{-2} for Cu, by assuming the metals lie very near to the wafer surface. The width of the iron peak is close to the diameter of the incident x-ray beam, which indicates that iron formed precipitates localized within a diameter equal to or smaller than the beam size. The copper peak is much broader than the iron peak, indicating that copper more likely forms a colony of small precipitates that appear to decorate an extended defect.

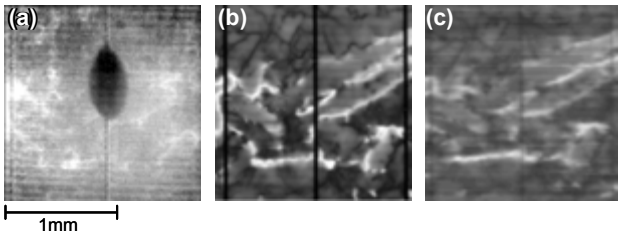

Figure E.3.2: Detail of a shunt area in an RGS sample. The features evident in the 54 Hz lock-in thermography image taken at 0.52V forward bias (a) resemble those of the 980 nm LBIC (b) and XBIC (c) maps of this area taken at zero bias, indicating that the shunting current is generated at or near the current collecting channels. The oval marker evident in (a) was placed on the surface of the solar cell to mark the region of interest.

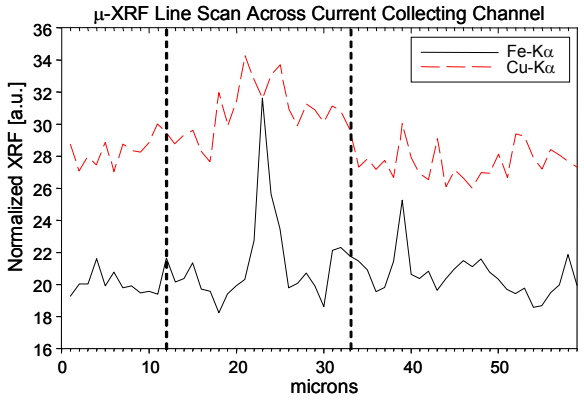

Figure E.3.3: An x-ray fluorescence microscopy line scan reveals an increase of copper and iron concentrations at a current collecting channel (between vertical dashed lines, identified by XBIC). A lower bound for the peak Fe concentration is 1.7x1014 cm^{-2}, and Cu $1.5x10^{14}$ cm^{-2}. This result suggests that current collecting channels are effective gettering sites for transition metals, which may play a role in shunt formation.

E.4. Chemical nature of metal precipitates formed after heat treatments and interaction of metals with lattice defects and oxygen (*tasks 2.1 and 2.3*).

Chemical state of iron and copper clusters was studied in a variety of materials to determine whether these metals form gettering-resistant chemical compounds, such as oxides and silicates.

Copper-rich clusters were studied in four types of silicon materials with varying amounts of oxygen: ("sample 1") Float zone silicon intentionally contaminated with (3-4)×10^{16} Cu/cm^{-3} during crystal growth; ("sample 2") Misfit dislocation heterostructure, consisting of a 2 μm thick n-type $Si_{0.98}Ge_{0.02}$ middle layer between a 2.5 μm n-type silicon bottom buffer layer on a (001) silicon substrate and a 2.5 μm thick n-type silicon cap layer, intentionally contaminated with Cu at 800°C; ("sample 3") Czochralski silicon containing approximately 1.8×10^{6} cm^{-3} oxygen precipitates and approximately 1.5×10^{15} cm^{-3} boron intentionally contaminated with Cu at 1200°C; ("sample 4") As-grown, cast mc-Si wafer extracted from near the bottom of the cast mc-Si ingot, where the interstitial oxygen concentration can be as high as 10^{18} cm^{-3}. Prior to μ-XAS analyses, each Si sample was mapped with μ-XRF to reveal the precise distribution of Cu-rich clusters.

Cu K-edge μ-XANES scans of the copper-rich clusters in all four samples yielded strikingly similar spectra to Cu_3Si standard material (Figure E.4.1). No indications of Cu clusters in chemical state other than copper-silicide was found in these samples.

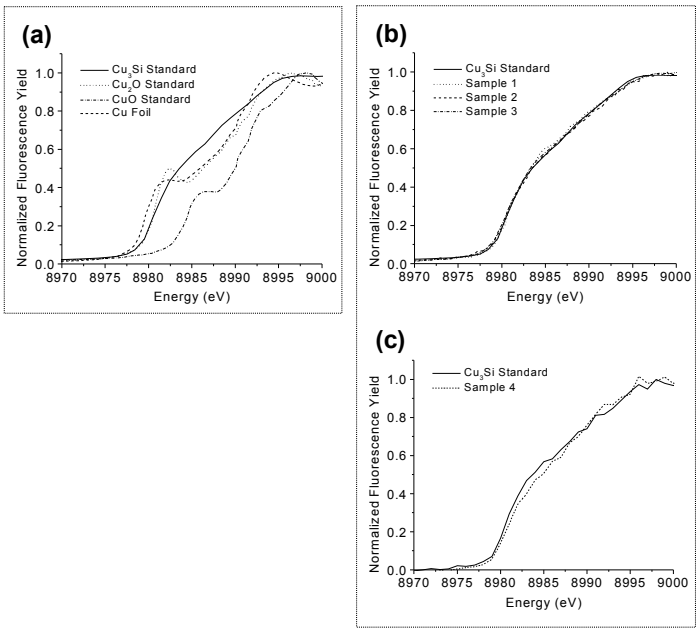

Figure E.4.1: μ-XANES showing the spectra of standard materials (a), and then the excellent match of Cu-rich clusters in a variety of silicon materials with the Cu_3Si standard (b,c, taken at different beamlines).

Iron-rich clusters were characterized in as-grown and processed cast mc-Si. XBIC maps revealed certain grain boundaries with exceptionally high recombination activity. Multiple iron-rich clusters were detected by μ-XRF at these locations, as the maps in Figure E.4.2 and Figure E.4.3 demonstrate. These iron-rich clusters populating grain boundaries can be divided into two distinct types, with distinct physical properties. Firstly, while the vast majority of iron-rich

clusters are small (e.g. P1, P3, and P4 in Figure E.4.2b, and all particles in Figure E.4.3b), some rare clusters have nearly two orders of magnitude higher µ-XRF Fe counts (e.g. P2 in Figure E.4.2b; note the log scale of Fe concentration). An analysis by µ-XAS reveals that the clusters with smaller Fe counts are composed of iron-silicide ($FeSi_2$), while the clusters with much larger Fe counts are composed of oxidized iron (Fe_2O_3), as shown in Figure E.4.4a and E.4.4b, respectively.

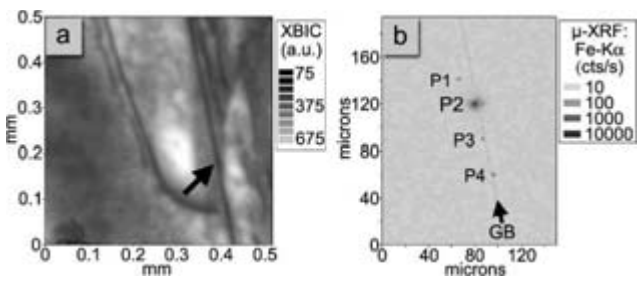

Figure E.4.2: (a) Typical XBIC image of a cast mc-Si sample. The arrow in (a) points to a recombination-active grain boundary, a region of which was analyzed by µ-XRF in (b). Fe-rich clusters are found along the grain boundary, highlighted by the arrow and the dotted line in (b). Note the log scale of µ-XRF Fe-Kα signal intensity, indicating that P2 has approximately two orders of magnitude higher counts than the others.

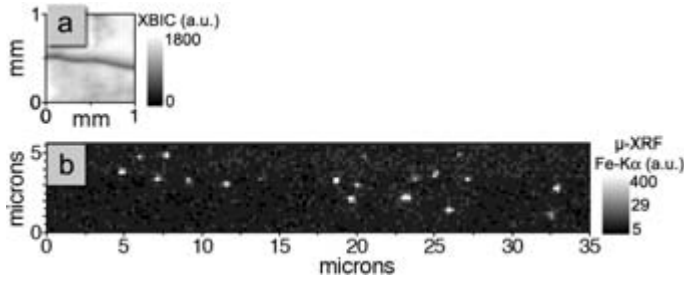

Figure E.4.3: (a) Large area XBIC and (b) high-resolution µ-XRF map of the iron distribution at a grain boundary in as-grown cast mc-Si. Several $FeSi_2$ nanoprecipitates are observed. Although some clustering is evident on a micron-scale, on a larger scale these $FeSi_2$ nanoprecipitates are distributed rather homogeneously.

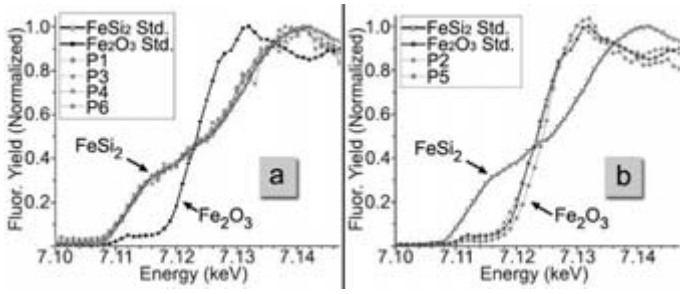

Figure E.4.4: µ-XAS data discern two types of Fe-rich cluster in cast mc-Si material: (a) smaller iron silicide ($FeSi_2$) and (b) larger iron oxide (Fe_2O_3). Data labels correspond to precipitates viewed in the µ-XRF image Figure C.4.2.

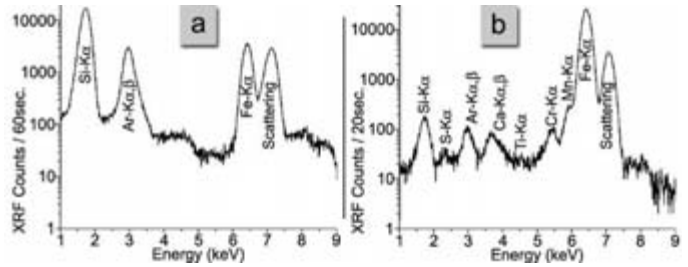

Figure E.4.5: Typical µ-XRF point scans for the two types of Fe-rich clusters in cast mc-Si: (a) Smaller $FeSi_2$ clusters, without detectable quantities of other metals, and (b) larger Fe_2O_3 particles, wherein iron is accompanied by other elements reminiscent of ceramics, dirt, and stainless steel.

The compositions of these clusters also differ, as determined by the µ-XRF point scans. While the Fe_2O_3 clusters typically show appreciable amounts of other contaminants such as Cr,

Mn, and Ca (Figure E.4.5b), the smaller $FeSi_2$ clusters generally show none of these above the μ-XRF detection limit (Fig E.4.5a). Only in as-grown material can Ni and Cu be found precipitated in the immediate vicinity of $FeSi_2$ in detectable quantities, but not Cr, Mn, Ti, or Ca.

Additionally, the morphologies and orientations of these two types of cluster are very distinct. The large Fe_2O_3 clusters do not appear to be preferentially oriented along the grain boundary or the crystal growth direction. In contrast, the $FeSi_2$ particles are elongated along the grain boundary only in the direction of crystal growth, by a factor of at least 3-4.

The distributions of these clusters also differ. While the large Fe_2O_3 clusters are inhomogeneously distributed, the smaller $FeSi_2$ clusters appear to be more regularly spaced. Taking into account the attenuation length of the Fe-Kα fluorescence in Si, one calculates a $FeSi_2$ precipitate density of $(1.5\text{-}2)\times10^6$ per cm^2 of grain boundary surface area in Figure E.4.3, resulting in an average spacing between precipitates of 7-8 μm along the grain boundary.

In the past, it has been suggested that oxidized metallic precipitates may form within silicon because many species of metal atom, e.g. Cu and Fe, have higher binding energies to oxidized compounds such as silicates and oxides than to silicides (see, e.g., [6, 8]). While it is true that metals bond strongly to oxygen, the same can also be said for silicon, and thus an analysis of whether a metallic oxide, silicate, or silicide will form should take this competitive oxidation potential into consideration. It is known that oxygen can form a very stable and electrically inactive interstitial complex with silicon (O_i), not to mention SiO_2. Table E.4.I reproduces the *enthalpy of formation per oxygen atom* (the figure of merit in a balanced equation) from individual elements for a selection of oxidized species, demonstrating that when [Si] >> [O] > [Cu], equilibrium thermodynamics predicts that silicon will be the predominant oxidized species.

While the precise values of enthalpies of formation cited in Table E.4.I do not reflect the additional detailed calculations necessary to account for the formation of a species within a silicon lattice, Table E.4.I indicates that in the presence of silicon, a strong competitor for oxygen, Cu and Fe will likely be reduced or remain unoxidized. Based on these observations and our μ-XAS measurements, it is concluded that both Cu and Fe in the presence of Si with [O] << [Si] will not tend to form stable chemical bonds with oxygen, and thus will likely either form non-oxidized precipitates, out-diffuse, or remain dissolved if solubility permits.

Table E.4.I. The enthalpies of formation per mol per oxygen atom at 298.15K for various oxidized metal species. It is shown that the binding energy of oxygen to silicon is far greater than that of oxygen to iron or to copper. The same is not true for all metals, e.g. hafnium. Data are from *CRC Handbook of Chemistry and Physics, 84th Edition* (CRC Press, 2003).

Compound	$\Delta_f H°$ (kJ/mol)
1/2 HfO_2	-572.4
1/2 ZrO_2	-550.3
1/2 TiO_2	-472.0
1/2 SiO_2	**-455.4**
1/4 Fe_2SiO_4	-370.0
1/4 Fe_3O_4	-279.6
1/3 Fe_2O_3	-274.7
Cu_2O	-168.6
CuO	-157.3

E.5. Recombination activity and thermal stability of complexes which metals form in mc-Si (*task 2.2*).

In the course of our research, we had numerous confirmations of high recombination activity of metal clusters in mc-Si. For example, Figure E.5.1 gives an example how μ-XRF maps, characteristic of metal distribution in solar cells, correlate with XBIC maps, characteristic of minority carrier diffusion length.

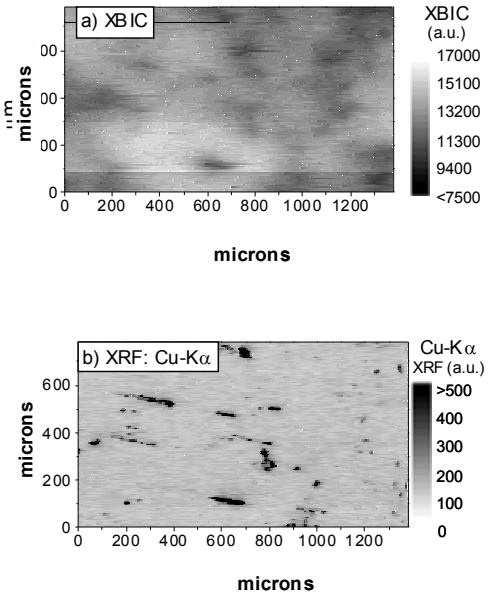

Figure E.5.1: (a) x-ray beam induced current and (b) Cu-Kα x-ray fluorescence microscopy maps of float zone silicon contaminated with (3-4)×10^{16} Cu cm^{-3} during crystal growth. Notice the strong correlation between the presence of copper-rich clusters (b) and the decrease of current collection efficiency (a).

The impact of transition metals on cell efficiency is determined by their spatial distribution. This can be understood by considering a hypothetical silicon sample with 10^{14} cm^{-3} iron-boron pairs (Fe_i-B_s) or interstitial iron (Fe_i). The minority carrier diffusion length in such a sample would be approximately 20 μm or 10 μm, respectively [9]. Now, let us assume these iron atoms are allowed to diffuse towards one another and form precipitates of iron-silicide. If we approximate the new minority carrier diffusion length as the distance between neighboring iron silicide clusters, then, if the same amount of iron forms precipitates with diameters of 60 nm, the diffusion length would be ~30 μm; if precipitates with diameters 350 nm form, the average diffusion length would be ~180 μm, etc. One can see the pattern: with increasing average precipitate size (and decreasing density of precipitates), the minority carrier diffusion length increases. It can thus be concluded that it is the distribution of metals, and not their total bulk concentration, that affects the mc-Si cell efficiency.

The iron-rich clusters analyzed in this study can be divided into two distinct groups, larger particles and smaller precipitates. Larger particles (diameter ≥ 1 μm) are present in rather low spatial densities and are believed to be inclusions originating from foreign sources, e.g. the feedstock, growth surfaces, and/or production equipment. These inclusions are (a) accompanied by lesser amounts of other metals such as Cr, Ni, Mn, Ti, S, or Ca, suggestive of stainless steels or ceramics, and/or (b) in an oxidized chemical state. Smaller (dia. < 800 nm, typically < 100 nm) iron silicide precipitates are observed in much higher spatial densities, separated by as little as a few microns. Despite their small size, a large amount of iron (up to $10^{14\text{-}15}$ cm^{-3}) is estimated to be contained in these iron silicide nanoprecipitates due to their high spatial density. Copper was found primarily in small copper-silicide precipitates; no oxidized copper particles was observed.

The smaller, more distributed iron silicide clusters are believed to have a large impact on solar cell device performance, the reason being the small distance separating adjacent clusters. This is substantiated by the correlation between the recombination active grain boundaries observed in numerous XBIC images presented in our quarterly reports, publications, and in this

report, and the presence of metal silicide precipitates separated by distances of only a few microns. A model developed by [10, 11] predicts that when the distance separating neighboring recombination-active clusters along a grain boundary is less than the minority carrier diffusion length within the grains, the grain boundary becomes noticeably recombination-active for minority carriers. This model agrees with our observations. Similarly, much lower diffusion lengths were observed in grains which contained higher density of metal clusters at intragranular defects.

Iron-oxide particles are expected to be very stable at typical gettering temperatures, and are extremely difficult to remove. However, due to their low spatial density, they have limited impact on device performance. Smaller metal-silicide particles, usually present in much higher density, have much more serious lifetime limiting effect. Additionally, interstitially and substitutionally dissolved metals, even if present in minute concentration, can greatly impact the solar cell performance. Metal-silicide precipitates are relatively easy to dissolve. However, due to the large total amount of metals found in these precipitates, the kinetics of gettering is limited by the solubility and diffusivity of metals. Since gettering involves dissolution of metal clusters, i.e., a conversion of precipitated metals into potentially even more recombination active interstitial/substitutional metal atoms, incomplete gettering may lead to no observable improvement or even degradation of minority carrier diffusion length.

Partial dissolution of metal-silicide precipitates during short high temperature heat treatments was demonstrated in the following experiment. One sample from a set of sister wafers from near the bottom of a cast mc-Si ingot was subject to a rapid thermal anneal (RTA) at Fraunhofer ISE for emitter diffusion at 1000°C for 20 seconds. The same grain boundary in the processed sample, as well as the as-grown material, was analyzed by µ-XRF. In the as-grown material (Figure E.5.2a), large iron clusters could be seen at grain boundaries accompanied by denuded zones (Figure E.5.2c). Also copper and nickel clusters were detected, although in a lower density (not shown). In the sample processed at 1000°C for 20 seconds, neither copper nor nickel could be detected, while the iron clusters contained only 50% their original iron content. The decrease of iron content at the precipitates corresponds with decreasing material performance. XBIC and LBIC maps indicate a large increase of intragranular recombination activity (Fig E.5.2d), as well as the lack of denuded zones around the grain boundaries. The iron, copper, and nickel dissolved from the precipitates are believed to have diffused into the grains at high temperatures, and re-precipitated at structural defects during cooling. The short high-temperature anneal combined with a rapid cooling rate probably exacerbated the delocalized iron precipitation within the grains, and deteriorated the material properties.

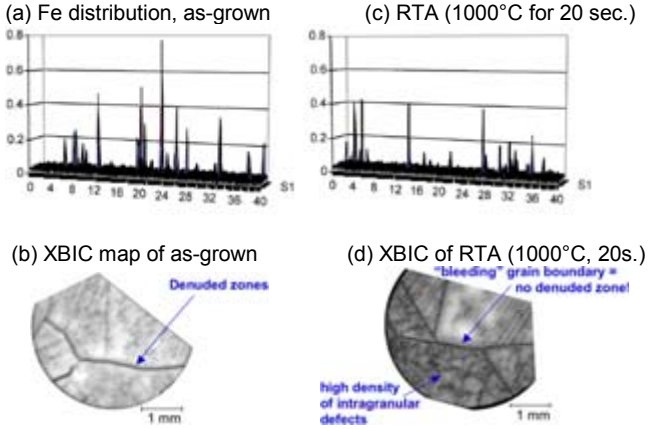

Figure E.5.2: 40 × 6 µm^2 µ-XRF maps of the iron distribution in grain boundaries of cast mc-Si sister wafers: (a) as-grown and (b) rapid thermal annealed at 1000°C for 20 sec. A comparison of higher resolution µ-XRF maps of numerous precipitates in both samples reveal a 50% reduction in Fe content as a result of high-temperature processing. This dissolved Fe is believed to be responsible for the degradation in minority carrier diffusion length observed in the XBIC images (c and d).

E.6. Pathways of formation of gettering-resistant clusters during mc-Si ingot growth (*tasks 3.1 and 3.2*).

Experimental evidence obtained in this study enabled us to conclude that the origins of metals in most mc-Si materials include some combination of the following: Metals dissolved in the silicon feedstock, foreign metallic particles introduced with the feedstock, metals originating from furnace or production equipment, and metals diffusing from the walls of the crucible or growth surfaces. Figure E.6.1 is a pictorial representation of the mechanisms of incorporation of metals into solar cells. Each of these mechanisms is discussed briefly below.

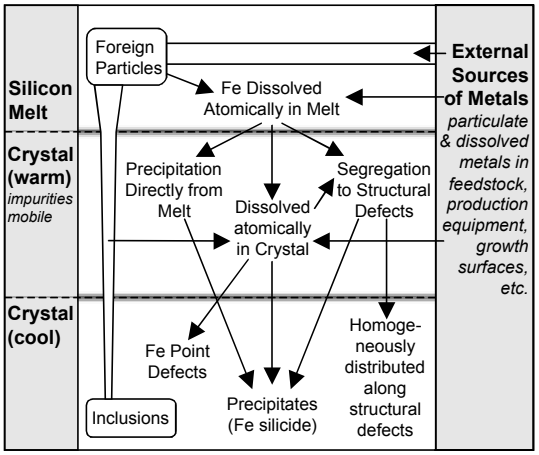

Figure E.6.1: Graphical representation of the origins of Fe contamination in mc-Si, the physical mechanisms responsible for incorporating large amounts of Fe into the mc-Si material when warm, i.e. temperatures at which impurity atoms are mobile, and the formation mechanisms of the Fe-rich clusters one observes in finished mc-Si material. Two types of Fe-rich cluster are observed in finished material: inclusions of foreign particles introduced into the melt, and iron silicide nanoprecipitates formed from dissolved iron. Note that the partial or complete dissolution of the former can contribute to the formation of the latter.

The hypothesis that foreign particles (originating from the feedstock, production equipment, etc.) are incorporated into the melt is substantiated by the μ-XRF observations of a few metal-rich particles of unusually large sizes (typically ≥ 1 μm). All of these large particles observed have one or both of the following additional characteristics: (a) the coincidence of iron with large amounts of other (often slowly-diffusing) metal species (e.g. Ca, Ti, Cr, Mn, Ni, etc.), the relative proportions of which allude to certain steels or ceramics and (b) an oxidized chemical state. This last point is a significant indicator of foreign particles being included in the melt, as oxidized iron and copper compounds are not thermodynamically favored to form under equilibrium conditions within silicon, as discussed in sec. E.4. However, an Fe_2O_3 particle inserted into the silicon melt should retain its structural integrity for a limited time, as the melting temperature of Fe_2O_3 is approximately 1565°C, about 150°C above the melting temperature of Si. Oxidized Cu particles will dissolve very quickly, as the low melting temperatures of both Cu_2O (1235°C) and CuO (1326°C) is lower than the melting point of silicon (1414°C). Experimental evidence up to this point has shown no evidence for oxidized Cu-rich clusters inside silicon crystals.

The possibility that metals found in cast mc-Si could diffuse from the crucible walls is supported by the fact that iron and other metals are typically present in the silicon nitride crucible lining typically in concentrations as high as parts per million (metal oxides are often added to densify and harden silicon nitride).

As shown in Figure E.6.1, besides (a) direct incorporation of incompletely dissolved foreign metal-rich particles into the crystal as inclusions, there are several other mechanisms of

incorporation of metals into the crystal: (b) direct precipitation of locally supersaturated iron from the melt (the mechanism suggested in [12, 13]), (c) segregation of metals dissolved in the melt to structural defects, (d) incorporation of dissolved Fe in the melt into single-crystalline regions of the material as interstitial atoms, and (e) diffusion of Fe from the growth surfaces into the crystal. The latter two mechanisms (d and e) are rather limited in their potential to introduce large amounts of Fe into most mc-Si materials, due to the segregation effect between the melt and the crystal, and to a limited diffusion length of metals within silicon. Mechanism (c) is discussed separately in Section E.7.

The density and size of metal precipitates can be expected to depend on cooling conditions. With slow cooling rates and high metal concentrations, a few "large" (10's of nm dia.) metal silicide precipitates are expected to form. On the other hand, faster cools offer less time for supersaturated metals to diffuse and form large clusters, thus favoring a more homogenous distribution of metals along structural defects, either atomically or as smaller precipitates. This dependence was observed experimentally in our studies: cast mc-Si which is cooled very slowly contained relatively larger particles with larger spacing in between, whereas sheet material, which is grown and cooled comparatively quickly, exhibited precipitates of closer spacing and smaller average size despite a total Fe content 1-2 orders of magnitude higher than cast mc-Si. The distribution of metal clusters between grain boundaries and intragranular defects is likely to depend both on the cooling regime and the availability and type of nucleations sites within grains.

Quantitative analysis of μ-XRF maps allowed us to estimate the total iron concentration in Astropower sheet material as $(0.1\text{-}3)\times10^{16}$ Fe/cm^3 at intragranular defects and $(0.4\text{-}2)\times10^{15}$ Fe/cm^3 at grain boundaries. In cast material, the majority of iron clusters were observed at grain boundaries; the estimated iron concentration in these clusters was $(0.5\text{-}3)\times10^{14}$ Fe/cm^3. Previous NAA analyses on these materials indicate total Fe contents of $(0.87\text{-}1.6)\times10^{16}$ Fe/cm^3 for sheet mc-Si and $(4.0\text{-}4.7)\times10^{14}$ Fe/cm^3 for cast mc-Si. Hence, the amount of Fe contained in these samples in iron silicide nanoprecipitates is comparable to the total amount of Fe in these samples, as measured by NAA. The iron silicide nanoprecipitates – especially those dispersed homogeneously along the grain boundaries – are extremely difficult to detect with most standard analytical techniques, due to their small spatial dimensions and comparatively large distances separating neighboring particles. Yet, it is precisely this form of Fe – homogeneously distributed in smaller clusters – that has a strong negative impact on the device performance.

E.7. Segregation of metals at structural defects (*additional topic 6.2; extends tasks 3.2 and 2.2*).

Simple equilibrium segregation models alone cannot account for the fact that $10^{14\text{-}16}$ cm^{-3} of Fe and other transition metals (Sec. E.1) are present in mc-Si materials. Were the amount of metals incorporated into the final crystal determined simply by their segregation into single-crystalline regions (described by the segregation coefficient (the ratio of Fe solubilities in single crystalline silicon and in the melt) which typically ranges from 10^{-5} to10^{-7} cm^{-3} [14]), this would imply that the melt at the solid-liquid interface contained as much as 0.001%-1% of transition metals! If in fact this high metal concentrations were present, instability in the solid-liquid interface would arise, and certainly columnar crystal growth with centimeter-sized grains would not proceed as desired in the case of cast mc-Si.

Incorporation of large oxidized particles could account for a fraction of the total metal content of mc-Si, but according to our estimates this fraction is small.

One of the mechanisms, which in our opinion could play an important role in incorporation of metals in mc-Si, is segregation of metals to structural defects. It is known that the solubility of metals in polysilicon is higher than in single-crystalline silicon [4], which is a consequence of the interaction of metals with dangling or reconstructed silicon bonds in structural defects (e.g. grain boundaries), as well as the reduction of strain energy from metals settling in a distorted silicon lattice near the structural defects. A higher metal solubility in mc-Si would lead to a lower effective segregation coefficient and incorporation of a higher metal concentration in the mc-Si ingots.

To determine how the solubility of iron in mc-Si differs from that in single-crystalline Si, we used a structure consisting of a thin polysilicon layer deposited on a CZ-grown silicon wafer. The advantage of polysilicon is that it has a high density of grain boundaries which is practically homogeneous on a macroscopic scale, and it can easily be deposited on a CZ substrate which can then be used as in-situ reference. The sample analyzed in Fig E.7.1 consisted of 11 μm of nominally undoped polysilicon deposited on top of a p^- silicon substrate. The sample was contaminated from the backside by scratching with an iron wire, annealed in a vertical furnace at 1150°C in N_2 + 5% H_2 ambient for 90 min, and quenched in silicone oil.

A decrease in the iron concentration in the substrate towards the interface with polysilicon stems from relaxation gettering of iron during the silicone oil quench, whereby supersaturated iron diffuses from the substrate to the polysilicon layer. The total amount of iron that was gettered in the poly-Si layer due to a combination of segregation and relaxation mechanisms can be determined, in the units of Fe atoms per cm^2 of the sample surface, by integrating the area "A" of the plot in Figure E.7.1a between the SIMS data in polySi and the equilibrium iron solubility. The total amount of iron that diffused into the polysilicon layer during cooling driven by relaxation can be calculated by integrating the area "B" in the substrate. By performing the integration, one obtains $A=1.44\times10^{13}$ cm^{-2} and $B=2.52\times10^{12}$ cm^{-2}. Since the area A is 6.4 times greater than the area B, relaxation gettering alone cannot account for all iron accumulated in concentration above its equilibrium solubility in the area B. The segregation coefficient k can be determined as follows: $k= S(poly)/S(substrate) = (Fe_{eq}+(A-B)/d)/Fe_{eq} \approx 2.6$, where Fe_{eq} is the equilibrium Fe solubility in silicon at the diffusion temperature, d is the thickness of the poly-Si layer, and $S(poly)$ and $S(substrate)$ are the solubilities of iron in polysilicon and in the substrate. A similar value (k=2.2) was obtained from computer modeling of gettering of iron during cooling.

Another experiment was performed with 1.1 microns thick polysilicon layer, which was quenched in 10% NaOH after anneal at 1100°C. In this case, no visible transient in iron concentration in the substrate was observed, and the segregation coefficient extracted from the ratio of iron concentrations in the substrate and in the poly was approximately 4. An experiment with a different structure (370 nm poly-Si on 197 nm SiO_2 on Si substrate) yielded k ≈16 at 1020°C. It is important to note that polysilicon (and to even greater extent multicrystalline silicon) is very inhomogeneous and contains both grain boundaries with significant lattice strain which segregate the impurities and relatively unstressed silicon within the grains which has no segregation effect. Hence, the macroscopic segregation coefficient observed in the experiments should depend not only on the microscopic structure of grain boundaries (such as misorientation of the grains forming the boundary), but also on the grain size and could vary depending on the thickness and growth conditions of the layer.

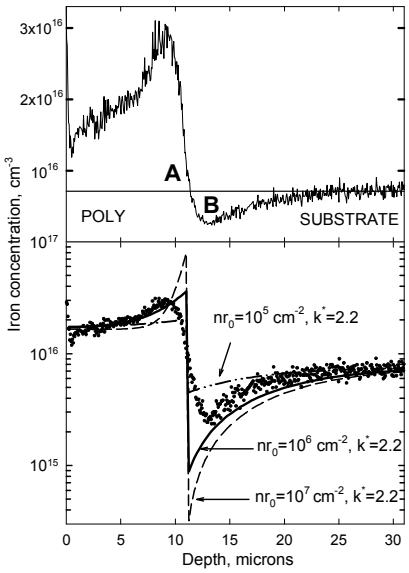

Figure E.7.1: Secondary ion mass spectroscopy depth profile of iron diffused in 11 μm polySi/Si structure at 1150°C and quenched in silicone oil. (a) depth profile plotted using a linear concentration scale. The solid horizontal line is the equilibrium iron solubility at the diffusion temperature. (b) The same depth profile plotted on a logarithmical scale together with the results of numerical modeling. The solid line represents the best fit, the dashed lines are variations of the nr_0 product.

The amount of segregation of Cu in multicrystalline silicon observed by Dorward and Kirkaldy was very substantial at low temperatures, around 3 orders of magnitude at 700°C, and dropped to a factor of two or less at temperatures above 900°C. Our studies of segregation of iron in polysilicon were performed at high temperatures, over 1000°C, and resulted in segregation coefficients from 2.6 to 16 which are similar or higher than the values observed by Dorward and Kirkaldy for copper in the same range of temperatures.

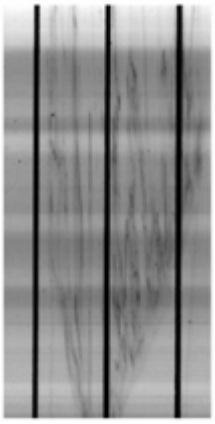

Figure E.7.2: LBIC map of a 2x1 cm^2 region in a Evergreen string ribbon solar cell.

It is instructive to make a simple estimate of the capacity of grain boundaries. The sample mapped by LBIC in Figure E.7.2 is 2 by 1 cm in size, 0.25 mm thick. We counted 40 grain boundaries within this sample, the average length of each boundary is 1.7 cm. The total area of all boundaries can be estimated as 1.7 cm^2, or 0.85 cm^2 per cm^2 of the surface area. If the metal density at the boundaries is 1 metal atom per 500 silicon atoms, the segregated Fe concentration will be 8.5×10^{11} cm^{-2} areal density, or 3.4×10^{13} cm^{-3} volume density.

E.8. Impact of the cooling rate on metal distribution in mc-Si (*topic 6.3, expands tasks 2.1 and 3.2*)

For this study, samples of mc-Si were intentionally contaminated with Fe, Cu, and Ni. "Slowly cooled" samples were cooled to room temperature inside of the furnace. "Quenched/reannealed" samples were quenched in silicone oil, etched to remove surface metal-silicides, inserted into a preheated furnace running at 655°C, annealed for 2.5 hours, and then slowly cooled in the furnace within approximately 12 hours. In the slowly cooled mc-Si samples (see our article in the August 2004 NREL workshop proceedings for details) Cu and Ni formed just a few localized precipitates along the grain boundaries and oxygen precipitates. Despite its higher solubility, copper formed lower density of precipitates than nickel, which agrees with a higher barrier for precipitation of Cu than of Ni.

The precipitation behavior of Cu and Ni in "quenched /reannealed" samples was found to be completely different. In mc-Si (Figure E.8.1) all grain boundaries and dislocations were evenly decorated. Once the samples were inserted back into preheated furnace running at 655^{o}C, quenched-in metals got mobile and at the same time remained highly supersaturated. Supersaturatio of metals determines the energy gained by a metal when it precipitates and therefore the height of potential barrier for precipitation which it can overcome. In such conditions metals can precipitate at sites which would be unfavorable at lower supersaturation levels, when the driving force for precipitation is low.

These observations confirm that faster cooling of ribbon/sheet/ingot is likely to lead to a higher density of small metal precipitates. Slow cooling would stimulate formation of a lower density of larger metal precipitates, which are likely to affect the minority carrier diffusion length to a lesser extent than high density of small precipitates. These results suggest that it might be possible to engineer the distribution of metals in an mc-Si wafer by a properly designed heat treatment.

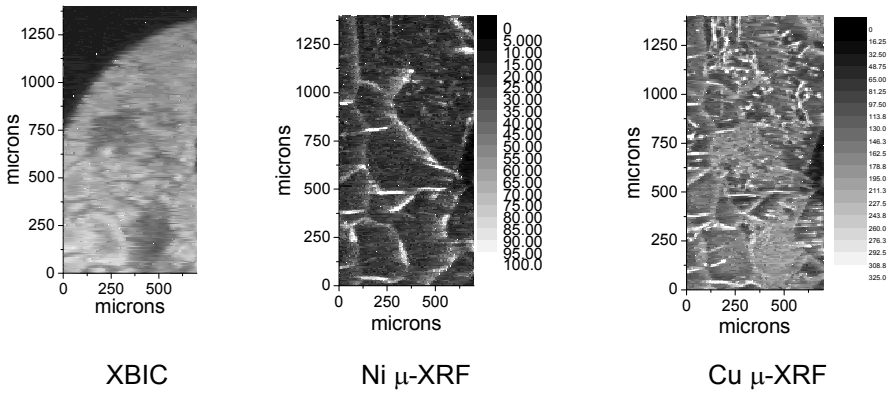

Figure E.8.1: XBIC, nickel μ-XRF, and copper μ-XRF maps of mc-FZ samples which were intentionally contaminated at 1200^{0}C, quenched and re-annealed at 655^{o}C.

E.9. Development of quantitative XBIC (SR-XBIC) *(task 4.1)*

The theory behind the SR-XBIC is similar to that of optical minority carrier diffusion length measurement methods, such as SPV [15, 16], with several differences specific to interaction of x-rays with the matter or specific to the experimental system used at the ALS:

1. The x-ray beam impinges the sample at an angle θ measured from the sample surface, typically at θ = 45 degrees. The depth from the surface at the point where the beam path is equal to its extinction length of $1/\alpha$, where α is the absorption coefficient of silicon, is given by $l = \sin\theta/\alpha$..

2. Each x-ray photon impinging a silicon sample generates multiple minority carriers; the total number is approximately given by E/E_p, where E is the beam energy and E_p=3.61 eV is the ionization constant of silicon (the energy required to produce an electron-hole pair in Si).

3. Absorption of x-rays in the ion chamber and in the air must be taken into account. This absorption depends on monochromator setting and becomes significant at beam energies below approximately 7 keV.

X-ray flux incident on the sample is measured by the current generated in the ion chamber installed in the beam path. The ion chamber at the ALS Beamline 10.3.2 is a cylinder about 2 cm long flushed with nitrogen at atmospheric pressure. X-rays are partly absorbed and ionize nitrogen in the chamber. These ions conduct current between two electrodes in the chamber. The electrical current flowing between the electrodes through the chamber is proportional to the x-ray beam intensity. The number of electron-ion pairs per absorbed photon generated in the chamber is calculated as E/E_{I0}, where E is the energy of x-ray photons and E_{I0} is the energy required to ionize one nitrogen molecule. The current flowing through the ion chamber is given by

$$I_0 = \frac{eE(1-T_{I0}(E))}{E_{I0}} \times F_0 \qquad \text{(Eq. E.9.1)}$$

where $T_{I0}(E)$ is the x-ray energy-dependent transmittance of the iron chamber (therefore, the $(1-T_{I0}(E))$ factor is the absorbance of the ion chamber), e is the electron charge, E_{I0} is energy necessary to make an electron-ion pair in the ion chamber, and F_0 is the x-ray flux which enters the ion chamber.

The x-ray flux incident on the sample is described as

$$F = F_0 \times T_{I0}(E) \times T_{air}(E) = \frac{I_0 E_{I0}}{eE(1-T_{I0}(E))} \times T_{I0}(E) \times T_{air}(E) \qquad \text{(Eq. E.9.2)}$$

where $T_{air}(E)$ is the transmittance of the air gap (typically, 2 cm) between the ion chamber and the sample.

The total number of electron-hole pairs generated in the sample is

$$N = F \times (1-R) \times \frac{E}{E_p} = \frac{I_0 \times E_{I0}}{eE_p(1-T_{I0}(E))} \times (1-R) \times T_{I0}(E) \times T_{air}(E) \qquad \text{(Eq. E.9.3)}$$

where R is the reflectivity of the sample (usually negligible with hard x-rays), and E_p is the ionization constant of silicon. This equation assumes that the x-ray beam is completely absorbed in the sample, i.e., that the thickness of the sample is much greater than the absorption depth of the x-ray beam.

XBIC is measured on a Schottky-contact or a p-n junction without reverse bias. The current flowing through the junction is proportional to the excess minority carrier density at the outside edge of the depletion region. The mathematical equation for this current is given by a formula based on the equations from [15, 16], but modified to take into account Eq.(3) and the geometry of the XBIC experiments:

$$I = C \times \frac{T_{\text{air}}(E) \times T_{\text{I0}}(E)}{1 - T_{\text{I0}}(E)} \times I_0 \times \frac{\alpha L_{\text{n}}}{(\sin\theta + \alpha L_{\text{n}})} \qquad \text{(Eq. E.9.4)}$$

where C is a sample-dependent constant which depends on reflectivity of the sample surface, recombination velocity at its surfaces, the minority carrier diffusion coefficient, and the minority carrier diffusion length.

Regrouping Eq.E.9.4, we obtain

$$\frac{CI_0}{I} \times \frac{T_{\text{air}}(E) \times T_{\text{I0}}(E)}{1 - T_{\text{I0}}(E)} = 1 + \frac{\sin\theta}{\alpha L_{\text{n}}} \qquad \text{(Eq. E.9.5)}$$

Performing the measurements at different x-ray beam energies and plotting

$$\frac{I_0}{I} \times \frac{T_{\text{air}}(E) \times T_{\text{I0}}(E)}{1 - T_{\text{I0}}(E)} \quad \text{versus} \quad \frac{1}{\alpha} \qquad \text{(Eq. E.9.6)}$$

we obtain a straight line dependence which crosses the horizontal axis at

$$l_0 = -L_{\text{n}} / \sin\theta \qquad \text{(Eq. E.9.7)}$$

And the diffusion length is calculated as

$$L_{\text{n}} = -l_0 \sin\theta \qquad \text{(Eq. E.9.8)}$$

In order to process the XBIC data correctly, it is important to properly take into account the transmission of a 2-cm thick gap filled with nitrogen (ion chamber) ($T_{\text{I0}}(E)$) and transmission of the air the gap between the ion chamber and the sample ($T_{\text{air}}(E)$) (typically around 2 cm). These values available online at http://www.cxro.lbl.gov/optical_constants/.

Errors due to incomplete x-ray absorption in the sample or recombination at its back surface can be minimized by using the x-rays with the lowest possible energies (monochromator at the Beamline 10.3.2 has the range of energies from 2.7 keV to 17 keV), i.e., the energies which have attenuation depth in the range of several 10s of microns. However, absorption in the

ion chamber and in the air picks up significantly at x-ray energies below 6-7 keV. The air gap between the ion chamber and the sample may vary from experiment to experiment and cannot be measured accurately. Additionally, absorption of x-ray by windows in the ion chamber is likely to become stronger at lower x-ray energies, although the exact amount of absorption is uncertain. We found from our experience that it is difficult to take into account absorption of x-rays on their path from the monochromator to the sample with sufficient accuracy at energies below 4.5 keV. Therefore, we conclude that the preferred energy range for SR-XBIC is from 4.5 to 7-8 keV for thin samples (200-250 microns) and 4.5-7 keV to 12 keV for thicker samples (≥0.5 mm).

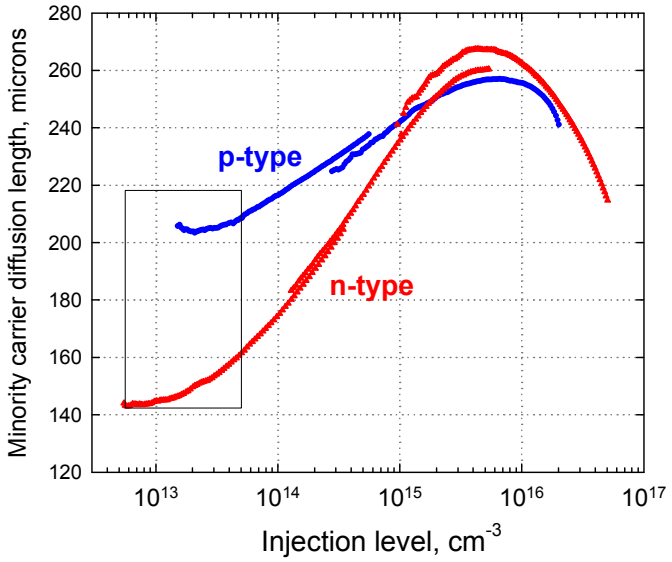

Figure E.9.1: Injection level dependence of minority carrier diffusion length of p-type and n-type samples determined from QSSP measurements (courtesy of D. Macdonald, Australian National University). The rectangle indicates the approximate range of injection levels in which our measurements were performed. The majority of measurements described in this report were performed in two-bunch mode of the synchrotron; in this mode, the x-ray flux is up to a factor of 10 lower than in the regular mode.

The SR-XBIC technique was tested using the following samples pre-characterized by standard minority carrier diffusion length / lifetime measurement techniques:

1. "SPV standard" - CZ-grown silicon sample with the diffusion length of 220 microns. This sample was cleaved from a larger sample which is used to calibrate our CMS-IIIA SPV system. The sample was chemically etched. A 30-40 nm thick, 3 mm in diameter aluminum Schottky diode was evaporated on the front side. The thickness of the sample after etching was 500 microns. The diffusion length obtained from the measurement of this sample was 227 microns, which is very close to the known for this sample diffusion length of 220 microns.

2. Two samples of CZ silicon, with n-type and p-type conductivity, pre-characterized by the quasi steady state photoconductance (QSSPC) technique (courtesy of Daniel Macdonald, Australian National University). These samples have known injection level dependence measured over the range of excess minority carrier concentration from 10^{13} cm^{-3} to 3×10^{16} cm^{-3}. The diffusion length of the p-type sample varied, depending on the injection level, from 200 to

255 microns, of the n-type sample – from 140 to 270 microns. The samples, as received, were passivated with silicon nitride. The passivating layer was removed by etching in concentrated HF and hot phosphoric acid, and Schottky diodes were evaporated using standard processing sequence. 30-40 nm Al contacts were used for the p-type diode, and 30-40 nm Pd contacts were evaporated on the n-type diode. The thickness of these samples after etching was 200 microns.

The samples from this set were used to estimate the injection level of SR-XBIC. We performed measurements using several ranges of x-ray energies from 4.5 keV to 8 keV, and determined that the obtained diffusion length varied from 100 to 125 microns for the n-type sample and 180 to 225 microns for the p-type samples, depending on which energy range was used. These values of diffusion length (and the ratio between them) are in agreement with the diffusion lengths determined for these samples in the injection level range of approximately 5×10^{12} - 5×10^{13} cm^{-3} (shown by a rectangle in Figure E.9.1). This injection level value is much smaller than majority carrier concentration in solar cells (about 10^{16} cm^{-3}) Hence, we conclude that SR-XBIC is a low-injection technique with the injection level somewhat higher or comparable to that of SPV, and lower than that of LBIC.

It is important to bear in mind when evaluating the SR-XBIC injection level that the photon flux at a synchrotron beamline is not a constant value and may vary by as much as a factor of 10 depending on the measurement conditions. For the highest possible beam intensity available at the ALS, the injection level can be extrapolated to the range of 2×10^{13} - 5×10^{14} cm^{-3} for this sample. For a typical photovoltaic material this is still a low injection level, $\Delta n << p$.

To summarize this section, we developed theoretical basis for spectrally resolved X-ray beam current technique (SR-XBIC) and demonstrated its accuracy using pre-characterized samples.

E.10. Application of SR-XBIC technique: correlation between metal precipitates and minority carrier diffusion length *(task 4.3)*

Spectrally-resolved XBIC (SR-XBIC) technique, combined with µ-XRF and µ-XAS, enables one to measure the elemental composition, chemical state, and effect on minority carrier diffusion length of metal-related defects in-situ, with micron- or sub-micron spatial resolution. Figure E.10.1 shows maps of copper and nickel distributions determined by µ-XRF, and minority carrier diffusion length determined by SR-XBIC, of a metal-contaminated multicrystalline float zone (mc-FZ) sample intentionally contaminated with copper, nickel and iron in order to achieve a very well-defined impurity distribution. µ-XAS analyses determine Cu and Ni to be in the form of Cu_3Si and $NiSi_2$ respectively, in agreement with previous results [17]. Fe did not form precipitates larger than the detection limit of these experiments, and could not be observed in µ-XRF maps.

Figure E.10.1 demonstrates a clear correlation between local metal concentration and minority carrier diffusion length, and areas with the highest Cu and Ni counts have the lowest diffusion lengths. The recombination strengths of Cu_3Si and $NiSi_2$ appear to be similar, as given by the slopes of the fit by 2D polynomial surface in Figure E.10.1 (note the different scales of the Cu and Ni axes). By comparing the SR-XBIC value at the points of maximum Cu and Ni (7 µm) versus the points with the least of these metals (25 µm), one deduces that the presence of Cu_3Si and $NiSi_2$ precipitates may locally reduce the minority carrier diffusion length by up to 72% compared to background levels.

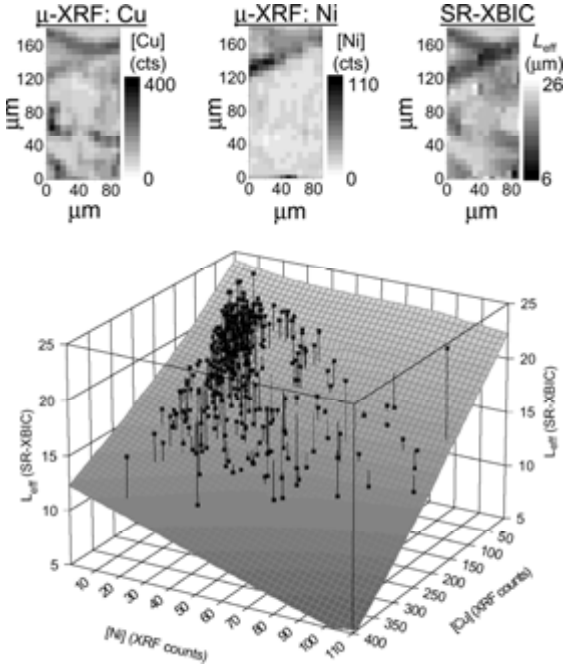

Figure E.10.1: SR-XBIC data (top right) can be obtained in-situ at the µ-XRF beamline, allowing for direct comparisons with metal distributions (top left, middle). The 3D correlation plot demonstrates a proportional correlation between increasing metal content and decreasing minority carrier diffusion length.

When one extrapolates the Cu and Ni concentrations to zero in Figure E.10.1, one determines a low baseline minority carrier diffusion length of approximately 30 µm. Meanwhile, "clean" mc-FZ samples can obtain local diffusion lengths higher than 100 µm. The likely explanation of this reduction is iron, present in very small clusters or point defects. When comparing "clean" and Fe-contaminated mc-FZ samples, one observes this same effect, while it is not evident in mc-FZ samples contaminated with Cu only. The low solubility and diffusivity of Fe favor the formation of smaller precipitates and point defects, unlike the larger precipitates formed by fast-diffusing and highly soluble Cu and Ni. The small distances separating neighboring Fe defect clusters increases their effect on device performance.

E.11. Application of synchrotron-based Fourier transform infrared spectromicroscopy to analyses ofoxygen concentration near grain boundaries in mc-Si *(task 4.2).*

Our preliminary Fourier transform infrared (FTIR) studies of cast ingot cross-sections showed that there are large fluctuations in interstitial oxygen concentrations throughout an ingot. It is evident, as demonstrated in Figure E11.1, that the edges and bottoms of the ingots have higher concentrations of oxygen than the center, presumably due to diffusion from the crucible. Others confirmed the observation of this behavior in Ref. [18]. The observation that there is a significant long-range change in oxygen concentration across an ingot has driven the hypothesis that short-range changes (e.g. near grain boundaries) may be detectable by high spatial resolution synchrotron-based techniques. To test this hypothesis we have initiated an FTIR spectromicroscopy study at Advanced Light Source beamline 1.4.3 (see http://infrared.als.lbl.gov).

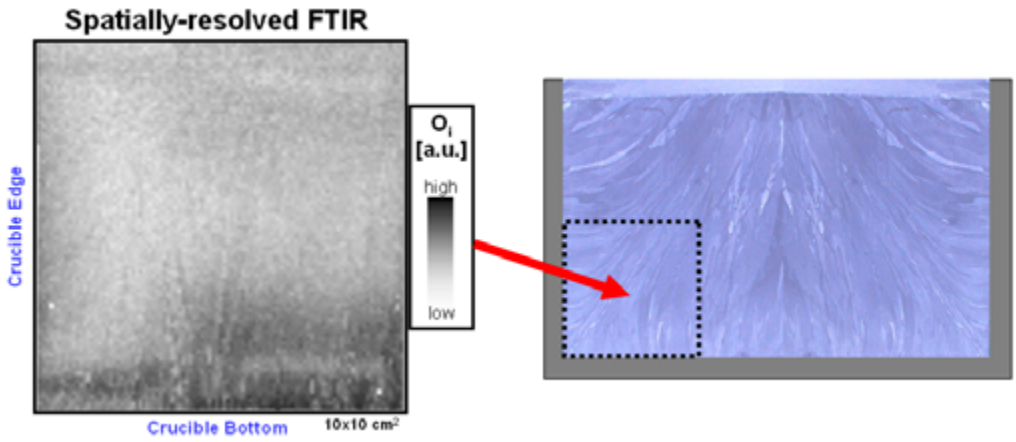

Figure E11.1: Long-range fluctuations in interstitial oxygen are detectable by large area conventional FTIR scans. We attempted to study short-range fluctuations in oxygen concentration by high spatial resolution synchrotron-based FTIR. Sample provided by J. Isenberg, Fraunhofer ISE.

One of the primary reasons for doing infrared spectroscopy at a synchrotron light source is the large enhancement in brightness (flux per unit area). This brightness advantage manifests itself most beneficially when focusing the light to a very small spot size. BL 1.4.3 staff scientists have been able to achieve essentially diffraction-limited spot sizes in the mid-IR using the ALS source. Figure E11.2 demonstrates the tight focus achieved using the synchrotron source and the 32x objective. The cross sectional Gaussian widths of the spot were 6.2 by 10.1 microns. Since the mid-IR wavelengths used are centered in the 3 to 10 micron range, and the objective lenses have a numerical aperture of approximately 1, one would expect the diffraction limited spot size to be approximately the wavelength of light, i.e. around 10 microns or better.

When the same measurement is made using the internal Globar^{TM} IR source, the spot size is 80 by 100 microns. One could reduce the spot size from the Globar source by using apertures; however, this would also greatly reduce the light intensity. Thus, with the synchrotron source one can get a signal enhancement with a 10-micron spot size of a factor of 200, as compared with the Globar source with a 10-micron aperture. Thus while the synchrotron source does not

provide a significant gain in flux compared to the Globar, it is possible to get all of the light from the synchrotron through a 10-micron aperture. In other words, when measuring areas with diameters less than 100 microns, the synchrotron provides substantial improvement in signal over the conventional Globar source.

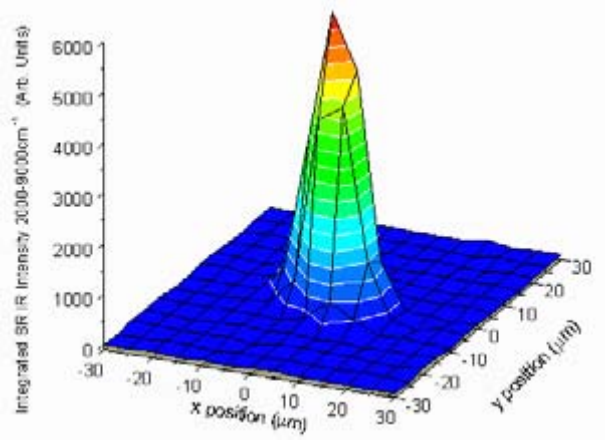

Figure E11.2: Profile of the IR spot size with the synchrotron as the light source (courtesy of M. Martin, BL 1.4 staff scientist).

The technical parameters of the beamline are as follows: energy range: 0.01 – 1 eV (which corresponds to the frequency range from 100 to 10,000 cm^{-1}). The interferometer resolution is 0.125 cm^{-1}. The endstation is equipped with Nicolet Magna 760 FTIR and Nic-Plan IR microscope with 15× and 32× objectives. Sample is mounted on computer-controlled motorized stage with 1 μm spatial resolution and can be measured in reflection or transmission modes. Available detectors include MCT-A (mercury cadmium telluride), Ge:Cu and Si bolometer detectors.

For our first study of oxygen and carbon in silicon we obtained approximately 2 mm thick cast mc-Si samples cut from the same ingot at 4 different positions. The 4 different slices were cut from the bottom of the ingot at the edge of the crucible, the bottom of the ingot towards the center of the ingot, the top of the ingot at the edge of the crucible, and the top of the ingot towards the center.

The samples were prepared by first mechanically polishing both sides to a roughness of less than 1 micron to minimize surface scattering of the infrared beam. After polishing, the samples were cleaned in acetone and very lightly etched in 10:1 HNO_3:HF for 5 seconds to reveal the grain boundaries. To properly subtract the background in FTIR spectra, an FZ silicon reference sample with very low oxygen and carbon content was prepared using the same procedure and was made to be the same thickness as the cast Si samples.

For each scan the guidelines set forth in ASTM documents F1391-93 and F1188-00 were followed in order to obtain data that could be calibrated quantitatively. The basic procedure for calibrating the data was to first obtain an open beam spectrum and a reference sample spectrum for each scan that was initiated. The two spectra were then used to obtain the absorption coefficient spectrum for each point in the scan. Concentrations were then determined by multiplying absorption peak height by the international calibration constants published in the ATSM documents: $[O_i] = 3.14 \times 10^{17} \times \alpha_{peak}$ and $[C_s] = 8.2 \times 10^{16} \times \alpha_{peak}$, both in cm^{-3}.

Despite our expectations, the experimental results indicated that there is little variation in bulk oxygen content across small distances in as-grown cast mc-Si. During our examination of a variety of positions in all 4 slices of the ingot we observed no significant variations near surface features revealed by etching or from grain to grain. Figures E11.3 and E11.4 are representative of our observations for one and two-dimensional scans, respectively. Figure E11.3 demonstrates a

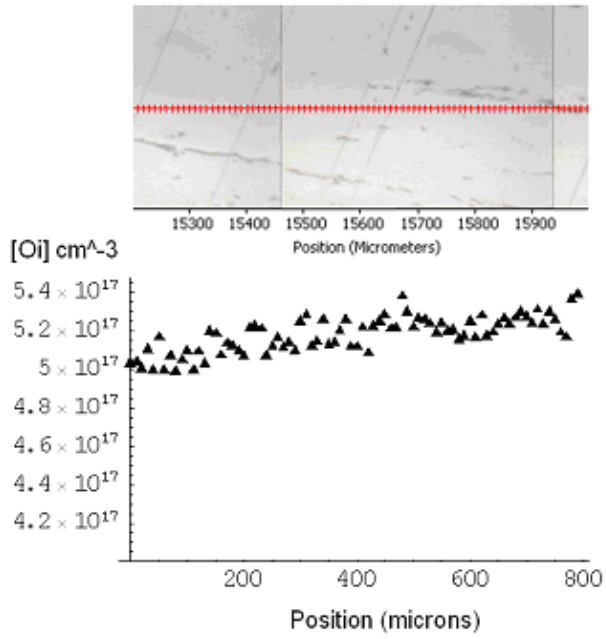

Figure E11.3: 10-micron resolutions scan across multiple grain boundaries shows that the concentration does not vary noticeably over short distances but that long-range variations are noticeable.

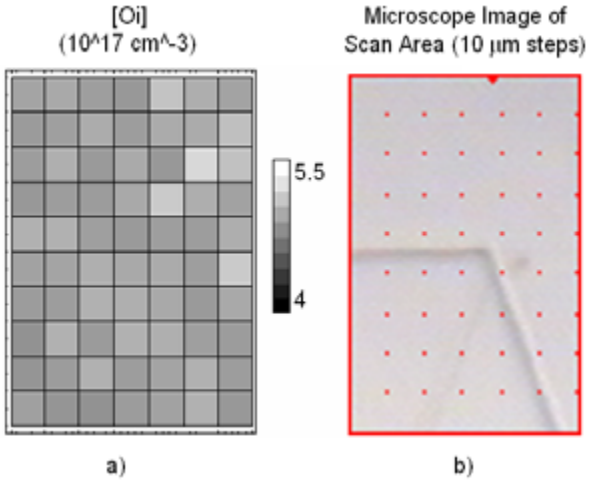

Figure E11.4: a) 10-micron step density plot of oxygen concentration from a 70x100 μm^2 scan across a grain boundary. b) A microscope image of the area scanned. Note that the concentration varies less than 10% throughout the area.

line scan across several grain boundaries over a few hundred microns. The 10-micron resolution scan was taken from interior of the ingot towards the edge of the sample that was adjacent to the crucible during solidification. A long-range linear increase in oxygen concentration is observed but no short-range variations at the grain boundaries can be seen. The two dimensional scan shown in Figure E11.4 also demonstrates that there is little variation in oxygen content at grain boundaries. There is less than a 10% deviation from the point with highest concentration of oxygen to the point with the lowest concentration.

The lack of short-range variations of oxygen concentration in these samples indicates that during the slow cooling of the ingot casting process interstitial oxygen was able to diffuse through the crystal in a relatively uniform manner. These results are similar to conventional FTIR scans on multicrystalline sheet material [19]. In upcoming studies we plan to examine the effect of processing on local interstitial oxygen concentration in the region of structural defects.

E12. Metal particle evolution during silicon nitride hydrogenation and phosphorus diffusion gettering processing of mc-Si solar cells (task 3.3).

Ingot-cast mc-Si samples from bottom, top, and edges of the ingots provided by two commercial vendors were used in this study. Sets of sister wafers were processed as follows: (1) as-grown, (2) SiN_x-fired, (3) phosphorus-diffused, without a nitride layer, (4) both SiN_x-fired and P-diffused, and (5) fully-processed solar cells (with Al back surface layer).

Synchrotron-based analytical techniques were used to measure the metal distributions and chemical states in samples extracted from nearly-identical regions of these sister wafers. X-ray fluorescence microscopy (μ-XRF) was used to determine the elemental nature and spatial distribution of metal-rich particles, and X-ray abosorption microspectroscopy (μ-XAS) was used to determine the chemical state. Microwave photoconductive decay (μ-PCD) and light beam induced current (LBIC) were used to identify under-performing regions in the samples.

(1) As-grown Material:

As expected, two types of metal-rich particle [20] were observed in as-grown ingot-cast mc-Si: metal silicide nanoprecipitates and metal-rich inclusions, often micron-sized and/or in an oxidized chemical state. The metal silicide nanopreciptiates contained some combination of copper, nickel, cobalt and iron, incidentally the four 3*d* transition metal species with highest atomic flux (product of solubility and diffusivity) in silicon. The metal-rich inclusions contained much larger amounts of slowly-diffusing species, such as calcium, titanium, and zinc, occasionally accompanied by high-flux elements.

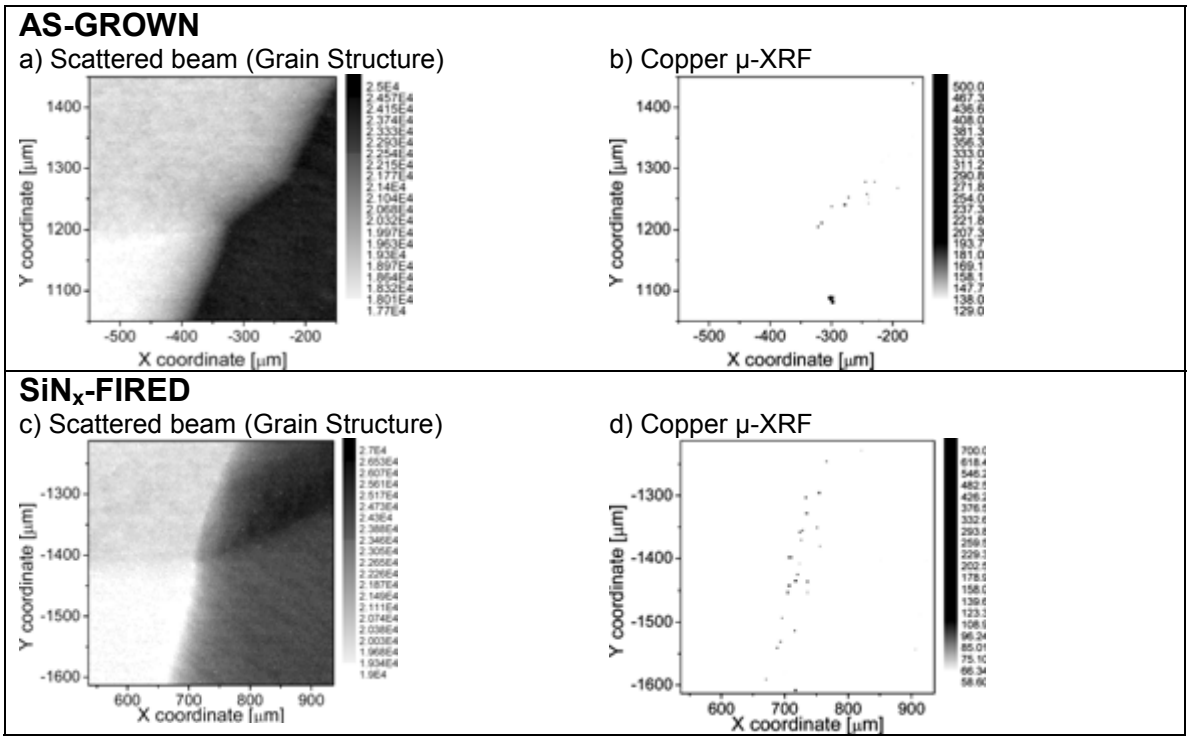

Figure E12.1: Comparison of Cu distributions in as-grown (b) and SiNx-fired (d) ingot-cast mc-Si from near an ingot top. The elastically-scattered X-ray beam intensity (a and c) provides a map of the grain structure.

(2) SiN_x Firing:

We employed μ-XRF to compare metal distributions within the same region of an as-grown wafer and a SiN_x-fired sister wafer. The as-grown wafer contained Cu_3Si nanoprecipitates along a grain boundary, and occasional inclusions of slowly-diffusing species within the grains.

Metals did not appear to be much affected by SiN_x-firing. Inclusions were evident in both wafers. Cu_3Si precipitates were also present in both wafers, only slightly larger and more numerous in the SiN_x-fired wafer than in as-grown wafer (Figure E12.1). The heat treatment associated with SiN_x firing may have induced the precipitation of additional metal atoms dissolved atomically within the grains, or in smaller precipitates, a similar phenomenon to Ostwald ripening. In the absence of a strong gettering layer, metals appear to have remained largely within the sample.

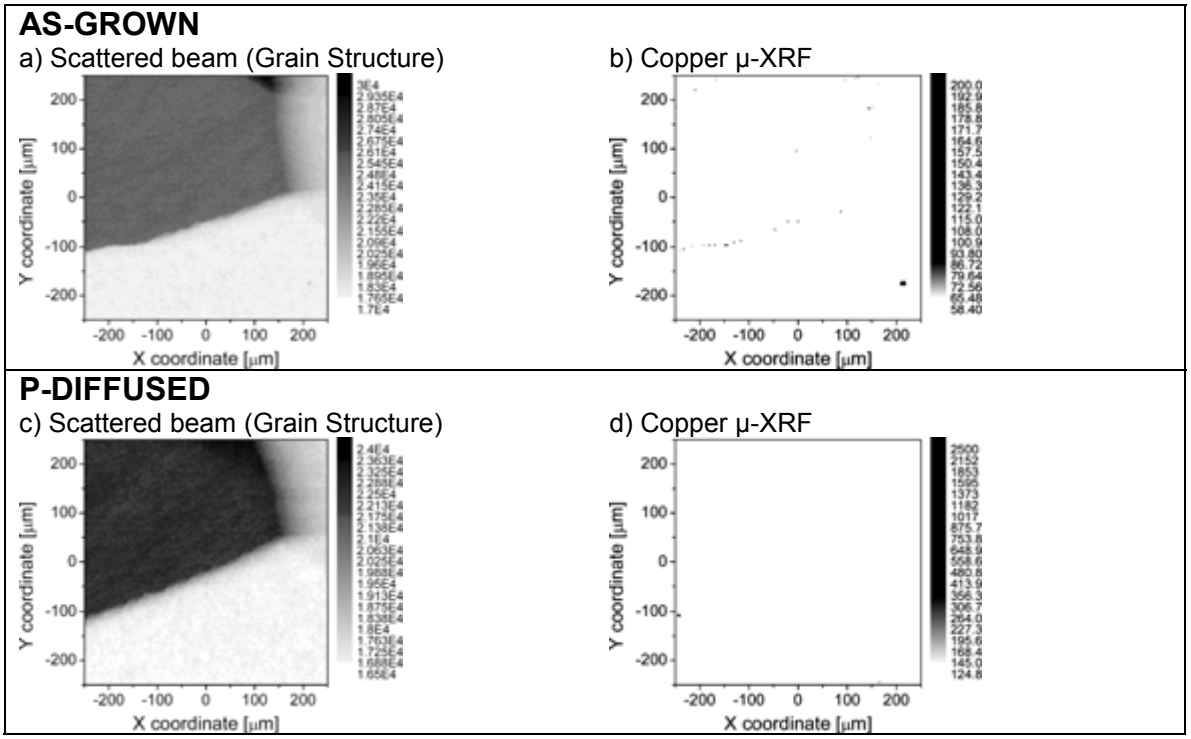

Figure E12.2: Comparison of Cu distributions in as-grown (b) and P-diffused (d) ingot-cast mc-Si samples from near an ingot top. While copper-rich precipitates are observed along a GB in as-grown material, few such particles are observed in the P-diffused sample. The one Cu-rich particle appears in the P-diffused sample also contains Ca, Cr, Fe, and Ni, which indicates an inclusion.

(3) P-diffusion Results:

Phosphorus diffusion appeared to significantly alter metal distributions within the mc-Si samples analyzed in this study.

Metal silicide nanoprecipitates with the highest fluxes, e.g. copper and nickel, appear to be dissolved below the detection limits (radius < 30 nm) during phosphorus gettering, as shown in Figure E12.2. Metal silicide nanopreciptiates of lower-flux species (such as iron) are more

resistant to dissolution during P-diffusion [21] and may serve as virtual sources of metal point defects within the bulk, as proposed by Plekhanov et al. [3].

On the other hand, large metal-rich inclusions are frequently observed after processing, although complete statistical analyses of their size and spatial distributions before and after processing have not been performed. Despite their composition of low-flux elements and frequently oxidized chemical state [8, 20], some limited dissolution of these particles is likely during high-temperature processing steps. To a certain degree, these particles may serve as virtually inexhaustible sources of metals during solar cell processing.

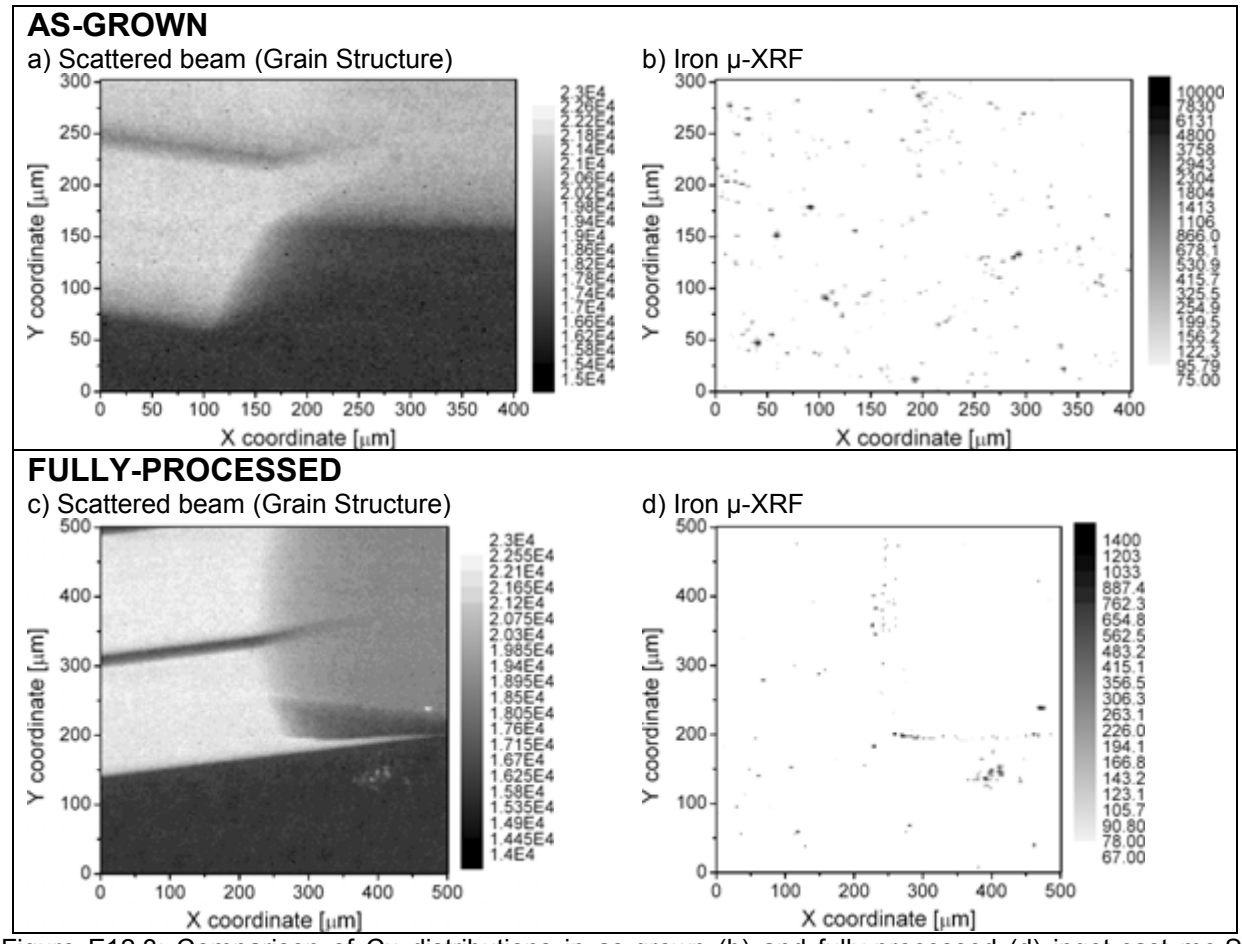

Figure E12.3: Comparison of Cu distributions in as-grown (b) and fully-processed (d) ingot-cast mc-Si samples from near an ingot edge. The high density of Fe-rich particles, which evidently cannot all be gettered, is observed to re-distribute itself along certain structural defects during processing.

(4+5) P-diffused + SiN_x firing, and Fully-Processed cells:

The metal distributions in P-diffused+SiN_x-fired and also in fully-processed cells resemble those found in P-diffused cells. Metal silicide nanoprecipitates of high-flux species are seldom observed in these samples, and metal silicide nanopreciptiates of low-flux species are reduced in size. Inclusions of foreign particles can still be observed in fully-processed material.

An interesting effect occurs in material with very high concentrations of metals (e.g. towards the edges of the ingot). Metals present in very high concentrations may re-arrange

themselves within the samples as the result of processing, as shown in Figure 3.3. An as-grown sample is shown above, revealing a distribution of iron oxide and silicide particles within the grains, likely originating from the crucible and/or crucible lining material. The same region in a sister wafers is shown after complete solar cell processing, which reveals a lower density of intragranular particles and a much higher density of iron silicide precipitates agglomerated along a certain grain boundary. Evidently, a considerable fraction of iron atoms dissolved during processing, were unable to be gettered by the P-diffusion layer (perhaps because of the high overall concentration), segregated to an energetically favorable structural defect, and precipitated there. This re-arrangement of metal species during solar cell processing necessitates an intelligent cool-down procedure at the end of processing wafers with high known metal contents that may be slower than usual, in order to promote the formation of larger metal precipitates and a reduction of dilaterious metal point defects.

Of all solar cell processing steps analyzed in this study, phosphorus diffusion appears to be the most effective step to dissolve metal silicide precipitates and alter their distributions. This correlates nicely with previous work, which demonstrated both a significant reduction of total metal concentration [22, 23] and improvement of electrical properties [24] as a result of phosphorus diffusion.

Slightly larger and more numerous metal silicide nanoprecipitates were observed after SiN_x firing, indicating a reduction in the concentration of metal point defects and nanoprecipitates below the detection limits. This could be simply an effect of the annealing, or it could be an effect of metal redistribution promoted by the presence of hydrogen as suggested by Vyvenko et al. [25]. Future work is needed to further investigate these effects, especially during co-firing with p-diffusion or aluminum backside gettering.

E.13. Concept of defect engineering of transition metals in mc-Si solar cells (task 6.1).

Our neutron activation analysis studies, presented in this final report and published in [26], demonstrated that the mc-Si material performance in solar cells is determined not only by the total concentration of transition metal contaminants, but also by their special distribution and chemical state. For example, we observed that areas of the wafers with high minority carrier diffusion lengths often have the same or higher transition metal concentrations than underperforming areas with several times lower diffusion length. On the other hand, in both cases the metal concentration was so high that it could reduce the minority carrier diffusion length and solar cell efficiencies to much lower values, if all metals were dissolved interstitially or substitutionally.

In the past, the main approach to dealing with metals were gettering and hydrogen passivation. However, recent work has proven that phosphorus diffusion gettering [22] is rather limited in removing metals: between 10-40% of interstitial diffusing metals (Cu, Fe, Co, Cr, Ag, etc.) and nearly 100% of substitutional diffusing metals (Zn, As, Sb, Sn, etc.) remain in the material after gettering.

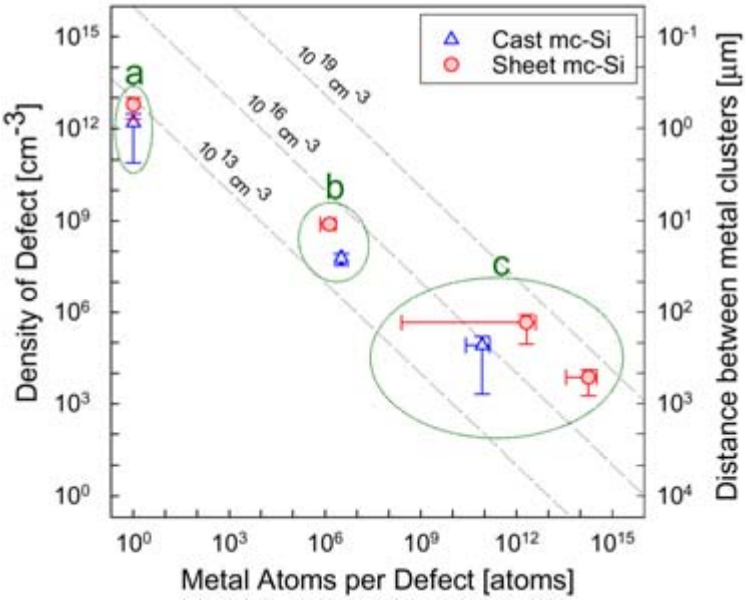

Figure E13.1: The spatial density (cm-3) of metal-related defects is related to their average size (number of atoms) and the average distance between them. Experimental data for cast mc-Si and sheet mc-Si) are also plotted. Dotted diagonal lines indicate constant metal concentrations. Different defect types are labelled by letters and circles: (a) refers to dissolved metal point defects; (b) refers to metal silicide nanoprecipitates; (c) refers to micron-sized inclusions of foreign particles.

Our research lead us to a novel approach to dealing with metals, which can be used in conjunction with existing solar cell processing techniques. Instead of removing all metals from multicrystalline silicon – a prospect that is frustrated by physical limitations and cost restrictions – we suggest that one can live with large amounts of metals inside the material, as long as their size and spatial distributions are properly engineered. Furthermore, we obtained experimental

proof of the principle that metal nanodefect engineering can be used to recover minority carrier diffusion lengths even in heavily contaminated materials.

While the data in Figure E13.1 indicate that the majority of metals are contained in micron-sized inclusions, the average distances between these particles is very large, so they cannot have a significant direct impact on minority carrier diffusion length. Unlike these large inclusions, smaller nanodefects (represented on the left-most side of Figure E13.1) are present in significantly higher spatial densities and are much more dangerous to solar cell device performance. These observations lead us to the conclusion that to maximize solar cell efficiency without changing the total metal concentration, in the ideal case all metals must be completely contained in large, micron-sized clusters separated by several hundreds of microns, thus minimizing the interaction between metal atoms and charge-carrying electrons.

To test this hypothesis, we compared metal nanodefect distributions within heavily contaminated mc-Si material, and correlated these to the minority carrier diffusion length. We observed that metal impurity distributions can be predictably engineered, for example, by controlling the sample cooling rate from high temperatures. Three samples contaminated with copper, nickel, and iron at 1200°C, were subjected to different cooling rates: quench (200°C/s cooling rate), slow cool (3-8°C/s), and quench and re-anneal at 655°C followed by slow cool. The metal nanodefect distributions in these three samples were mapped using µ-XRF, and the minority carrier diffusion lengths were determined by SR-XBIC.

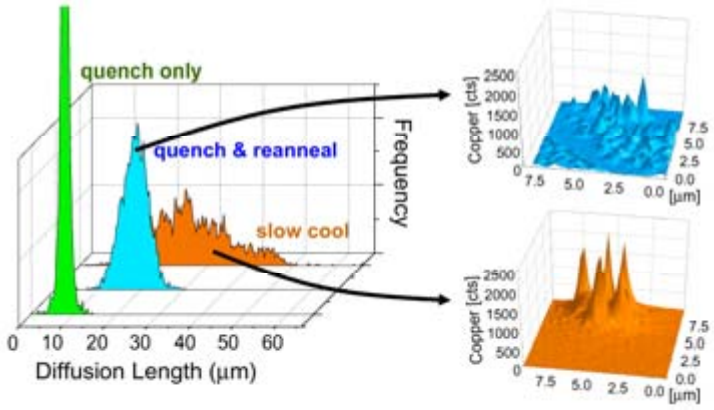

Figure E13.2: Effect of nanodefect distribution on material performance. Material performance (minority carrier diffusion length histograms, left) in three differently cooled samples (quench, quench & re-anneal, slow cool) is compared with size and spatial distributions of metal nanodefects (high-resolution µ-XRF maps, right). The material with microdefects in lower spatial densities clearly outperforms materials with smaller nanodefects in higher spatial densities, despite the fact that all materials contain the same total amount of metals.

Very fast cooling rates result in a homogeneous distribution of predominantly dissolved metals and their complexes. The histogram labelled "quench" in Figure E13.2 shows a narrow distribution of minority carrier diffusion lengths under 10 µm, unacceptable for solar cell devices. The sample quenched and subsequently re-annealed exhibits a fine distribution of nanodefect clusters, tens of nanometres in size, with lower spatial densities than in the quenched

sample. Simultaneously, the minority carrier diffusion length increases almost two-fold (Fig E13.2). Finally, a low density of micron-sized defect clusters was observed in the slowly-cooled sample, which has a maximum minority carrier diffusion length a factor of four higher than the quenched sample. These results provide direct evidence for the correlation between changes in metal nanodefect distribution and enhancement of material performance.

The concept proposed in this study opens a new and exciting opportunity to recover low-quality silicon for commercially viable solar cell material, which could be used in addition to existing solar cell processing techniques. Since material performance is shown to be limited primarily by the metal nanodefect distribution, and not by total metal concentrations, even heavily contaminated materials can be improved via nanodefect engineering.

E14. Feasibility of contamination of cast mc-Si from the silicon nitride crucible coating *(task 5.2).*

Samples of α-Si_3N_4 powder were obtained from commercial chemical suppliers (Alfa Aesar and Cerac) and from one of our industrial collaborators. The total impurity contents of α-Si_3N_4 powders from commercial suppliers were known from inductively coupled plasma optical emission spectroscopy (ICP-OES) data, provided by the vendors). Figure E14. 1a shows the results of these analyses, i.e., the most common impurities in α-Si_3N_4.

For comparison, Figure E14.1b shows impurity content of ingot-cast mc-Si as determined by NAA. Not all elements detected by ICP-OES in Si_3N_4 could be detected in mc-Si by neutron activation analysis because NAA is not equally sensitive to all elements [27], and vice versa; hence, the lack of bars in Figure 1a or 1b corresponding to certain elements does not imply that these elements were not present.

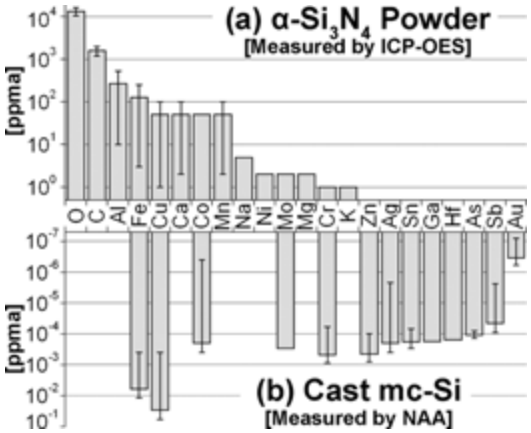

Figure E14.1: (a) Vendor-specified impurity contents of 4 different commercially-available α-Si3N4 powders with purities between 95% and 99.9%. The range of variation, which depends on the purity of the powder, is shown by the error bars. (b) Typical impurity content of different directionally-solidified ingot-grown mc-Si materials determined by NAA [22, 26, 28]. The error bars show the range of values obtained on different samples. Note the different concentration scales in Figure 1a and Figure 1b.

Figure E14.2 shows a μ-XRF map of Fe and Ca distributions in an α-Si_3N_4 powder, provided by our industrial collaborator and typical of what is used in industry to coat the ingot-casting crucibles. Similar distributions were observed in the powders purchased from commercial vendors. In such powders, iron can be found both distributed homogeneously as well as concentrated in discrete small and large particles. The homogeneously-distributed background iron concentration is most readily detectable in lower-purity α-Si_3N_4, and is determined by μ-XAS to be in the $FeSi_2$ chemical state. In addition, discrete Fe-rich particles can be observed in all α-Si_3N_4 materials. The sizes and abundances of these particles decrease with increasing powder purity; the industrial sample demonstrated particle sizes and abundances comparable to the higher-purity commercial samples. These particles exist in two varieties: larger particles of a chemical state most similar to Fe_2O_3 (Figure E14.3a), and smaller particles of Fe+Cr+Ni (reminiscent of stainless steel, Figure E14.4) with iron in an Fe^0 charge state (such as in iron silicide, metallic iron, iron carbide, etc.) (Figure E14.3b). Other less-frequently-observed

impurity-rich particles contain Cu metal, Zn, Ti, Cr, Ni, Co, or Ca. All α-Si_3N_4 powders analyzed in this study exhibit at least two of these types of particle, in addition to the more abundant Fe-rich particles.

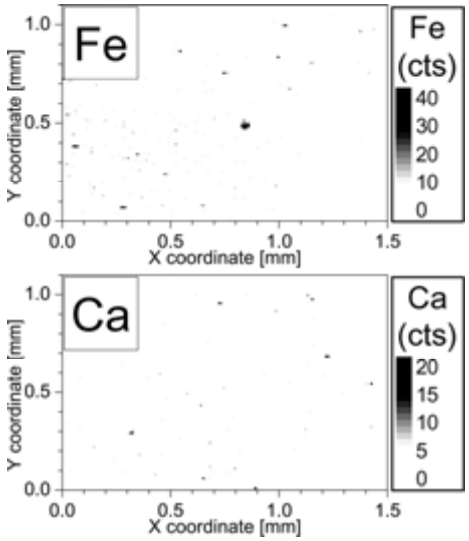

Figure E14.2: μ-XRF map of α-Si_3N_4 powder (representative of what is used in industry to coat casting crucibles) reveals the spatial distribution of iron- and calcium-rich particles. Both large and small iron-rich particles are observed. Large Fe-rich particles (such as the one at X = 0.7 mm, Y = 0.5 mm) contain only iron in a chemical state most similar to Fe_2O_3 (Figure E14.3a). The smaller particles consist of Fe+Ni+Cr (Figure E14.4), with iron in a Fe0 charge state, i.e. most similar to metallic Fe (Figure E14.3b). Background Fe, detectable in some lower-purity α-Si_3N_4 powders, is determined to be $FeSi_2$. More isolated particles containing Cu metal, Zn, Ti, Cr, Ni, and Co were also observed.

The spatial distributions and chemical states of impurity-rich particles in ingot-cast mc-Si turned out to be very similar to those in the silicon nitride coating. In ingot-cast mc-Si, three types of impurity-rich particle are observed by our experimental techniques: (a) metal silicide nanoprecipitates, typically 30-60 nm in diameter, most often found along structural defects (especially grain boundaries), (b) metal-rich inclusions, often measuring up to a few tens of microns in diameter, and (c) extended microdefects (e.g., silicon carbide or nitride) measuring up to several tens or hundred of microns in diameter. A much higher concentration of these precipitates is observed towards the bottom, top, and edges of the ingot. The total amount of metals contained in these precipitates is estimated by μ-XRF to reach values as high as 3×10^{14} cm^{-3} or higher. On the other hand, in the middle of the ingot, such precipitates are rarely observed above the current μ-XRF detection limits.

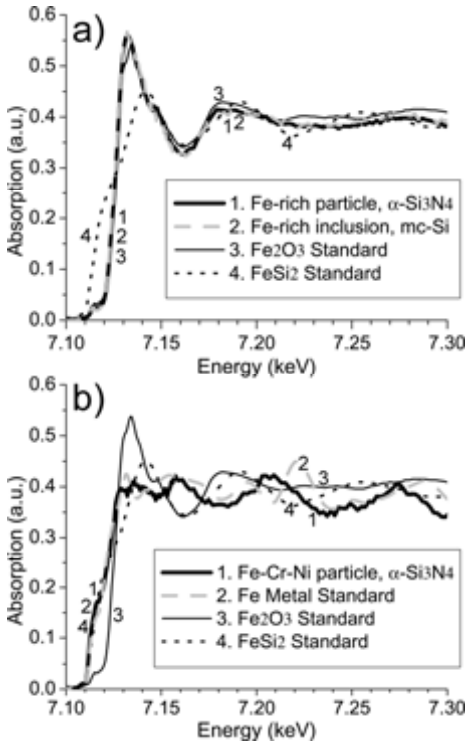

Figure E14.3: μ-XAS spectra of two types of Fe-rich particle in α-Si3N4 material. The particle in (a) contains a large amount of iron (Figure E14.2), and the chemical state is most similar to iron oxide (Fe2O3). The particle in (b) consists of Cr, Ni, and Fe (Figs. E14.2, E14.4), and the near-edge features match most closely with those of iron in the Fe^0 charge state (e.g. Fe metal, Fe silicide), although the extended X-ray absorption fine spectrum does not match perfectly with any of the standards. Note that the μ-XAS of the oxidized iron particle found in α-Si_3N_4 and that of an oxidized iron inclusion detected in ingot-cast mc-Si material match nearly perfectly, indicating that both the charge state and local crystallographic environment are nearly identical, and providing strong evidence that metal-rich particles in the α-Si_3N_4 crucible lining material can enter the melt during growth.

Micron-sized particles in mc-Si are often composed of oxidized Fe or Ti. In addition, particles containing Ca, Zn, Mn, Mo, and/or Cr, with traces of fast diffusers were also observed. The abundance of slowly-diffusing elements, combined with their frequently oxidized chemical state lead us to conclude that these particles are inclusions and not precipitates [17, 20]. The spatial density of these particles is orders of magnitude lower than metal silicide nanoprecipitates. However, each inclusion particle contains a far greater number of metal atoms than a metal silicide nanopreciptiate. Consequently, these particles were found to account for local metal contents as high as 2.3×10^{16} cm^{-3} [20] in regions of the ingot where they are most prevalent (top, bottom, and edges).

Metals are also found at Si_3N_4 and SiC microdefects towards the top of the ingot. These microdefects are specific for ingot-cast mc-Si. An IRTM image (Figure E14.5a) of one collection of microdefects reveals a β-Si_3N_4 rod surrounded by several β-SiC clusters. $FeSi_2$ and Ca (chemical state not determined) are found rather homogeneously distributed within the β-Si_3N_4 rod (Figs. E14.5b,d), while $FeSi_2$ and Cu_3Si particles are observed within the SiC clusters surrounding the Si_3N_4 rods (Figs. E14.5c,d).

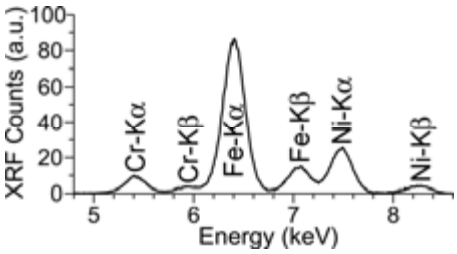

Figure E14.4: Typical μ-XRF point spectrum of the smaller Fe-rich particles in Figure E14.2. Iron, chromium, and nickel are present in proportions suggestive of stainless steel. The μ-XAS spectrum for this particle appears in Figure E14.3b.

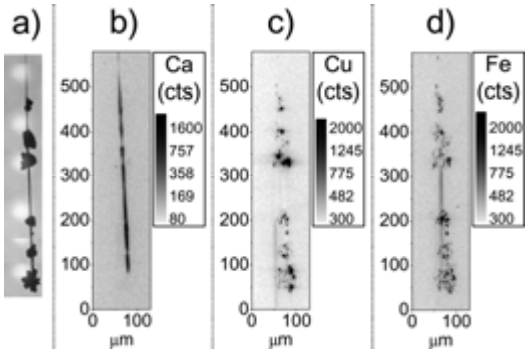

Figure E14.5: (a) IRTM image of a β-Si3N4 rod encircled by SiC clusters, found in the upper part of a cast mc-Si ingot; (b-d) μ-XRF maps of the same region. Homogeneously-distributed Ca and $FeSi_2$ are present at the β-Si_3N_4 rod. Particles of $FeSi_2$ and Cu_3Si are also present at the SiC clusters. All of these impurities are also present in α-Si_3N_4 powder in high concentrations (Figs. E14.1, E14.2).

The results presented in this study strongly indicate that the silicon nitride coating could contaminate cast mc-Si ingots with an assortment of metallic and non-metallic impurities during crystal growth. Firstly, the *relative concentrations of elemental impurity species* in α-Si_3N_4 are similar to those impurities found in ingot-cast mc-Si, as shown in Figure E14.1. Secondly, the *chemical states* of certain impurity-rich particles in α-Si_3N_4 and inclusions in ingot-cast mc-Si are practically identical, as shown in the overlapping μ-XAS spectra in Figure E14.3a. Thirdly, the *distribution* of impurities in ingot-cast mc-Si ingots suggests an external contamination source in contact with the melt and crystal, given the predominance of precipitates and inclusions near the side edges of ingots. Fourthly, the observation of *silicon nitride and silicon carbide microdefects* in the upper regions of the ingot reflects high concentrations of carbon and nitrogen impurities in the melt. (It is generally believed that dissolved nitrogen and carbon become supersaturated in the melt during the later stages of ingot growth, leading to the formation of these microdefects). During directionally-solidified cast mc-Si ingot growth, nitride and carbide particles likely decompose from the crucible lining material in contact with the melt. This is consistent with the observation that mc-Si materials not grown in Si_3N_4-coated crucibles seldom exhibit silicon nitride and silicon carbide microdefects, with the exception of silicon carbide microdefects observed in mc-Si materials grown using graphite crucible parts [13] or growth substrates [29]. Upon decomposition of the silicon nitride crucible lining material in contact with

the melt, other impurity atoms or particles associated with the nitride can also enter into the melt. This hypothesis is strongly supported by the concomitant presence of N, C, Fe, Ca, and Cu at these microdefects (Figure E14.5) and within α-Si_3N_4 powders (Figs. E14.1, E14.2).

These data suggest two possible mechanisms of incorporating impurities from the α-Si_3N_4 coating into mc-Si:

(1) Impurity atoms and impurity-rich particles in the crucible lining material may dissolve into the silicon melt or warm crystal and form metal point defects, precipitates, and/or microdefects. This mechanism likely dominates for small particles (e.g. Fe+Cr+Ni-rich particles), particles with low melting temperatures, and impurities distributed atomically or in very small clusters (e.g. background $FeSi_2$ in lower-purity α-Si_3N_4).

(2) Impurity-rich particles in the α-Si_3N_4 may be wholly incorporated into the melt as second-phase particles. If these particles exist for only a short time in the melt, and/or if the melt is already saturated with the given impurity species, then these second-phase particles can be incorporated into the advancing solidification front as inclusions.

The concentration of impurities in the melt dissolving from the α-Si_3N_4 coating depends on the total thickness of α-Si_3N_4 that dissolves during crystal growth, the elements that may be added during the coating process as sintering aid, as well as on the surface area to volume ratio of the crucible. Effective means of reducing the impact of this contamination source on ingot-cast mc-Si might include reducing the impurity content in α-Si_3N_4, improving the structural quality of Si_3N_4 to minimize its decomposition during growth, and reducing the surface area to volume ratio of the crucible (e.g. increasing the crucible size).

E.15. Investigate interaction between different metals in solar-grade multicrystalline silicon with the formation of intermetallic silicides *(task 5.3)*

Application of x-ray synchrotron techniques to metal-contaminated multicrystalline silicon (mc-Si) samples enabled us to obtain evidence of chemical interaction between Fe, Cu, and Ni with the formation of a so far unknown intermetallic phase. Analysis of x-ray absorption spectra of this phase by means of computer modeling enabled us to determine its crystal structure.

The phase discussed in this study has been observed in our studies of a variety of silicon materials, including multicrystalline float zone (mc-FZ) silicon, Czochralski grown silicon, and as-grown commercial multicrystalline silicon from cast processes. For the purpose of detailed study of this new phase, we used a mc-FZ silicon [30] sample which was contaminated with Ni, Fe and Cu by scratching with a wire of the respective element and then annealed at 1200°C for 2.5 hours, leading to contamination levels of $1x10^{16}cm^{-3}$ for iron, $1x10^{18}cm^{-3}$ for copper and $7x10^{17}cm^{-3}$ for nickel according the maximum solubility of these elements at the given temperature [31]. The sample was "slow cooled" from 1200°C in the furnace.

μ-XRF maps of many different slow-cooled mc-Si samples as well as the mc-FZ material frequently revealed metal-rich precipitates simultaneously containing Ni, Fe and Cu (Figure E15.1). μ-XRF analyses on several multi-metal precipitates consistently yielded a Ni:Fe:Cu ratio of approximately 10:~1:3 with a uncertainty of about 3-5%. To study the chemical nature of these clusters, μ-EXAFS measurements were performed at the K-edges of Ni, Fe and Cu. Because each compound has a unique EXAFS spectrum, a good correlation between μ-EXAFS spectra from the precipitates in silicon and reference materials, which are well characterized in structure and composition, yields a positive identification of chemical state.

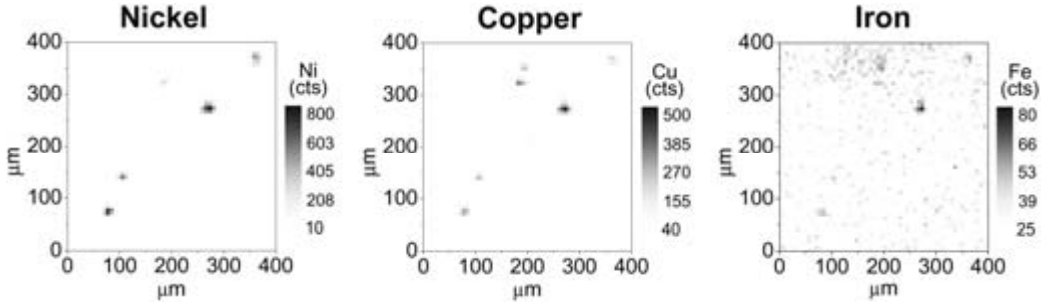

Figure E15.1: X-ray fluorescence microscopy maps of multicrystalline float-zone silicon showing precipitates simultaneously containing Ni, Fe and Cu as dark spots.

To get an idea which phases could have formed, a Ni-Fe-Cu silicide sample was synthesized using an initial stoichiometry following the overall Ni:Fe:Cu ratio from μ-XRF measurements on the precipitates, and a transition metal to silicon ratio of 1:2, which corresponds to the most Si-rich phase of the Metal-Si system (i.e. MSi_2). According to this initial ratio, high-purity powders (99.999%) of the elements silicon, iron, nickel and copper were mixed and homogenized by melting in a SiO_2 crucible at 1600°C. The resulting melting ball was placed

in an evacuated silica ampoule and annealed at T=1000 °C for seven days and then quenched in water.

The synthesis product was checked by an XRD measurement on a Seifert XRD3000 diffractometer. It was confirmed that the resulting material was a mixture of silicon, two phases structurally similar to $NiSi_2$ (referring to the Joint Committee for Powder Diffraction Studies, JCPDS, standard number 43-0989), and smaller amounts of another phase similar to $Cu_3Ni_{10}Si_7$ (JCPDS 03-1061).

The chemical composition of the reference sample was then determined by electron microprobe analysis using a CAMECA SX100 operating at 15kV/20nA and using calibration standards of synthetic NiO, $CuFeS_2$ and $CaMgSi_2O_6$. It was found that the composition of the main phase in the reference sample is $Ni_{0.83(1)}Fe_{0.20(1)}Cu_{0.03(1)}Si_{1.97(1)}$. The secondary phases, $Ni_{1.01(1)}Cu_{0.13(1)}Si_{1.84(1)}$ and $Cu_{0.39(1)}Ni_{0.24(1)}Si_{0.36(1)}$, did not contain iron and were therefore not of interest for a phase identification of the mc-FZ precipitates.

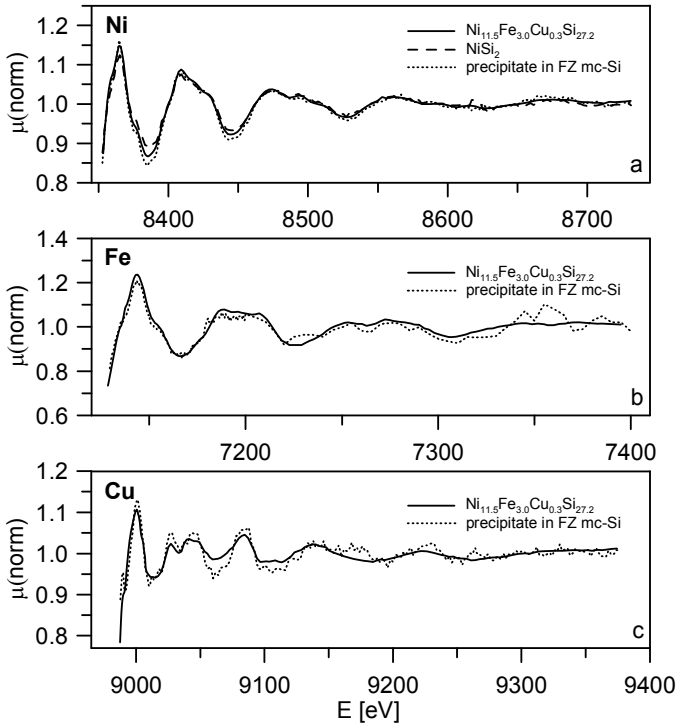

Figure E15.2: EXAFS spectra of each transition-metal edge of precipitates in multicrystalline float-zone silicon and the synthetic reference material, $Ni_{0.82}Fe_{0.21}Cu_{0.02}Si_{1.94}$. Good match between all EXAFS spectra indicates the same atomic site occupancies in both phases. The Ni EXAFS (a) matches as well with pure $NiSi_2$, which supports that the investigated phases have a CaF_2-type $NiSi_2$ structure.

To obtain a homogeneous reference material, in a second synthesis a powder mix was produced with an initial weight according to $Ni_{0.83}Fe_{0.20}Cu_{0.03}Si_{1.97}$, pressed to a pellet and annealed in an evacuated silica ampoule at 900°C for two days. The product was homogenized by grinding in an agate mortar, pressed again and annealed a second time under the same conditions. The XRD measurement on the resulting material confirmed a single phase similar to

$NiSi_2$ (JCPDS 43-0989) with a composition of $Ni_{0.82(1)}Fe_{0.21(1)}Cu_{0.02(1)}Si_{1.94(1)}$ which was determined by electron microprobe analysis.

The comparison of the Ni EXAFS spectra of a) the precipitates in the slow cooled mc-FZ-silicon, b) pure $NiSi_2$, and c) the synthesized reference material confirmed that all these compounds have nickel in the same coordination as the CaF_2-type $NiSi_2$ structure (Figure E15.2a). The very good match between the EXAFS spectra of the mc-FZ precipitates and the standard exists for every measured element, indicating the same atomic site occupancies in both phases (Figure E15.2a-c). Thus, it is obvious that their individual structures just differ in elemental substitutions on the atomic sites of the same structure type.

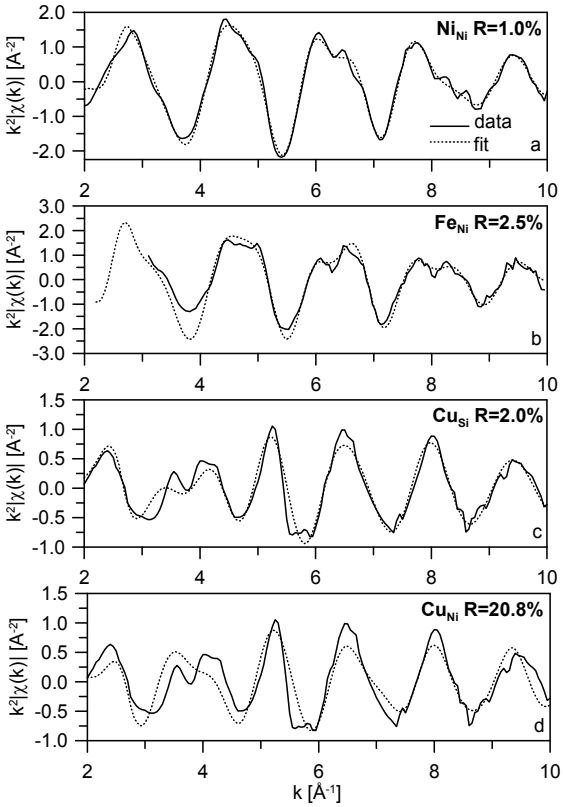

Figure E15.3: EXAFS data and fits for each transition-metal edge: (a) Ni on the nickel site in $NiSi_2$, (b) Fe on the nickel site in $NiSi_2$, (c) Cu on the silicon site in $NiSi_2$, (d) Cu on the nickel site in $NiSi_2$.

Further, the measured compositions $Ni_{0.83}Fe_{0.20}Cu_{0.03}Si_{1.97}$, $Ni_{1.01}Cu_{0.13}Si_{1.84}$ and $Ni_{0.82}Fe_{0.21}Cu_{0.02}Si_{1.94}$ imply that Ni and Fe share one site of the structure, and Cu and Si the other site, since the summation of the formula units gives: 2[Ni,Fe]=[Si,Cu].

It was possible to confirm this assumption by analyzing the EXAFS data measured for Ni, Fe and Cu at the precipitates as well as for the reference material. Note that the oscillations in the Ni and Fe spectra are very similar, which suggests that both elements are in a similar structural environment, i.e. sharing the same site of the structure. In contrast, the oscillations in

the Cu spectrum appear very different from the Ni and Fe spectra, implying that Cu has a different structural environment and occupies a different structural site.

Following these considerations, a structure model was developed to analyze the EXAFS data of the reference material. This model is a derivative of the fluorite – type structure of $NiSi_2$ (spgr. $Fm\bar{3}m$), whereby 20% iron and 80% nickel share the Ni-site (4a) and 99% silicon and 1% copper share the Si-site (8c). The cubic lattice parameter a=5.3957(2)Å was determined from the XRD of the reference material using silicon as internal standard to correct the Bragg angles.

A well established procedure to analyze EXAFS data is by modifying an *ab initio* calculated theoretical standard [32]. Hereby a sum over multiple scattering calculations is used to predict an EXAFS signal from a structure model and the differences between the calculated and the measured EXAFS signal are minimized using least squares algorithms to find the best-fit set of parameters for the calculated signal. Based on the above mentioned structure model, individual theoretical standards for each elemental EXAFS spectrum (Ni, Fe, Cu) were calculated using the computer program FEFF8 [33]. Since the proposed structure contains mixed occupancies, which cannot be simulated directly with FEFF8, the final scattering contributions were calculated by a weighted averaging of different boundary situations. For example, the scattering path data for the Cu spectrum were generated by averaging FEFF8 calculations for Cu on a Si-site in pure $NiSi_2$, Cu on a Si-site in a hypothetical "$FeSi_2$" structure and Cu on a Cu-site in hypothetical "$NiCu_2$" structure (both identical to $NiSi_2$). Hereby the weighting scheme referred to the measured composition of $Ni_{0.82}Fe_{0.21}Cu_{0.02}Si_{1.94}$.

The refinements were performed with the program IFEFFIT [34] using 8-10 free parameters. Further details can be found in the July 2006 quarterly technical status report. The refinements achieved good fits for every measured spectrum ending up in R-values between 1 and 2.5%. To visualize the results figures E15.3a-c show the EXAFS data and fits for each transition-metal edge, and Figs. E15.4a-c show the real parts of the Fourier transform of these data. The refined local distortions as well as the good fit support the assumption that copper shares a site with silicon in the $Ni_{0.82}Fe_{0.21}Cu_{0.02}Si_{1.94}$- structure.

Attempts were also made to refine structure models with Cu on an interstitial site or sharing the site with Ni and Fe, but it was not possible to refine these models with resulting R-values under 10% (see Figs.E15.3d, E15.4d), which again suggests that Cu occupies the Si site in this compound.

In summary, experimental evidence of the formation of a so far unknown mixed silicide phase with a fluorite-type structure in silicon samples is presented. The analysis of the precipitates was possible using synchrotron based μ-EXAFS measurements. Simulation of EXAFS spectra taken on K-edges of the transition metals combined with analysis of standards synthesized for this study reveal that the silicide phase has a structure similar to $NiSi_2$ but with mixed occupancies of the Ni- and the Si- sites. Thus, nickel and iron share the (4a)-site of the structure, which is reported for various structures because of the similar properties of these elements. On the other hand, copper shares the (8c) site with silicon, which is more rare but is physically and chemically feasible. Similarities in the bonding behavior of Cu and Si are theoretically predicted [35], and the shared site occupancy of these elements within intermetallic compounds like Cu_3Si has been reported [36]. Hereby the variability in composition of the precipitates and the reference material indicates that the investigated structure can act as host for different transition metals.

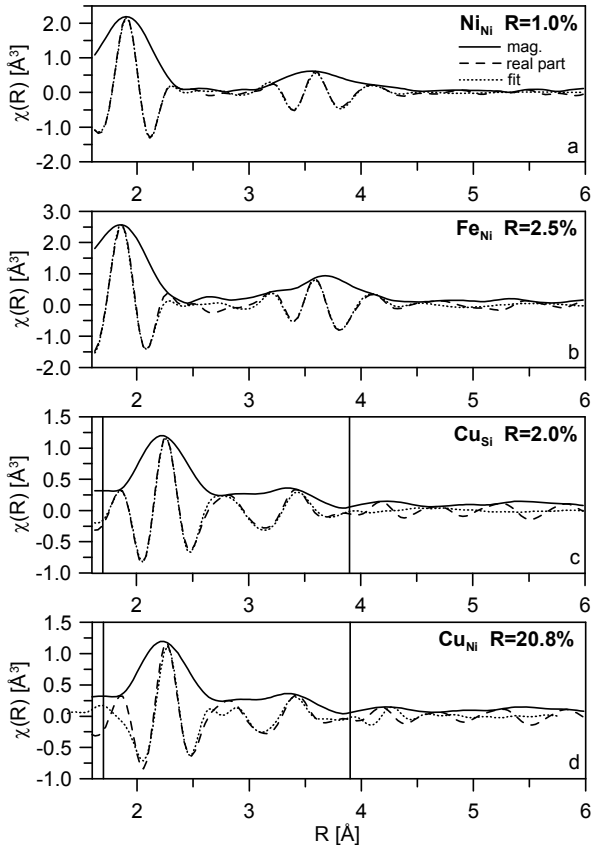

Figure E15.4: Magnitude (mag.) and real part, of Fourier transform of EXAFS data and fits for each transition-metal edge: (a) Ni on the nickel site in $NiSi_2$, (b) Fe on the nickel site in $NiSi_2$, (c) Cu on the silicon site in $NiSi_2$, (d) Cu on the nickel site in $NiSi_2$. Note, the fitting range in (c) and (d) is between the vertical lines.

E.16. Establish correlations between feedstock quality, crystal growth parameters, spatial distribution, and chemical state of metals in multicrystalline silicon *(task 5.3)*

As newer multicrystalline silicon materials evolved, it has become clear that in order to fully assess the effect of metals on solar cell performance, one must take into account feedstock quality, crystal growth parameters, and link these factors to the spatial and size distributions of metal-related defects, their chemical natures, and their interactions with different types of defects. We employed synchrotron-based analytical techniques to determine the aforementioned characteristics of metal contamination in a variety of mc-Si materials from multiple vendors and to correlate distribution and state of metals in solar cells with the growth conditions of the material and the source of contamination. The conclusions drawn in this study are based on a large database of experimental data, which is much wider than a few typical metal distribution maps included in this report by way of example.

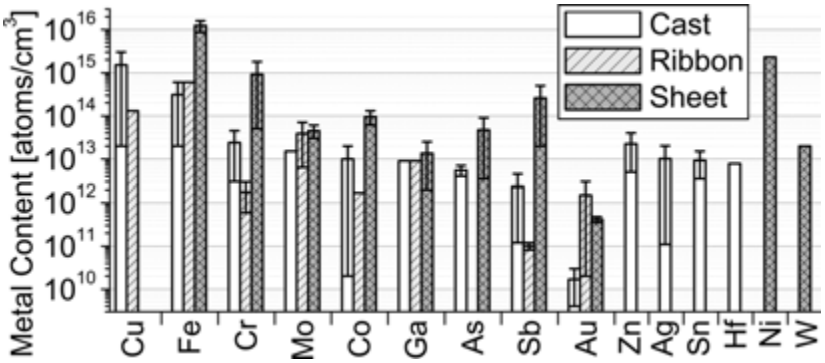

Figure E16.1: Neutron activation analysis data of total metal content in ingot-grown, ribbon, and sheet mc-Si materials, as determined from our and literature data (Refs. [22, 26, 28]). Note that the total metal content is a strong function of feedstock quality, which can be varied between growth runs. Additionally, since data was compiled from three different studies, sensitivity limits for one element may vary between materials. Thus "zero" values do not indicate the absence of that metal in a particular material, simply a signal below the detection limit.

We have examined and compared ingot-grown mc-Si material from three manufacturers, which will be distinguished as "material A", "material B", and "material C". Since variations in impurity distributions are known to exist along the height, i.e., along the growth direction, of the ingot, samples from material A were extracted from three locations along the growth direction (bottom, middle, and top) of several ingots subject to different growth conditions, as well as near the edge of the ingot. Samples from the bottom of the ingot were analyzed for material B, as well as samples from near the top of the ingot from material C. In addition, two types of ribbon materials and two types of Astropower SiliconFilm™ material were analyzed, one using high-purity feedstock (Sheet A) and another using low-purity feedstock (Sheet B). Finally, multicrystalline float zone (mc-FZ) samples grown from melts intentionally doped with copper, iron, and titanium were also analyzed. While not commercial solar cell material, mc-FZ allows one to study the distribution, chemical nature, and effect on diffusion length of one impurity species at a time, making it a powerful research tool.

The most characteristic observations for each type of material are shown in Table E16.I, and can be summarized as follows (further details are provided in the subsequent sections):

Directionally-solidified ingot-grown material: Nanoprecipitates (diameter ≤ 200 nm), typically consisting of silicides of faster-diffusing metal species (e.g., Cu, Ni, Co, and/or Fe), are detected along certain grain boundaries (Figure E16.2), and are sometimes elongated along the grain boundary directions (Figure E16.3, particle #5). Such precipitates are predominantly found in the bottom, top, and side (edge) regions of the ingot, and less frequently in the middle. Near the top of the ingot, smaller, more homogeneously distributed precipitates are observed.

Metal particles several microns in diameter, typically in oxidized chemical state, are found in much lower but variable spatial densities. These particles are frequently found within the grains and towards the edges of the ingot, and occasionally at grain boundaries (Figure E16.2). Their compositions can vary substantially (see Figure E16.3) but often include Fe and Ti, less frequently other elements such as Ca, Cr, Mn, Mo, and Zn, and sometimes additions of faster diffusers (Cu, Ni, and Co).

Ribbon Material: Multicrystalline silicon ribbon materials vertically grown by non-substrate-assisted methods were analyzed on beamlines of medium sensitivity (ALS 10.3.1 and 10.3.2). While these beamlines could detect metal-rich particles in most other as-grown mc-Si materials, no metal-rich particles were detected in the ribbon materials analyzed in this study, despite total metal contents comparable to ingot-grown mc-Si. This suggests that metals in these ribbon materials are distributed more homogeneously and in smaller particles and point defects, below the detection limits of those beamlines.

Sheet Material: Sheet materials horizontally grown by substrate-assisted methods were analyzed using high- (APS 2-ID-D and 20-ID-B) and medium-sensitivity (ALS 10.3.1 and 10.3.2) beamlines. In sheet material grown with high-purity feedstock (sheet material A), no metal-rich particles were detected in as-grown material, in agreement with the results from ribbon materials. As-grown material subjected to a post-growth anneal at high temperature, which allows existing precipitates to grow by absorbing metals in solution within the crystal, exhibited iron and copper particles along structural defects.

Within the grains and occasionally at grain boundaries in sheet material grown from low-purity feedstock (sheet material B), one observes a low density of clusters, tens of microns across, containing micron-sized particles consisting of iron silicide, nickel silicide, and chromium silicide. Rarely, oxidized particles up to 25 μm diameter can be observed. In as-grown material subject to a 800°C anneal for 4 hours, iron silicide nanoprecipitates can be observed in high densities along grain boundaries and intragranular defects, believed to be voids [37] or another type of microdefect. Were all the iron silicide precipitated at grain boundaries and at intragranular defects to be dissolved homogeneously throughout the sample, estimates indicate that bulk concentrations up to 10^{15} Fe/cm^3 could be reached [20].

Mc-FZ doped with Copper: Mc-FZ containing (3-4)×10^{16} cm^{-3} Cu (arising by intentional melt doping during growth) demonstrate large, recombination-active Cu_3Si particles (or clusters of particles) along structural defects such as grain boundaries and dislocations (Figure E16.4a). The distribution of copper at structural defects is inhomogeneous, in agreement with previous studies [38-40], such that the spaces between precipitates exhibit noticeably lower recombination activity.

Mc-FZ doped with iron: In mc-FZ containing approximately 10^{16} cm^{-3} Fe (by intentional melt doping during growth) a few micron-sized iron silicide particles are detected in low spatial densities (e.g., Figure E16.4b). While these Fe silicide particles coincide with a

locally-decreased XBIC, the predominant features observed in XBIC maps are highly recombination-active grain boundaries and intragranular regions. These are present to a much lesser extent in undoped reference mc-FZ material, indicating that a high density of nm-sized defects (precipitates and metal point defects) are present with dimensions below the detection limits of the experimental conditions used in this study. The large $FeSi_2$ particles observed in the µ-XRF scans are probably incorporated into the material as inclusions directly from high iron concentrations in the boundary layer of the interface melt.

Mc-FZ doped with Titanium: Mc-FZ containing 5×10^{13} cm^{-3} Ti (by intentional melt doping during growth) exhibited no Ti-rich particles above the µ-XRF detection limits chosen for this study (Figure E16.4c, noise only is visible). Nevertheless, structural defects and intragranular regions demonstrated exceptionally high recombination activities, suggesting a fine distribution of metal atoms or particles below the detection limits of the experimental conditions used in this study. Impurity segregation to structural defects during crystal growth, which may be responsible for the recombination activity of structural defects in this sample, will be discussed below.

Table E16.I. Summary of observed particles in mc-Si materials. Not included in this table are metals homogeneously distributed along structural defects and metal point defects, most of which are below the detection limits of µ-XRF.

Defect / Material	*Metal Silicide Nanoprecipitates*	*Metal-rich Inclusions and Microdefects*
Directionally-solidified, ingot-grown mc-Si	*Predominantly found near bottom, top, and edges of ingot along structural defects. µ-XRF at nanoprecipitates reveals Cu, Ni, Co, and/or Fe. Compared to other mc-Si materials, the slow cooling rate results in comparatively large (dia. > 30 nm) precipitates in comparatively low spatial densities along certain types of grain boundaries.*	*Predominantly found near bottom, top, and edges of ingot. µ-XRF at inclusions observes Ca, Cr, Fe, Mn, Mo, Ti, Zn, and/or traces of fast diffusers (Cu, Ni, Co). Microdefects can contain C, N, Fe, Cu, Ca.*
Ribbon Material (vertically-grown, without substrate)	*Generally below detection limits of medium-sensitivity µ-XRF beamlines. Comparatively fast cooling rate likely responsible for smaller precipitates in higher spatial densities.*	*Unstable growth from melts with high impurity contents can result in a variety of inclusions and microdefects. None observed in high-purity materials analyzed in this study.*
Sheet Material (horizontal substrate-assisted growth)	*Predominantly found along structural defects. µ-XRF detects Cu and Fe. Fast cool likely responsible for high spatial densities of small precipitates, sometimes below detection limit in samples with low impurity content.*	*µ-XRF detects intragranular inclusions in material with high impurity content, including Fe, Cr, Ni. Microdefects can contain C, O.*

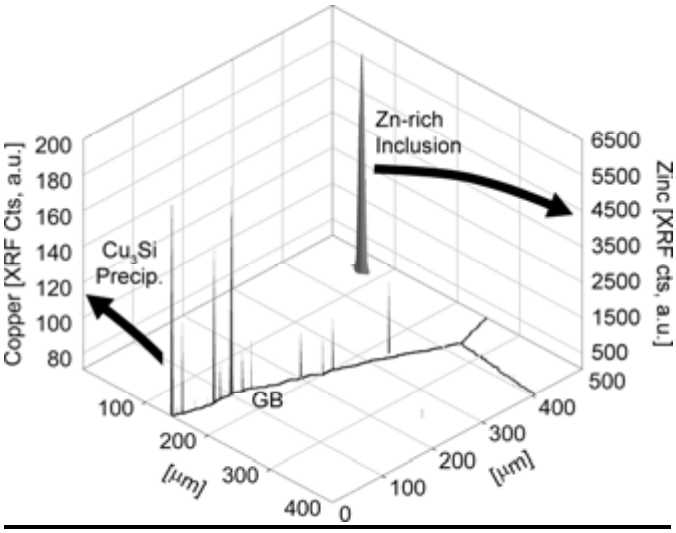

Figure E16.2: μ-XRF maps of Cu and Zn distributions in ingot-grown mc-Si, exemplifying the two types of metal-rich particle commonly observed in mc-Si: metal silicide nanoprecipitates (along a grain boundary, denoted by thick line and “GB”) and spatially-isolated inclusions up to several microns in diameter.

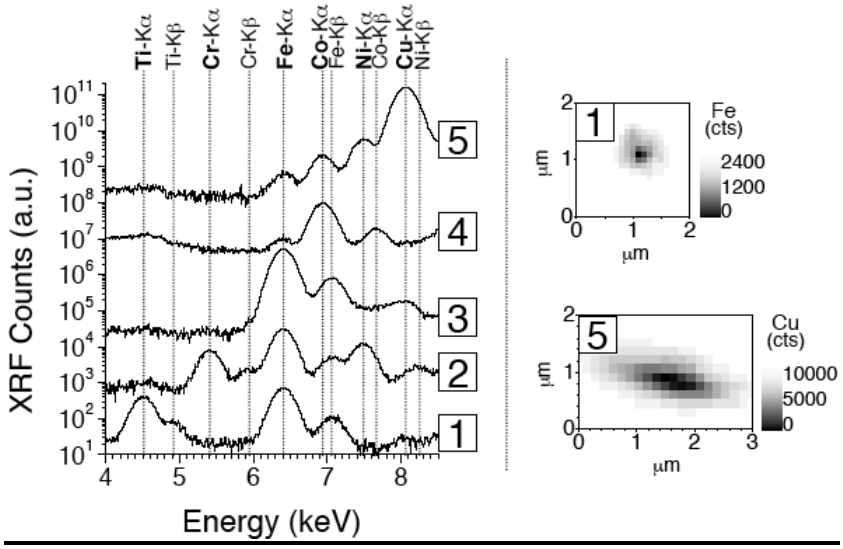

Figure E16.3: μ-XRF point spectra on impurity-rich particles in ingot-grown mc-Si material reveal a wide range of compositions and suggest a diversity of contamination sources. Two-dimensional μ-XRF maps reveal that particles of slower-diffusing species (e.g. "1", top right) are often found within the grains, while particles of faster-diffusing species (e.g. "5", bottom right) are often found at grain boundaries, sometimes elongated along the grain boundary direction.

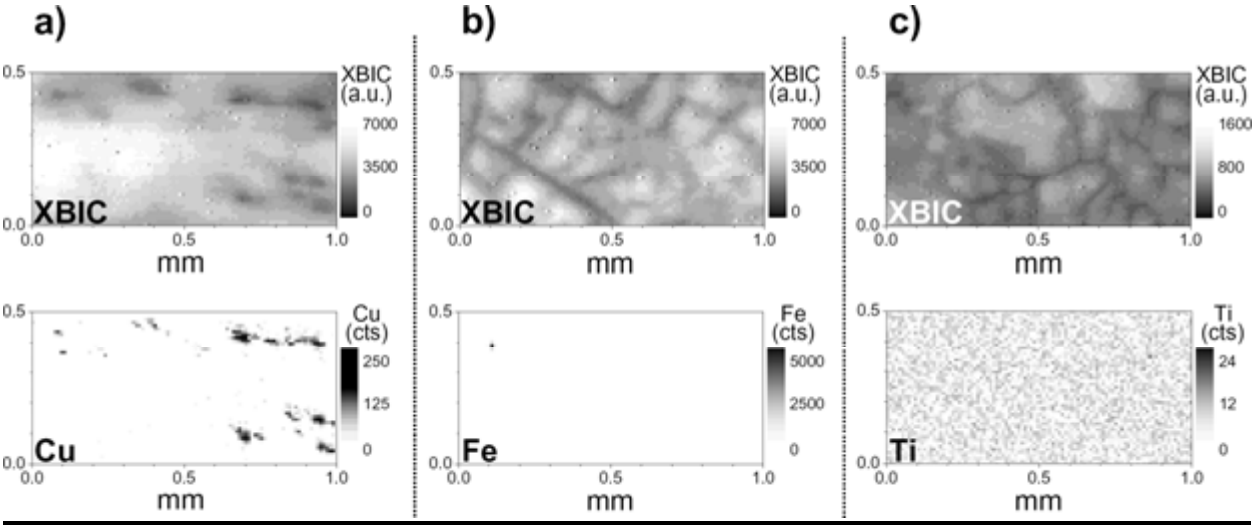

Figure E16.4: XBIC (above) and μ-XRF (below) maps of multicrystalline float zone silicon grown from metal-doped melts of (a) copper, (b) iron, and (c) titanium. Whereas high-flux Cu tends to form relatively isolated metal-rich particles or clusters of particles, low-flux Ti and Fe tend to form metal point defects and homogeneously coat structural defects (as evident in XBIC), often below the current detection limits of the μ-XRF technique. Occasionally, large inclusions can be detected (e.g., Fe).

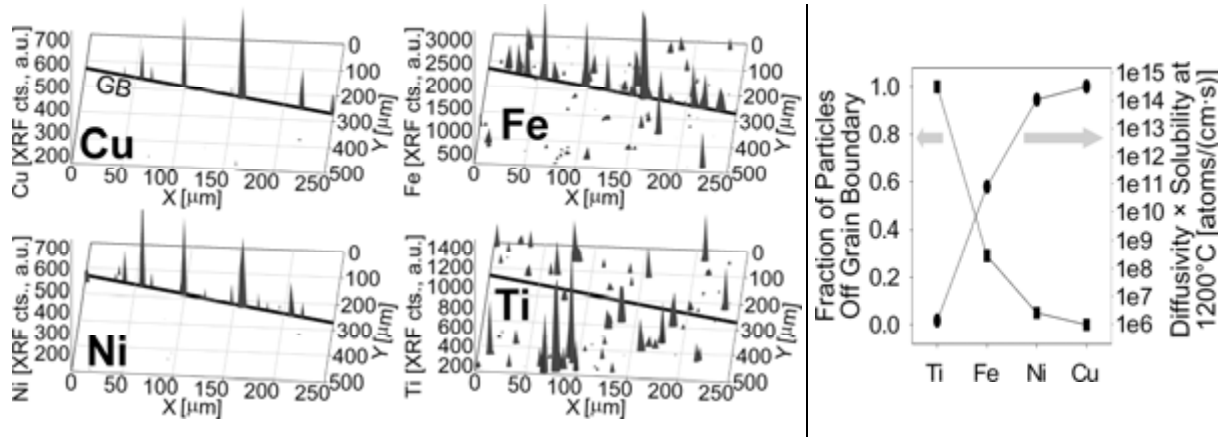

Figure E16.5: Dependence of elemental distribution in ingot-grown mc-Si on diffusivity and solubility. The four μ-XRF maps to the left depict a grain boundary (thick line denoted by "GB") in material extracted from near the edge of an ingot, and surrounding intragranular regions. Particles of low-flux species (e.g. Ti) are often found within the grains, while particles of high-flux species (e.g. Cu, Ni) are often found aggregated in a fewer total number of particles, usually at grain boundaries.

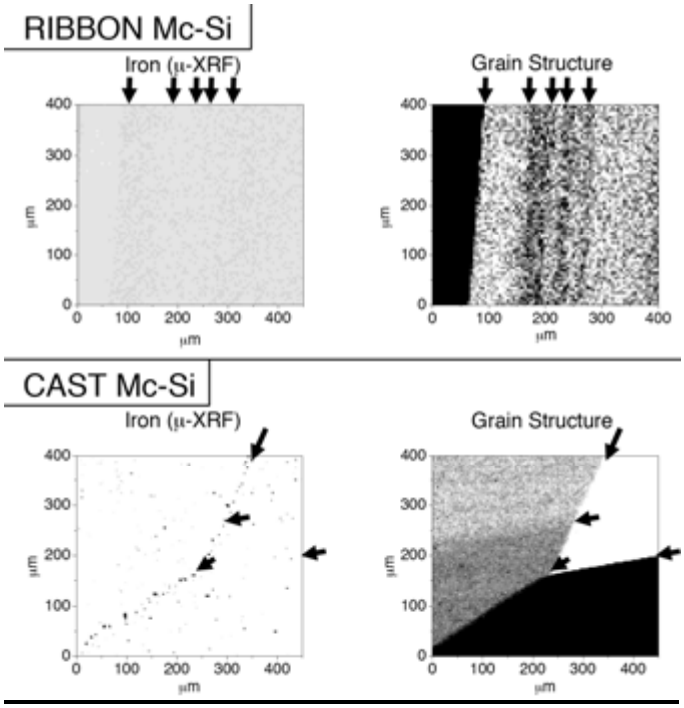

Figure E16.6: μ-XRF maps of iron distributions in ribbon and directionally-solidified mc-Si, using the elastically scattered X-ray beam peak intensity to determine grain structure. Metal silicide nanoprecipitates are detected along certain structural defects in the ingot-grown mc-Si, whereas in ribbon materials, no metal-rich particles are detected. This difference can stem from two possible (non-exclusive) phenomena: (a) the faster cooling rate of ribbon mc-Si and a low metal concentration favor the formation of smaller precipitates below the current detection limits of μ-XRF, and (b) the structural defects in ribbon (especially twin boundaries) have less capacity for metals than the high-angle twin and random grain boundaries of ingot-grown mc-Si and sheet materials.

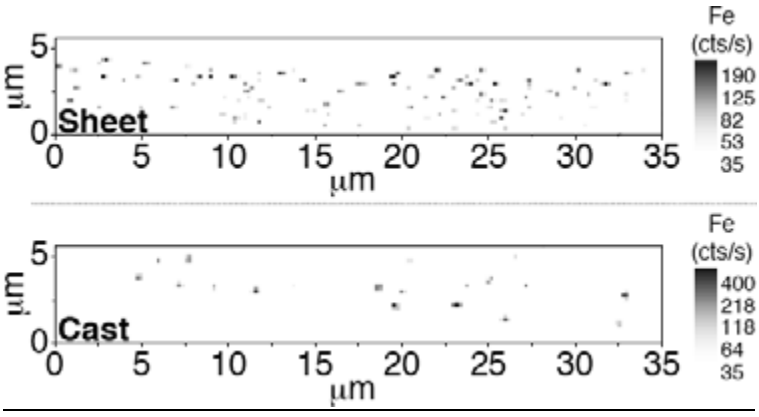

Figure E16.7: Comparison of size and spatial distribution of iron silicide nanoprecipitates in grain boundaries of sheet mc-Si grown with the aid of a substrate (above) and ingot-grown mc-Si (below) from near the bottom of the ingot. A lower density of larger (note the Fe count rate, right) nanoprecipitates is detected by μ-XRF in the ingot-grown mc-Si sample, likely a reflection of the slower cooling rate of ingot-grown mc-Si.

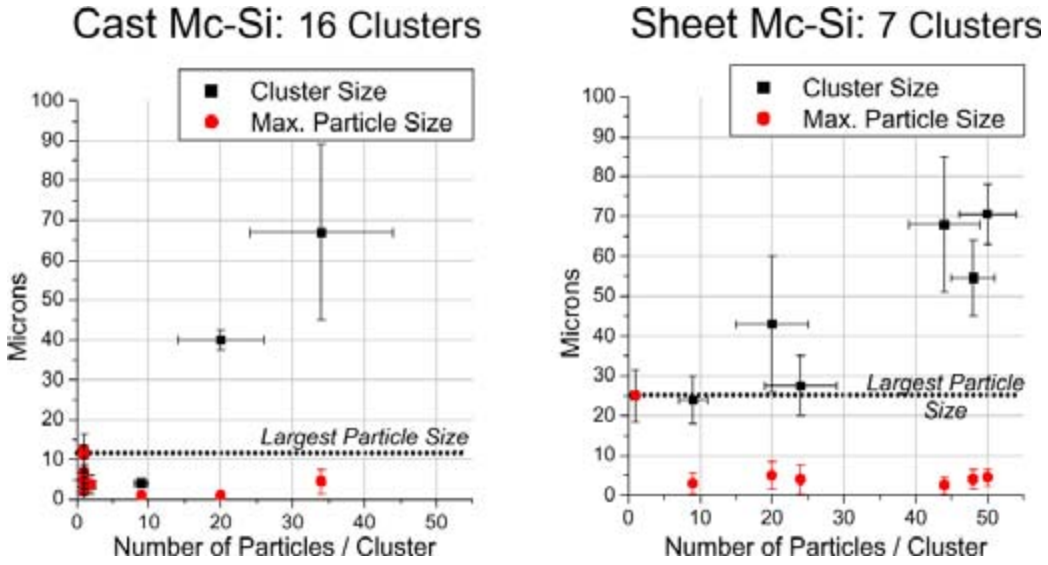

Figure E16.8: Size distributions of inclusion clusters and of the individual particles composing the clusters, detected by μ-XRF in ingot-grown (16 inclusion clusters analyzed) and sheet (7 clusters analyzed) mc-Si materials. Inclusions are often observed in regions of unstable crystal growth (e.g. near growth surfaces, and within the first and last regions of the crystal to solidify). Ingot-grown mc-Si has a predominance of single particle inclusions with comparably smaller maximum size, with the exception of two large inclusion clusters observed near the edge and bottom of an ingot. In sheet mc-Si, large clusters of particles are frequently observed, especially towards the backside (i.e. the last to solidify) of the material, as well as a comparatively large single particle. The different size distributions of clusters in the two materials are believed to stem from differences in crystal growth, such as the solidification velocity and feedstock quality.

SIMILARITIES OF METAL CONTAMINATION BETWEEN MC-SI MATERIALS

The metal-rich particles in all materials analyzed herein can be divided into two distinct classes: (a) the metal silicide (e.g., $FeSi_2$, $NiSi_2$, Cu_3Si, etc.) nanoprecipitate, typically up to several tens of nanometers in diameter, most often associated with structural defects, and (b) the occasional larger particle, up to several microns in diameter, which is frequently oxidized, found within the grains, and/or composed of multiple slowly-diffusing metal species reminiscent of foreign material inclusions (e.g., coming from stainless steels, furnace material, etc.). These two distinct classes of metal-rich particle are shown in Figure E16.2, which portrays a representative μ-XRF map of an ingot-grown mc-Si sample from near the top of an ingot.

Metal-rich particles over 1 μm in size, especially those containing oxidized and/or slowly-diffusing species, are believed to be incorporated directly from the melt during crystal growth. Examples include the 12 μm diameter ZnS particle in Figure E16.2, and the oxidized iron particles previously reported by McHugo *et al*. [2, 8]. Most oxidized metal compounds are not expected to form under equilibrium conditions within silicon [20], and several of these particles are too large to be explained by the precipitation of supersaturated impurities during cooling. These facts, plus the compositions of these particles, indicate that these are inclusions, i.e., incompletely-dissolved foreign particles introduced into the melt and engulfed by the advancing solidification front during crystallization.

In almost all materials analyzed in this study, metal silicide precipitates were detected at structural defects, especially two-dimensional defect surfaces such as grain boundaries and voids.

The appearance of metal-rich particles at structural defects is likely due to a combination of processes. Firstly, impurity atoms in solution (i.e. dissolved) in the crystal at high temperatures supersaturate upon cooling, and then seek the most energetically favorable sites for second-phase (e.g. metal silicide) precipitate nucleation. Secondly, impurity atoms such as iron and copper have been observed to segregate to structural defects even at elevated temperatures; upon cooling, these metals will form precipitates when they reach a supersaturated state. Thirdly, if metals are present in locally high concentrations in the melt, they can precipitate directly from the melt at structural defects that perturb the solidification front, e.g. grain boundaries, when a locally high metal content exists at the liquid solid interface [13, 41]. Such perturbations of the solidification front are also believed to favor the incorporation of foreign particles (e.g. oxidized Ti or Fe) in the melt as inclusions. The end result of all these processes is the accumulation of metals at structural defects in mc-Si.

The capacity of a given type of structural defect to absorb transition metals is a parameter that is known to vary in a somewhat predictable manner [4, 42-44]. Since different mc-Si materials tend to have unique sets of structural defect types, one may expect variations in the amount of transition metal precipitation at structural defects from one material to another. This point is further discussed below.

Some elements tend to aggregate in nanoprecipitates along grain boundaries, while others are found predominantly in large intragranular particles, as evident in Figure E16.5. This divergence can be partially explained by element-specific fluxes and degrees of supersaturation in the material. The product of the solubility [atoms/cm^3] and diffusivity [cm^2/s] of an elemental species at a temperature T yields its *atomic flux* [$\frac{\text{atoms}}{\text{cm}^3 \cdot \text{s}} \cdot \text{cm}^2$], which describes impurity transport within the crystal. Once the total concentration of a given impurity species exceeds its solubility at a given temperature, a driving force for precipitation develops, and the atomic flux determines the distance a certain fraction of impurity atoms can travel before precipitating or forming point defects. In addition, differences in elemental impurity distributions are partly explained by the way different elements are present in the melt and introduced into the crystal (atomically dissolved metals vs. foreign particles of Ti- or Fe-oxide containing many millions of atoms).

Elements with higher atomic fluxes (e.g. Cu and Ni) are predominantly found in silicide nanoprecipitates (10's or 100's of nm in diameter) at grain boundaries or other structural defects, as shown in Figure E16.5. Their more gradual temperature dependences of solubility combined with high diffusivity allow them to diffuse to the most stable sinks (e.g. grain boundaries), where nucleation barriers are lower for precipitation. Precipitates of these elements are typically the easiest to detect by μ-XRF, reflecting both their higher solubilities as well as their tendency to be concentrated at select locations with relatively large distances between particles. This reduces the concentration of dissolved metals and smaller precipitates elsewhere and improves material performance between particles (e.g. Figure E16.4a).

Elements with medium (e.g. Fe) or low (e.g. Ti) atomic fluxes are more frequently found in intragranular defect particles, as Figs. E16.2 and E16.5 demonstrate. These atoms are less likely to dissolve from inclusions formed during crystal growth, and thus are less likely to diffuse to structural defects and form precipitates. On the other hand, metals in solution with low atomic fluxes cannot diffuse very far during cooling and tend to precipitate locally upon supersaturating, forming precipitates that are much smaller and closer-spaced than those of metals with higher atomic fluxes, as deduced from Figs. E16.4b and E16.4c. Unfortunately, point defects of these

low-flux species are known to form deep levels in the silicon bandgap [45, 46]. Thus, it is not surprising that elements of lower atomic fluxes tend to be more harmful for solar cell device performance [42, 45, 47], since these elements form closer-spaced and more recombination-active defect centers.

Elemental distributions in the solidified mc-Si material also depend on the way elements are introduced into the crystal. μ-XRF and μ-XAS measurements show Fe and Ti often contained in oxidized particles containing up to 10^8–10^{15} atoms, which are likely inclusions of foreign particles. These compounds have high melting temperatures ($T_M[Fe_2O_3]$=1565°C; $T_M[TiO_x]$>1700°C) and will likely survive for a limited time in the silicon melt, especially if the melt already contains high concentrations of the dissolved impurity. Once incorporated into the crystal, the low fluxes of these metals and high binding energy to oxidized compounds hinders metal dissolution from inclusions into the grains. On the other hand, copper oxides have melting temperatures below that of silicon, so these particles likely dissolve in the melt prior to their incorporation into the mc-Si crystal, facilitating silicide precipitate formation during cool-down.

DIFFERENCES IN METAL CONTAMINATION BETWEEN MC-SI MATERIALS

Impurities may enter the mc-Si crystal from any non-silicon object, whether from feedstock or crystal growth, which is directly or indirectly in contact with the melt or cooling crystal. Impurities observed in mc-Si reflect a wide variety of different contamination sources, as shown in Figure E16.3. One contamination source is stainless steel, likely originating from furnace parts, growth surfaces, or feedstock. The possibility of contamination from materials coating growth furnaces was demonstrated in the January 2006 quarterly technical report. Impurity concentrations may vary from run to run in the same process equipment, or even from one region to another in the same crystal, e.g. along the height of an ingot or between different ingots.

Because different types and concentrations of metal impurities have varying effects on minority diffusion length [48], control over all process parameters and impurity sources (feedstock, growth surfaces, furnace parts, etc.) is necessary to ensure the production of mc-Si material of consistently reproducible quality.

A number of studies [42, 43, 49] indicate that each type of structural defect has its own capacity for transition metals, which affects the ability for the segregated metals to aggregate at the defect and eventually form precipitates during crystal cool-down. Evidence for this is shown in Figure E16.6, which compares grain boundary decoration in ribbon and in ingot-grown mc-Si samples. The grain boundary locations were determined by the intensity of the elastically scattered X-ray beam in the direction of the detector (a function of grain orientation). In the ingot-grown mc-Si sample, metal silicide precipitates are detected at some grain boundaries but not at others, while no metal-rich particles are detected in ribbon. While differences in grain boundary metal decoration between ingot and ribbon materials are also influenced by other factors (namely crystal cooling rates), local differences within the same material can be explained only by differences in structural defect character and density.

The crystal growth conditions play a large role in determining the densities and types of structural defects within the crystal [50-52], i.e., the density of precipitation sites for impurities. Large-angle and random grain boundaries common to sheet and ingot-grown mc-Si are the easiest for precipitate nucleation, given model defect studies [42, 43]. This is supported by the greater abundance of metal nanoprecipitates detected by μ-XRF at these defect types (e.g. Figure

E16.6). Such structural defects with large capacities for impurities will also act as internal gettering sites, reducing the metal point defect concentration and increasing the minority carrier diffusion length within the grains. On the other hand, $\sum 3<111>$ twin boundaries common to both ingot-grown mc-Si and ribbon [53, 54] offer less segregation and nucleation sites for metals. Metal precipitates are seldom observed by μ-XRF at those locations in these materials.

Interactions between metals and structural defects can either be advantageous [55, 56] or detrimental [5, 30, 48] for solar cell device performance, depending on the spatial density, location (especially with respect to the pn-junction), and character of structural defects within the device. If one could, during crystal growth, reliably control the types of structural defects and their densities, one would subsequently reduce the variability in the sizes and densities of metal silicide nanoprecipitates. This, in turn, would reduce the variability of the impact of metallic impurities on performance.

In addition to structural defect density discussed above, at least three other crystal growth variables combine to determine the size and spatial distribution of metal silicide nanoprecipitates: (1) the cooling rate during crystal growth, (2) the total metal content, and (3) variations of crystal growth conditions as growth progresses. Since it is necessary to decouple these effects to fully understand them, the next paragraphs describe examples where one or two of the variables are held constant, while a second and/or third is altered.

To study the effect of cooling rate on nanoprecipitate size and spatial distributions, one can select ribbon and ingot-grown mc-Si materials with comparable total metal contents, but orders of magnitude different interface cooling rates (approx. 1000-2000°C/min for ribbon, 20-100°C/min for ingot-grown, according to [53]). While metal silicide precipitates can be detected by μ-XRF along certain grain boundaries in the ingot-grown mc-Si sample, ribbon material exhibits no such precipitates above the detection limits (Figure E16.6). This can be explained by the effect of cooling rate on the spatial and size distributions of metal precipitates. Assuming a fixed initial impurity content, faster cooling rates (>100°C/min.) during crystal growth result in faster impurity supersaturation, which in turn provides a stronger driving force for metals in solution to precipitate locally. Consequently, faster-cooled materials (e.g. ribbon and sheet) contain metal nanoprecipitates with relatively smaller average sizes and higher spatial densities [57]. On the other hand, slow cooling after growth (< 20°C/min.), typical of ingot-grown mc-Si, allows impurity atoms to diffuse over much larger distances and accumulate preferentially at the most energetically favorable sites, resulting in a few large particles separated by larger distances.

The effect of total metal concentration on nanoprecipitate size is seen by comparing materials with dissimilar metal contents, but comparable cooling rates. Sheet material B experiences cooling rates comparable to ribbon materials and sheet material A, but contains one to two orders of magnitude greater metal content. As a consequence, metal silicide nanoprecipitates (~46 nm diameter) are detected along structural defects in sheet material B (Figure E16.7), while no precipitates are above the detection limits in the other sheet and ribbon materials. A higher dissolved metal concentration in sheet material B is likely to provoke supersaturation – and thus the onset of precipitation – at a higher temperature, when the atomic flux of impurities is orders of magnitude larger, allowing impurities to accumulate at stable sinks such as grain boundaries.

Inevitably, variations of crystal growth conditions occur as crystal growth progresses. Hence, different regions of the ingot or in different wafers of ribbon or sheet mc-Si (depending on the time elapsed from the beginning of the growth run [53]) can be expected to have different concentrations and distributions of impurities. Independent studies have demonstrated how the

total metal content [28] and the iron point defect concentration vary as a function of ingot height, largely because of impurity segregation from the solid to the melt, in-diffusion of impurities from growth surfaces, and back-diffusion after solidification. We observe similar trends: near the middle of the ingot, where segregation has reached a steady-state and the dissolved metal concentration and total metal content [28] are lower than near the culmination of growth at the top of the ingot, metal silicide nanoprecipitates are not readily detected. On the other hand, metal silicide nanoprecipitates are readily observed in three locations: (a) near the top of the ingot, due to impurity segregation during growth, (b) near the edges of the ingot, arising from impurity indiffusion from the growth surfaces, and (c) near the bottom of the ingot, arising from the latter effect concomitant with non-steady-state segregation of impurities during the early stages of ingot growth.

We have studied many tens of inclusions during our investigations, which lead us to conclude that inclusion size and distribution can be affected by two crystal growth variables: (a) crystal growth velocity (or "crystal pull velocity"), and (b) stability of the growth process.

Under stable growth conditions, the growth velocity is one of the key parameters that determine the maximum size of second-phase particle incorporated by the advancing solidification front. Slower-moving solidification fronts tend to push large, second-phase particles in the melt forward like a snow-plow, while faster-moving solidification fronts increase the chances of these particles being incorporated as inclusions [58]. Our observations are consistent with this model: the largest single particle inclusion was observed in fast-solidified sheet Material B, as shown by the dotted horizontal line in Figure E16.8. On the other hand, the sizes of single particles in slowly-solidified ingot-grown mc-Si were comparatively smaller. It must be noted that the size and chemical state distributions of impurity-rich particles in the original contamination sources (e.g. growth surfaces, feedstock, growth environment) strongly influence the maximum inclusion size detected in as-grown mc-Si.

The largest and most abundant inclusions in both ingot-grown mc-Si and sheet material B are generally found in first or last regions of the crystal to solidify, or near the growth surfaces. In ingot-grown mc-Si, this corresponds to material near the edges of the crucible, as well as near the bottom and the top of the ingot. Incidentally, these regions are also where the majority of metal silicide precipitates are observed, suggesting that unstable crystal growth [12] and high metal concentrations dissolving from growth surfaces favor the formation of these nanodefects.

The presence of foreign particles in the melt can adversely affect mc-Si material performance. If metals are dissolved from foreign particles, this increases melt impurity levels and leads to a higher level of decoration of structural defects at the interface, also increasing the recombination activity of those defects in the crystal. Foreign metal-rich particles incorporated directly into the material as inclusions affect only a small volume of material around the inclusion, provided these are not formed from a metal species with sufficiently high atomic flux to be liberated during subsequent solar cell device processing [59, 60].

To summarize the findings of this section, most of the differences observed between materials can be attributed to the crystal growth conditions and external contamination sources. Metals detected by μ-XRF can typically be traced back to specific parts of the production process (e.g. feedstock, material lining growth surfaces, etc.). The final distribution and form of metals, which most severely affects device performance, is dictated not only by the nature (i.e. diffusivity and solubility) of the contaminants, but also by a handful of crystal growth parameters: the crystal growth velocity, the total time silicon remains in a molten state, the character and density of structural defects, and most significantly, the cooling rate. Fast-cooled

materials such as ribbon and sheet material tend to have larger densities of smaller precipitates, while more slowly-cooled material such as ingot-grown mc-Si and mc-FZ exhibit a comparatively lower density of larger metal silicide precipitates.

These differences underscore two important points: (1) the critical impurity content for one mc-Si material or processing sequence may not necessarily be the same for all others. Material-specific crystal growth conditions and contamination sources can produce differences in the spatial distribution and chemical nature of metals, which directly affects the minority carrier diffusion length and its response to processing. Thus, one must individually evaluate threshold values for impurity content and nature in the feedstock and production environment for each mc-Si material. (2) A complete material-specific optimization of solar cell device processing must take these differences into consideration.

Our observations on three types of mc-Si materials can be summarized as follows: Multicrystalline silicon ribbon material, because of the rapid cooling during growth which does not allow dissolved impurities to diffuse far before precipitating, the predominance of structural defects with comparatively lower capacity for impurities (e.g. 60° twin boundaries), and the low total transition metal concentration, reveals no metal precipitates above the detection limits of this study. We thus conclude that metals are distributed in a higher density of smaller precipitates and point defects, which could explain the lower performance of as-grown ribbon materials relative to ingot-grown mc-Si. However, effective processing, especially phosphorus diffusion, H-passivation, and aluminum gettering can substantially increase performance.

Sheet material appears to be similar to ribbon, but key differences include feedstock quality and structural defect density and character. In sheet mc-Si grown from feedstock containing high total metal concentrations, material performance can benefit from the proper amount and (three-dimensional) location of random, equiaxial grain boundaries, which serve as nucleation sites for transition metal precipitates, which in turn reduce the metal content within the grains. Metals are also found concentrated in intragranular defects and, due to cleverly chosen growth conditions, segregated towards the back of the wafer (away from the pn junction) during growth. Even with high total impurity contents, these mechanisms contribute to reduce the impacts of metals on device performance. The vast majority of these metals cannot be effectively removed during processing because of their high concentrations, so effective defect engineering of metals within the material is necessary in addition to optimized processing to ensure performance comparable to ingot-grown mc-Si.

Ingot-grown mc-Si in many respects represents the intersection of the two material types discussed above. Metal silicide nanoprecipitates of fast-diffusing species are observed along certain structural defects with high capacities for impurities, but not along others. Those structural defects are effective internal gettering sites for metal point defects during the slow ingot cool, and the concentration of point defects can be reduced considerably. However, one must keep this initial defect distribution in mind when optimizing solar cell processing, as to avoid possible re-dissolution of metals from silicide nanoprecipitates back into the grains. Slower-diffusing impurities are frequently observed at intragranular inclusions, often in an oxidized chemical state and/or present with other metals that indicate the origins of contamination as the feedstock, crucible walls, and/or furnace parts. Although these particles themselves are in too low spatial density to significantly impact diffusion lengths, any metals dissolved from these inclusions during growth or subsequent processing can lead to decreased performance.

E.17. Analysis of impurity concentrations in metallurgical and solar-grade silicon *(task 6.4)*.

The cost of raw silicon is determined by its purity. While metallurgical grade (MG-Si) silicon costs not more than $1 to $1.50 per kilogram, semiconductor grade polysilicon can cost anywhere from $35 to $200 depending on the market conditions. If the photovoltaic industry could use "dirty" silicon with less stringent specifications for purity than electronic grade silicon, a substantial gain in cost and availability could be achieved. As early as 1982, Bathey and Cretella [61] pointed out in their review that the cost of silicon could be reduced by a factor of ten by reducing the purity requirements from <1 ppb (semiconductor grade silicon) to 0.5-100 ppm. Feedstock supplies for the PV industry that have intermediate impurity constraints have been dubbed solar-grade-silicon (SoG-Si), although there is yet no consensus concerning what the ultimate specifications should be.

SoG-Si can be manufactured either by simplification or modifications [62-66] of the standard Siemens process based on distillation of silicon-rich gaseous compounds, or by purification of metallurgical grade silicon to reduce concentrations of P, B, Al, O, C, and transition metals. In general, SoG-Si routes utilize significantly less energy than the standard Siemens process, thus reducing both costs and energy payback times. Some of the purification processes that are most frequently mentioned in the literature include one of the following technologies or their combination:

a) Reduction of silica by carbon. This process uses the same reaction that is used for manufacturing metallurgical-grade silicon in an arc furnace ($SiO_2 + 2C \rightarrow Si + 2CO$). The typical impurity level in MG-Si manufactured through this process is 98-99% and even 95% because the raw materials used in this process contain high impurity levels. It is possible to obtain much higher degree of purity of silicon at a reasonable cost by using either naturally clean, or purified by leaching silica or quartz and carbon black or pelletized activated carbon with higher than average purity in specially-designed arc furnaces with purified electrodes [62, 67-74].

b) Acid leaching. This approach calls for pulverizing MG-Si in powder with 70 μm or less particle size, and then treating this powder with various acids (e.g., aqua regia, hydrochloric acid, hydrofluoric acid) to dissolve metal clusters, which are frequently found in MG-Si at grain boundaries and are exposed during powdering [61]. It is possible to obtain silicon with the purity of 99.9% to 99.97% [75-77]. The disadvantage of this process is that it is not effective in removing impurities dissolved intragranularly in high concentrations, e.g., B and P.

c) Gas blowing through the silicon melt. A purity level of 99.99% can be achieved by blowing gases such as Cl_2, O_2, $SiCl_4$, wet hydrogen, CO_2, or their combinations [78, 79]. These gases react with impurities dissolved in silicon and form volatile compounds which evaporate from the melt. For example, chlorides of many metals and BOH are volatile. This method is effective in removing, e.g., Al, Ca, C, Mg, Fe, B, P, and Ti.

d) Directional solidification. During crystal pulling from the melt (e.g., Czochralski or float zone growth) or directional solidification of the molten silicon (e.g., float zone Si, ingot-grown mc-Si) impurities segregate in the melt [62, 74, 78, 80]. At the end of the growth run, the majority of impurities is found in a thin layer near the top of the directionally-solidified ingot or remains in the crucible. Such purification runs can be used to improve the purity of MC-Si. The efficiency of removal of impurities from silicon depends on their segregation coefficients. In general, metals segregate much more effectively than shallow dopants.

e) “Slagging” or calcium leaching. These approaches are based on mixing silicon with a chemical that has high affinity to undesirable impurities, binds them in a stable compound, and can later be separated from the silicon through deposition on the crucible walls, filtering through the mesh, or acid and solvent leaching. For instance, addition of Ca was successfully used for reduction of Fe, Ti, and P concentrations [81]. Another example is immersion of crushed silicon in a metal with low melting point, such as aluminum, silver, or zinc [82]. Silicon may be completely liquefied by forming a Si-Al eutectic at temperatures well below the melting point of Si (such as 1100°C). During cooling, the solubility of Si in Al decreases and silicon precipitates are formed, which are separated from the molten Al by filtering through a mesh. Si pellets are cleaned from Al by acid leaching.

The list above, which is by no means complete, shows that a variety of technologies for inexpensive and energy-efficient purification of silicon are available. One of the chief obstacles on the road to their wide-scale commercialization is the lack of understanding in the photovoltaic community of what contamination levels are acceptable. To make things more complicated, the critical contamination levels are likely to differ among sheet, ribbon, and directional ingot solidification technologies, and may be affected by small changes in the growth and solar cell processing conditions.

It is instructive to compare typical impurity concentrations in MG-Si, SoG-Si, and standard mc-Si currently used for solar cells. The plot presented in Figure E.17.1 is based on the data from Refs. [26, 28, 61, 63, 83-87]. There is no legend in Figure E.17.1 because the link between the sets of bars in the plot and data sources is not important. We are concerned about the general trends. One can see that the impurity content in MG-Si (top graph in Figure E.17.1) is very high, but the values from different sources rarely vary by more than an order of magnitude. The impurity content in commercial mc-Si (the bottom graph in Figure E.17.1) is two to five orders of magnitude lower than in MG-Si, and some elements such as Ti, Mn, V, Zr, Mn, are below the detection limit of neutron activation analysis. The variation in metal concentration by 1 to 2 orders of magnitude reflects the differences in growth conditions and in the quality of feedstock used by different manufacturers. Finally, the most interesting in this figure is the metal concentration in SoG-Si (the middle graph in Figure E.17.1). These data are based on analyses of materials which went through one or several steps of purification of MG-Si. Two facts are worth noting. First, there is huge (up to three orders of magnitude) variation in reported transition metal content from one purification technology to another. Secondly, the metal content in SoG-Si materials is much higher than in mc-Si currently used in the production (the bottom graph in Figure E.17.1). SoG-Si available today contains practically every transition metal in concentrations between 3×10^{13} and 10^{16} cm^{-3}.

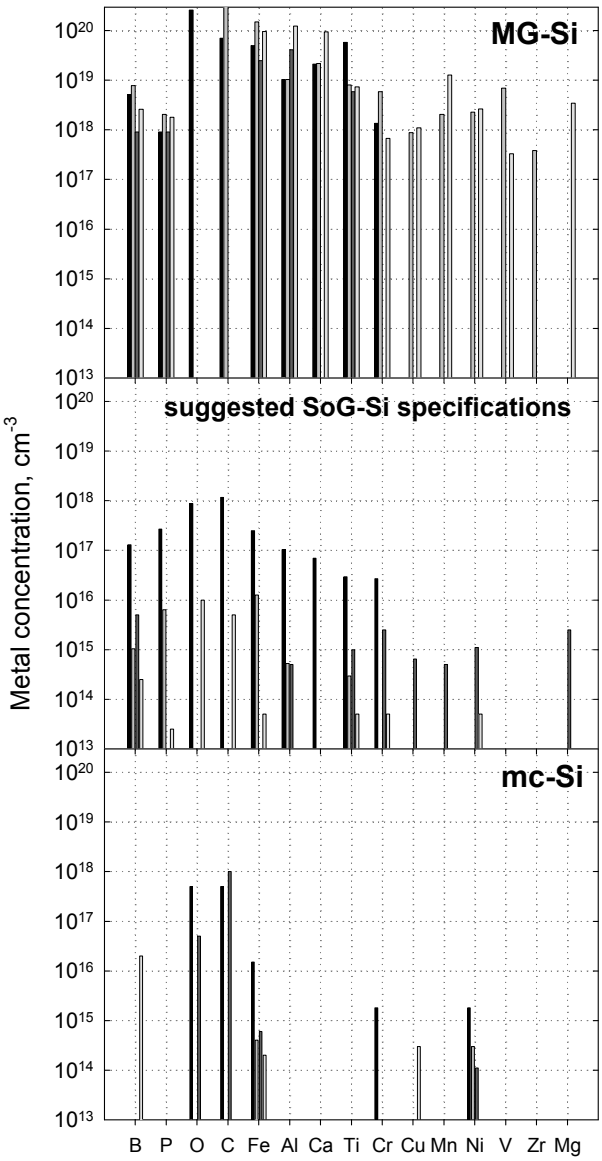

Figure E.17.1: Typical concentrations of impurities in metallurgical grade (the top graph), solar grade (the middle graph) and multicrystalline silicon solar cells that are currently in production (the bottom graph). The data points are from the references [26, 28, 61, 63, 83-87]. Not all sources provide data for all elements. Lack of bars on the plots does not always mean that this element was not present above the detection limit but rather that it was not tested.

This raises the question if the purity of SoG-Si as it is available today is sufficient to make cells that can compete on the market with the cells made of electronic grade silicon. The question lies primarily in concentration of transition metals because the maximum acceptable concentration of shallow dopants is well known, and because removal of metals usually cannot be accomplished in the same processing step with removal of boron or phosphorus.

Metals are known to severely affect the minority carrier diffusion length and solar cell efficiency. Figure E.17.2 presents data for interstitial iron and FeB pairs from [9], data for Cu from [88], and our unpublished data for Ni. The shaded area on the plot indicates the range of minority carrier diffusion lengths typically found in mc-Si solar cells. One can see that the

threshold concentration of interstitial iron acceptable for solar cells is around 2×10^{12} cm^{-3}. Cu and Ni can be tolerated in concentrations up to 10^{14} to 10^{16} cm^{-3}. This conclusion is in agreement with experimental studies of efficiency of solar cells made of intentionally contaminated CZ ingots by Davis et al. [47]. They showed that Cu is the least detrimental metal impurity, while heavier metals such as Ti or W can degrade cell performance in concentrations as low as 10^{11} – 10^{12} cm^{-3}.

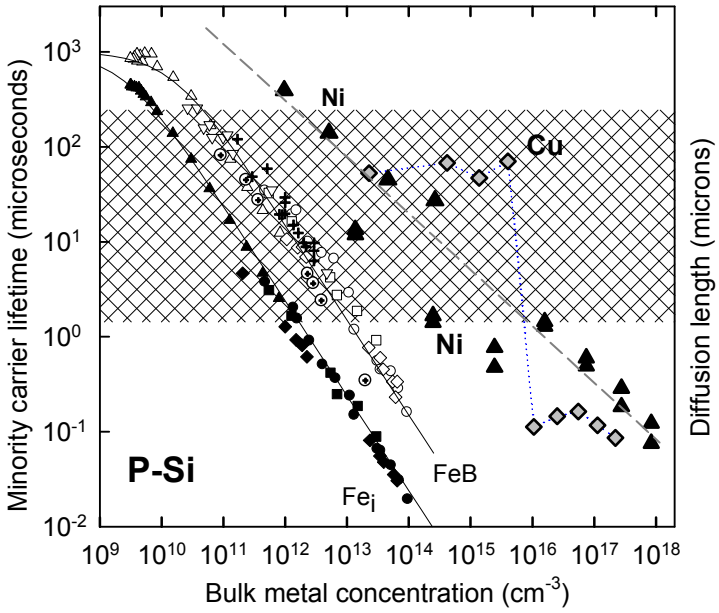

Figure E.17.2: Impact of iron, copper, and nickel on minority carrier diffusion length in single-crystalline silicon. The shaded area represents a typical range of minority carrier diffusion lengths in multicrystalline silicon solar cells.

Should one conclude that 10^{12} – 10^{13} cm^{-3} of transition metals is the limit which solar cells can tolerate? Surprisingly, neutron activation analyses [22, 26, 28] (see also this report) of several mc-Si materials used for commercial-scale manufacturing of solar cells revealed that these materials contain as much as 10^{15} cm^{-3} or iron, and 10^{12} to 10^{14} cm^{-3} of several other transition metals. If all these metals were homogeneously dissolved in the bulk in interstitial or substitutional state, the efficiency of solar cells would drop to unacceptably low levels. Our extensive x-ray microscopy studies using synchrotron radiation tools [17, 20, 89, 90], supported by this NREL contract in the past several years, revealed that, in fact, the majority of transition metals are found in metal precipitates or inclusions at grain boundaries or intragranular defects. In this state, the recombination activity per metal atom is reduced as compared to interstitially dissolved metals, and the tolerance of solar cells to metal contamination increases.

We discussed above that SoG-Si which is currently produced in research and development programs contains high concentration of transition metals. One possible approach to use this material for solar cell production is to add an additional purification step to reduce the metal content by two-three orders of magnitude. This would increase the cost of the silicon feedstock. An alternative approach is to gain a deeper understanding of the interaction between metals and with structural defects in mc-Si in order to defect-engineer metals into their least

recombination active state and to improve efficiency of their gettering. This approach could involve specially designed heat treatments, optimization of growth conditions to favor the formation of preferred types and densities of grain boundaries or dislocations, shifting the balance between silicon interstitials or vacancies in the desired direction, utilization of defect reactions between metals with the formation of complexes and mixed silicides [91], etc. Additionally, one could use the improved understanding of defect reactions of metals to improve the efficiency of gettering and hydrogen passivation. A combination of impurity defect engineering with improved techniques for purification of MG-Si could lead to implementation of SoG-Si into mass-scale production in the near future.

The importance of development of defect engineering techniques is emphasized by the fact that traditional gettering strategies for removal of metallic impurities during solar cell device processing are unlikely to be sufficient for solar-grade silicon because they are fundamentally limited by four physical realities of metals in multicrystalline silicon (mc-Si) solar cell material:

(1) *Limited segregation coefficient.* Firstly, the segregation coefficient for any gettering process is finite, determined by equilibrium solubilities of impurities in the bulk (mc-Si wafer) and boundary phases (gettering layers). Secondly, segregation gettering mechanisms such as phosphorus diffusion or aluminum backside gettering must compete for metals with structural defects within bulk mc-Si. Certain types of grain boundaries [92] and dislocations [93] also have high binding energies for metallic impurities, reducing the segregation coefficient and placing a fundamental upper limit on metal gettering effectiveness [4, 5].

(2) *Limited capacity of the gettering layer.* The capacity of a segregation gettering layer is fundamentally limited by its volume. The amount of metals removed from the bulk during segregation gettering is a function of the volume ratio of bulk to gettering layer, as well as the segregation coefficient, as described by

$$\frac{[\mathrm{M}]\,\text{in bulk after gettering}}{[\mathrm{M}]\,\text{in bulk before gettering}} \equiv \frac{c_{\mathrm{bulk}}}{c_{\mathrm{o}}} = \frac{c_{\mathrm{bulk}}}{\left[\dfrac{\left(c_{\mathrm{bulk}} \times d\right) + \left(c_{\mathrm{gett}} \times w\right)}{d}\right]} = \frac{1}{1 + \dfrac{k \times w}{d}}\ , \qquad (1)$$

where k is the segregation coefficient defined as $c_{\mathrm{gett}}/c_{\mathrm{bulk}}$, d is the volume [thickness] of the bulk, and w is the volume [thickness] of the gettering layer.

(3) *Kinetic limitations*: Limitations in impurity solubility and diffusivity retard the complete dissolution of large local concentrations of metals, such as precipitates and inclusions [3, 21]. Consequently, large metal-silicide precipitates can take up to several hours to dissolve at low to intermediate processing temperatures.

(4) *Competing demands of solar cell processing:* The depths and profiles of the pn-junction and the back surface field must be carefully controlled, to ensure good short- and long-wavelength response. Additionally, metallization firing must ensure low contact resistance, while avoiding shunting. Any gettering process employed during solar cell production must be mindful of the parameter space necessary for optimized solar cell processing.

F. Summary of Results Relevant to the Photovoltaic Community

Average metal content of solar cells. Neutron activation analysis was performed to determine the total metal content of solar-grade multicrystalline silicon. The dominant metal impurities were found to be Fe (6×10^{14} cm^{-3} to 1.5×10^{16} cm^{-3}, depending on the material), Ni (up to 1.8×10^{15} cm^{-3}), Co (1.7×10^{12} cm^{-3} to 9.7×10^{13} cm^{-3}), Mo (6.4×10^{12} cm^{-3} to 4.6×10^{13} cm^{-3}), and Cr (1.7×10^{12} cm^{-3} to 1.8×10^{15} cm^{-3}). Copper was also detected (less than 2.4×10^{14} cm^{-3}), but its concentration could not be accurately determined because of a very short decay time of the corresponding radioactive isotope. The total metal concentration of the wafers would be sufficient to decrease the average minority carrier diffusing length to several microns or less, if all metals were in the interstitial or substitutional state.

Metal content of good and bad regions. No systematic differences were found between the metal content of "good" and "bad" regions, except for a consistently higher gold concentration in "bad" regions. Some metals were even found in slightly higher concentration in the "good" regions than in the "bad" regions. This implies that the "good" and "bad" regions differ not by the amount of metals, but by their spatial distribution and by the recombination activity of clusters and point defects which these metals form.

Aluminum gettering of metals. We studied Al gettering of Cu in detail, determined segregation coefficient of Cu, and concluded that the efficiency of Al gettering is limited primarily by the capacitance of the gettering layer for metal impurities. Thicker Al layers could getter more metals, but this would increase costs and, in the case of slowly diffusing metals, would require long processing times.

Shunts and transition metals. We demonstrated that transition metal contamination is one of possible mechanisms of shunt formation. We observed precipitates of Ag and Ti at a shunt location in cast mc-Si cell, which indicated a possibility of process-induced shunt. Clusters of iron and copper were found near the current-collecting channels in RGS material. These channels are unique to RGS material grown under certain conditions and are known to have detrimental effect (lower fill-factor and open-circuit voltage) similar to shunting.

Chemical state and distribution of iron clusters in mc-Si. The iron-rich clusters analyzed in this study can be divided into two distinct groups: 1) Larger particles (diameter ≥ 1 μm) which are present in rather low spatial densities and are believed to be inclusions originating from foreign sources, e.g. the feedstock, growth surfaces, and/or production equipment. These inclusions are (a) accompanied by lesser amounts of other metals such as Cr, Ni, Mn, Ti, S, or Ca, suggestive of stainless steels or ceramics, and/or (b) in an oxidized chemical state, both indicators of foreign origins. 2) Smaller (dia. < 800 nm, typically < 100 nm) iron silicide precipitates, observed in much higher spatial densities and separated by as little as a few microns. Despite their small size, a large amount of iron (up to $10^{14\text{-}15}$ cm^{-3}) is estimated to be contained in these iron silicide nanoprecipitates, due to their homogeneous distribution and high spatial density along structural defects.

Chemical state and distribution of copper clusters in mc-Si. All Cu clusters observed in our experiments were copper-silicide; no copper-oxide or copper-silicate particles were observed.

Copper was shown to precipitate predominantly at extended defects such as grain boundaries and dislocations. The distribution of copper depends on the cooling rate (i.e., on the Cu supersaturation level).

Interaction of metals with oxygen and formation of gettering-resistant clusters. Thermodynamic considerations indicate that metals are unlikely to form complexes with oxygen dissolved in silicon wafers because the binding energy of oxygen to silicon is greater than that of oxygen to most transition metals. Particles in which metals were found in oxidized state were found in very low density and were concluded to be incompletely dissolved inclusions trapped from the melt. These inclusions are unlikely to have substantial impact on solar cell efficiency due to their low spatial density.

Segregation of metals at grain boundaries and structural defects. We obtained experimental evidence that iron aggregates at structural defects due to a combination of relaxation and segregation mechanisms. Similar effect has been earlier reported for copper. Segregation at grain boundaries and dislocations is likely to be one of the mechanisms of incorporation of high metal concentrations in mc-Si ingots from the melt.

Sources and pathways of metal contamination in solar cell materials. The chemical and elemental composition of large metal-rich clusters in mc-Si suggests that metal contamination originates from metal-rich particles or dissolved metals in the growth surfaces, feedstock, and/or production equipment. Large amounts of metals can be incorporated into mc-Si primarily via three mechanisms: (a) the inclusion of incompletely dissolved foreign metal-rich particles, (b) the direct precipitation of locally supersaturated metal at the solid-liquid interface in the vicinity of structural defects, and (c) the segregation of metals to structural defects. Once inside the crystal at elevated but decreasing temperatures, dissolved metals can form metal-silicide nanoprecipitates.

Silicon nitride crucible coating as a possible source of metal contamination. We analyzed several silicon nitride powders, including a powder used in solar cell manufacturing. The powders were shown to contain transition metal precipitates. Dissolution of silicon nitride coating into the melt, or diffusion of metals in silicon, can lead to contamination of the ingot. Indeed, a higher metal concentration was found in the areas adjacent to the crucible walls, and SiN precipitates were found in the upper part of the ingot, indicating that partial dissolution of the crucible indeed takes place.

Gettering of metals in solar cells. We demonstrated that short heat treatments may partially dissolve metal clusters and lead to a minority carrier diffusion length degradation within the grains. The majority of metal clusters observed in our studies are in the state of metal silicide which is relatively easy to dissolve. As suggested by Plekhanov and Tan, gettering may take a long time if metal solubility at the gettering temperature is much less than the total metal content of the wafer. Segregation coefficient of Cu in Al was found to be greater or equal than S(Cu in Al)/S(Cu in Si)= 2×10^3. The difficulties with gettering of metals in mc-Si appear to be primarily due to high metal content of mc-Si and limited capacity of the gettering layers. Due to the limited capacity of a standard 1-2 microns thick Al layer, only 90% to 95% of Cu can be removed from a

solar cell. Incomplete gettering may result in no visible improvement in minority carrier diffusion length.

Impact of the cooling rate. Our data indicate that cooling rate has a significant impact on precipitation behavior of Cu and Ni: they can either very selectively precipitate at certain locations at grain boundaries and oxygen precipitates, or evenly decorate all boundaries and dislocations. This implies that properly chosen heat treatments can be used to engineer the distribution of metal clusters in the samples.

Analysis of metal clusters in a wide variety of mc-Si materials. It was confirmed that while the density and spatial distribution of metal clusters depends on the feedstock quality and growth conditions, the chemical state and general trends in distribution of metal clusters are similar for all mc-Si materials. The differences between concentration and distribution of transition metals could be correlated with the feedstock quality, density and type of structural defects, and growth conditions.

Interactions between different transition metals in silicon. We observed that Fe, Cu, and Ni can not only precipitate in the same locations, but interact with each other chemically with the formation of mixed metal silicides. This finding may have implications for gettering of transition metals and their impact on minority carrier diffusion length.

Possible practical solutions for decreasing impact of metals on solar cells: the concept of defect engineering of metals in solar cells. Solar cells can tolerate much higher amounts of precipitated metals compared to interstitially/substitutionally dissolved metals in the lattice. The recombination properties of metals vary depending on their chemical or structural state and spatial distribution. The total metal content of mc-Si materials is typically so high that it is not feasible, due to the kinetic constraints and limited gettering layer capacity, to remove all these metals by gettering within a temperature cycle compatible with solar cell production cycle. One the other hand, instead of removing the metals from the cells it is sufficient to convert them to a less recombination efficient state. This approach was called defect engineering of transition metals in solar cells. Variation of the cooling rate of mc-Si samples with the same initial metal content was used to obtain proof of the principle: slowly cooled samples had low density of large metal precipitates and had 4 times higher minority carrier diffusion length than the quenched samples.

Quantitative XBIC technique was developed and applied to transition metal contaminated samples to demonstrate that minority carrier diffusion length is directly correlated to the local concentration of transition metals.

Interstital oxygen spatial distribution in the vicinity of grain boundaries was mapped with high spatial distribution. The measurements revealed that oxygen was homogeneously distributed.

Solar-grade silicon was compared, in terms of impurity concentration, with electronic-grade silicon and with metallurgical-grade silicon. It was shown that limitations of traditional gettering techniques require their combination with metal defect engineering to mitigate the impact of transition metals in solar-grade Si.

G. Acknowledgements

This study would not be possible without fruitful collaboration with our colleagues from NREL (T. F. Ciszek, R. Mcconnell, R. Matson, B. Sopori), Fraunhofer ISE (C. Ballif, S. Peters, J. Isenberg, W. Warta, S. Riepe, M. Rinio, S. Rein, S. Glunz, and R. Schindler), Georgia Tech (A. Upadhyaya, M.Sheoran, A.Rohatgi), University of Konstanz (G. Hahn), Max Planck Institute for Microstructure Physics in Halle (O. Breitenstein, J.-P. Rakotoniaina), University of Leipzig (M. Heuer), BP Solar (D. W. Cunningham), Evergreen Solar (A. Gabor), GE Energy (formerly Astropower) (R. Jonczyk), RWE Schott Solar (J. Kalejs), Sumitomo Mitsibushi Silicon (W.Huber) as well as staff scientists from the Advanced Light Source (M. A. Marcus, A. C. Thompson), Advanced Photon Source (B. Lai, Z. Cai), and LBNL Nuclear Physics Division (R. J. Mcdonald and A. R. Smith). Contributions of O. F. Vyvenko, H. Hieslmair, and S. A. McHugo were instrumental for development of experimental approaches used in this study and for determining the directions of research. Last but not least we would like to thank D. Macdonald and A. Cuevas (Australian National University), S. K. Estreicher (Texas Tech), W. Schröter (University of Göttingen), O.Breitenstein (MPI Halle), and our present and past group members, M. Pickett, P. Zhang, H. Väinölä, S.A. McHugo, and D. Schleuning, for numerous discussions. T. Buonassisi would like to thank the DAAD for a summer 2004 scholarship which supported his trip to Germany to discuss with work with our German colleagues. The operations of the Advanced Light Source at Lawrence Berkeley National Laboratory are supported by the Director, Office of Science, Office of Basic Energy Sciences, Materials Sciences Division, of the US Department of Energy under Contract No. DEAC03-76SF00098. Use of the Advanced Photon Source was supported by the US Department of Energy, Office of Science, Office of Basic Energy Sciences, under Contract No. W-31-109-ENG-38.

H. References

1. M. A. Marcus and J. E. Bower, *J. Appl. Phys.* **82**, 3821 (1997).
2. S. A. McHugo, A. C. Thompson, G. Lamble, C. Flink, and E. R. Weber, *Physica B* **273-274**, 371 (1999).
3. P. S. Plekhanov, R. Gafiteanu, U. M. Gosele, and T. Y. Tan, *J. Appl. Phys.* **86**, 2453 (1999).
4. R. C. Dorward and J. S. Kirkaldy, *J. Mat. Sci.* **3**, 502 (1968).
5. M. Kittler and W. Seifert, *Solid State Phenom.* **95-96**, 197 (2004).
6. S. A. McHugo, A. Mohammed, A. C. Thompson, B. Lai, and Z. Cai, *J. Appl. Phys.* **91**, 6396 (2002).
7. N. Li, H. Li, and T. Y. Tan, in *14th workshop on crystalline silicon solar cells and modules: materials and processes,* B. L. Sopori, Editor, p. 238, NREL, Golden, CO (2004).
8. S. A. McHugo, A. C. Thompson, A. Mohammed, G. Lamble, I. Perichaud, S. Martinuzzi, M. Werner, M. Rinio, W. Koch, H. U. Hoefs, and C. Haessler, *J. Appl. Phys.* **89**, 4282 (2001).
9. A. A. Istratov, H. Hieslmair, and E. R. Weber, *Appl. Phys. A* **70**, 489 (2000).
10. A. Fedotov, B. Evtody, L. Fionova, J. Iliashuk, E. Katz, and L. Poljak, *J. Cryst. Growth* **104**, 186 (1990).
11. A. Fedotov, B. Evtodyi, L. Fionova, Y. Ilyashuk, E. Katz, and L. Polyak, *phys. stat. sol. (a)* **119**, 523 (1990).
12. P. S. Ravishankar, J. P. Dismukes, and W. R. Wilcox, *J. Cryst. Growth* **71**, 579 (1985).
13. J. P. Kalejs, B. Bathey, and C. Dube, *J. Cryst. Growth* **109**, 174 (1991).
14. S. Mahajan and K. S. S. Harsha, *Principles of growth and processing of semiconductors*, McGraw-Hill, Boston (1999).
15. J. Lagowski, P. Edelman, M. Dexter, and W. Henley, *Semicond. Sci. Technol.* **7**, A185 (1992).
16. D. K. Schroder, *Semiconductor material and device characterization*, 2nd Ed., Wiley, New York (1998).
17. T. Buonassisi, M. A. Marcus, A. A. Istratov, M. Heuer, T. F. Ciszek, B. Lai, C. Zhonghou, and E. R. Weber, *J. Appl. Phys.* **97**, 63503 (2005).
18. T. Y. Tan, E. E. Garnder, and W. K. Tice, *Appl. Phys. Lett.* **30**, 175 (1977).
19. J. Lu, M. Wagener, G. Rozgonyi, J. Rand, and R. Jonczyk, *J. Appl. Phys.* **94**, 140 (2003).
20. T. Buonassisi, A. A. Istratov, M. Heuer, M. A. Marcus, R. Jonczyk, J. Isenberg, B. Lai, C. Zhonghou, S. Heald, W. Warta, R. Schindler, G. Willeke, and E. R. Weber, *J. Appl. Phys.* **97**, 74901 (2005).
21. T. Buonassisi, A. A. Istratov, S. Peters, C. Ballif, J. Isenberg, S. Riepe, W. Warta, R. Schindler, G. Willeke, Z. Cai, B. Lai, and E. R. Weber, *Appl. Phys. Lett.* **87**, 121918 (2005).
22. D. Macdonald, A. Cuevas, A. Kinomura, and Y. Nakano, in *29th Photovoltaic Specialists Conference*, p. 285, IEEE, New Orleans, LA (2002).
23. S. Binetti, M. Acciarri, C. Savigni, A. Brianza, S. Pizzini, and A. Musinu, *in* "Elsevier. Materials Science & Engineering B (Solid-State Materials for Advanced Technology), vol.36, no.1-3, Jan. 1996, pp. 68-72. Switzerland.").
24. C. Ballif, S. Peters, C. Borchert, C. Ндssler, J. Isenberg, R. Schindler, W. Warta, and G. Willeke, *in* "17th European Photovoltaics Specialists Conference", p. 1818, Munich, Germany (2001).

25. O. F. Vyvenko, T. Buonassisi, A. A. Istratov, E. R. Weber, M. Kittler, and W. Seifert, *J. Phys.: Cond. Matter* **14**, 13079 (2002).
26. A. A. Istratov, T. Buonassisi, R. J. McDonald, A. R. Smith, R. Schindler, J. A. Rand, J. P. Kalejs, and E. R. Weber, *J. Appl. Phys.* **94**, 6552 (2003).
27. A. R. Smith, R. J. McDonald, H. Manini, D. L. Hurley, E. B. Norman, M. C. Vella, and R. W. Odom, *J. Electrochem. Soc.* **143**, 339 (1996).
28. D. Macdonald, A. Cuevas, A. Kinomura, Y. Nakano, and L. J. Geerligs, *J. Appl. Phys.* **97**, 33523 (2005).
29. H. Gottschalk, *phys. stat. sol. B* **222**, 353 (2000).
30. T. F. Ciszek and T. H. Wang, *J. Cryst. Growth* **237-239**, 1685 (2002).
31. E. R. Weber, *Appl. Phys. A* **30**, 1 (1983).
32. J. J. Rehr and R. C. Albers, *Rev. Mod. Phys. (USA)* **72**, 621 (2000).
33. A. L. Ankudinov, B. Ravel, J. J. Rehr, and S. D. Conradson, *Phys. Rev. B* **58**, 7565 (1998).
34. M. Newville, *J. Synchrotron Radiation* **8**, 322 (2001).
35. S. K. Estreicher, *Phys. Rev. B* **60**, 5375 (1999).
36. K. J. Solberg, *Acta Crystallographica A* **A34**, 684 (1978).
37. G. A. Rozgonyi, J. Lu, R. Zhang, J. Rand, and R. Jonczyk, *in* "Balaban Publishers; Scitec Publications. Diffusion and Defect Data Part B (Solid State Phenomena), vol.95-96, 2004, pp. 211-16. Switzerland.").
38. T. S. Fell and P. R. Wilshaw, *Journal de Physique IV (Colloque)* **1**, 211 (1991).
39. M. Kittler, C. Ulhaq-Bouillet, and V. Higgs, *J. Appl. Phys.* **78**, 4573 (1995).
40. D. M. Lee and G. A. Rozgonyi, *Appl. Phys. Lett.* **65**, 350 (1994).
41. N. V. Abrosimov, A. V. Bazhenov, and V. A. Tatarchenko, *J. Cryst. Growth* **82**, 203 (1987).
42. A. Ihlal, R. Rizk, and O. B. M. H. Duparc, *J. Appl. Phys.* **80**, 2665 (1996).
43. J. Chen, T. Sekiguchi, D. Yang, F. Yin, K. Kido, and S. Tsurekawa, *J. Appl. Phys.* **96**, 5490 (2004).
44. A. A. Istratov, W. Huber, and E. R. Weber, *Applied Physcs Letters* **85**, 4472 (2004).
45. A. Rohatgi, J. R. Davis, R. H. Hopkins, P. Rai-Choudhury, and P. G. McMullin, *Sol. St. Electron.* **23**, 415 (1980).
46. K. Graff, *Metal impurities in silicon-device fabrication*, 2 Ed., Springer, Berlin (2001).
47. J. R. Davis, A. Rohatgi, R. H. Hopkins, P. D. Blais, P. Rai-Choudhury, J. R. McCormic, and H. C. Mollenkopf, *IEEE Trans. Electron. Dev.* **ED-27**, 677 (1980).
48. S. Pizzini, L. Bigoni, M. Beghi, and C. Chemelli, *J. Electrochem. Soc.* **133**, 2363 (1986).
49. J. Chen, D. Yang, Z. Xi, and T. Sekiguchi, *J. Appl. Phys.* **97**, 33701 (2005).
50. C. T. Tsai, *J. Cryst. Growth* **113**, 499 (1991).
51. D. Franke, T. Rettelbach, C. Hassler, W. Koch, and A. Muller, *Solar Energy Mat. Solar Cells* **72**, 83 (2002).
52. I. Steinbach, M. Apel, T. Rettelbach, and D. Franke, *Solar Energy Mat. Solar Cells* **72**, 59 (2002).
53. J. P. Kalejs, *Solid State Phenom.* **95-96**, 159 (2004).
54. J. P. Kalejs, *Solar Energy Materials & Solar Cells* **72**, 139 (2002).
55. S. A. McHugo, H. Hieslmair, and E. R. Weber, *Appl. Phys. A* **64**, 127 (1997).
56. S. Pizzini, *phys. stat. sol. (a)* **171**, 123 (1999).
57. T. Buonassisi, A. A. Istratov, M. A. Marcus, B. Lai, Z. Cai, S. M. Heald, and E. R. Weber, *Nature Materials* **4**, 676 (2005).
58. D. R. Uhlmann, B. Chalmers, and K. A. Jackson, *J. Appl. Phys.* **35**, 2986 (1964).

59. I. Perichaud, S. Martinuzzi, and F. Durand, *Solar Energy Mat. Solar Cells* **72**, 101 (2002).
60. A. K. Soiland, E. J. Ovrelid, T. A. Engh, O. Lohne, J. K. Tuset, and O. Gjerstad, *Mater. Sci. Semicond. Process.* **7**, 39 (2004).
61. B. R. Bathey and M. C. Cretella, *J. Mat. Sci.* **17**, 3077 (1982).
62. S. Pizzini, *Solar Energy Materials* **6**, 253 (1982).
63. T. F. Ciszek, T. H. Wang, M. R. Page, R. E. Bauer, and M. D. Landry, *in* "Conference Record of the Twenty-Ninth IEEE Photovoltaic Specialists Conference 2002 (Cat. No.02CH37361)." p. 206 IEEE, Piscataway, NJ, USA. (2002).
64. N. S. K. Prasad, *in* "Sun: Mankind's future source of energy. Pergamon." (F. de Winter and M. Cox, Editors), Vol. 2, p. 772 Oxford, UK (1978).
65. W. C. Breneman, E. G. Farrier, and H. Morihara, *in* "Thirteenth IEEE Photovoltaic Specialists Conference-1978. IEEE. 1978, pp. 339-43. New York, NY, USA." p. 339 IEEE, New York, NY, USA. (1978).
66. M. F. Browning, J. M. Blocher, Jr., W. J. Wilson, and D. C. Carmichael, *in* "Twelfth IEEE Photovoltaic Specialists Conference 1976. IEEE. 1976, pp. 130-6. New York, NY, USA." p. 130 IEEE, New York, NY, USA (1976).
67. V. D. Dosaj and L. P. Hunt, US Patent 4247528 (1981)
68. H. Aulich, K.-H. Eisenrith, F. W. Schulze, and H.-P. Urbach, US Patent 4460556 (1984)
69. J. A. Amick, J. P. Dismukes, R. W. Francis, L. P. Hunt, P. S. Ravishankar, M. Schneider, K. Matthei, R. Sylvain, K. Larsen, and A. Schei, *J. Electrochem. Soc.* **132**, 339 (1985).
70. H. A. Aulich, F. W. Schulz, and J. G. Grabmaier, *Siemens Forschungs- und Entwicklungsberichte* **11**, 332 (1982).
71. D. E. Claeys, H. D. Hecht, and K. A. Munzer, *in* "Sixth E.C. Photovoltaic Solar Energy Conference." (W. Palz and F. C. Treble, Editors), p. 1021 Reidel, Dordrecht, Netherlands (1985).
72. L. P. Hunt and V. D. Dosaj, *in* "Commission of the European Communities, 2nd E.C. Photovoltaic Solar Energy Conference." (R. Van Overstraeten and W. Palz, Editors), p. 98 Reidel, Dordrecht, Netherlands. (1979).
73. L. P. Hunt, V. D. Dosaj, J. R. McCormick, and A. W. Rauchholz, *in* "Thirteenth IEEE Photovoltaic Specialists Conference", p. 333 IEEE, New York, NY, USA (1978).
74. L. P. Hunt, V. D. Dosaj, J. R. McCormick, and L. D. Crossman, *in* "Twelfth IEEE Photovoltaic Specialists Conference 1976. IEEE. 1976, pp. 125-9. New York, NY, USA." p. 125 IEEE, New York, NY, USA (1976).
75. W. V. Gampel, US Patent 2972521 (1961)
76. E. Bildl, J. Dietl, R. Baueregger, and D. Seifert, US Patent 4588571 (1984)
77. C. E. Norman, E. M. Absi, and R. E. Thomas, *Can. J. Phys.* **63**, 859 (1985).
78. T. L. Chu, G. A. van der Leeden, and H. I. Yoo, *J. Electrochem. Soc.* **125**, 661 (1978).
79. C. P. Khattak, D. B. Joyce, and F. Schmid, in *Conference Record of the Twenty-Ninth IEEE Photovoltaic Specialists Conference 2002*, p. 364, IEEE, Piscataway, NJ, USA (2002).
80. T. L. Chu, S. S. Chu, R. W. Kelm, Jr., and G. W. Wakefield, *J. Electrochem. Soc.* **125**, 595 (1978).
81. K. Morita, *in* "Proceedings of Modeling, Control and Optimization in Ferrous and Nonferrous Industry Symposium" (F. Kongoli, B. G. Thomas, and K. Sawamiphakdi, Editors), p. 49 Minerals, Metals & Mater. Soc., Warrendale, PA, USA. (2003).
82. P. S. Kotval and H. B. Strock, US Patent 4193975 (1980)
83. D. Sarti and R. Einhaus, *Solar Energy Mat. Solar Cells* **72**, 27 (2002).

84. N. Yuge, M. Abe, K. Hanazawa, H. Baba, N. Nakamura, Y. Kato, Y. Sakaguchi, S. Hiwasa, and F. Aratani, *Progress in Photovoltaics: Research & Applications* **9**, 203 (2001).
85. S. Pizzini, *Journal of Power Sources* **11**, 115 (1984).
86. G. C. Jain, S. N. Singh, and R. Kishore, *Sol. Cells (Switzerland)* **6**, 357 (1982).
87. M. G. Mauk, J. A. Rand, R. Jonczyk, R. B. Hall, and A. M. Barnett, *in* "Proceedings of 3rd World Conference on Photovoltaic Energy Conversion (IEEE Cat. No.03CH37497). Arisumi Printing Inc. Part Vol.1, 2003, pp. 939-42 Vol.1. Japan, Japan." (K. Kurokawa, L. L. Kazmerski, B. McNelis, M. Yamaguchi, C. Wronski, and W. C. Sinke, Editors), Vol. 1, p. 939 Arisumi Printing Inc., Japan (2003).
88. R. Sachdeva, *Appl. Phys. Lett.* **79**, 2937 (2001).
89. T. Buonassisi, O. F. Vyvenko, I. A.A., E. R. Weber, G. Hahn, D. Sontag, J. P. Rakotoniaina, O. Breitenstein, J. Isenberg, and R. Schindler, *J. Appl. Phys.* **95**, 1556 (2004).
90. T. Buonassisi, A. A. Istratov, M. D. Pickett, M. Heuer, J. Kalejs, Z. Cai, B. Lai, M. A. Marcus, T. F. Ciszek, and E. R. Weber, *Progress in Photovoltaics: Research & Applications*, in print (2005).
91. M. Heuer, T. Buonassisi, M. A. Marcus, A. A. Istratov, M. D. Pickett, and E. R. Weber, *Phys. Rev. B*, in print (2006).
92. T. Buonassisi, A. A. Istratov, M. D. Pickett, M. A. Marcus, T. F. Ciszek, and E. R. Weber, *Appl. Phys. Lett.* **89**, 42102 (2006).
93. A. Bentzen, A. Holt, R. Kopecek, G. Stokkan, J. S. Christensen, and B. G. Svensson, *J. Appl. Phys.* **99**, 93509 (2006).

REPORT DOCUMENTATION PAGE

Form Approved
OMB No. 0704-0188

PLEASE DO NOT RETURN YOUR FORM TO THE ABOVE ORGANIZATION.

1. REPORT DATE *(DD-MM-YYYY)*	2. REPORT TYPE	3. DATES COVERED *(From - To)*
November 2007	Subcontract Report	1 January 2002 – 30 September 2006

4. TITLE AND SUBTITLE
Efficiency Improvement of Crystalline Solar Cells: Final Subcontract Report, 1 January 2002 – 30 September 2006

5a. CONTRACT NUMBER
DE-AC36-99-GO10337

5b. GRANT NUMBER

5c. PROGRAM ELEMENT NUMBER

6. AUTHOR(S)
E.R. Weber

5d. PROJECT NUMBER
NREL/SR-520-42323

5e. TASK NUMBER
PVA72101

5f. WORK UNIT NUMBER

7. PERFORMING ORGANIZATION NAME(S) AND ADDRESS(ES)
University of California, Berkeley
336 Sprout Hall
Berkeley, California 94720

8. PERFORMING ORGANIZATION REPORT NUMBER
AAT-2-31605-03

9. SPONSORING/MONITORING AGENCY NAME(S) AND ADDRESS(ES)
National Renewable Energy Laboratory
1617 Cole Blvd.
Golden, CO 80401-3393

10. SPONSOR/MONITOR'S ACRONYM(S)
NREL

11. SPONSORING/MONITORING AGENCY REPORT NUMBER
NREL/SR-520-42323

12. DISTRIBUTION AVAILABILITY STATEMENT
National Technical Information Service
U.S. Department of Commerce
5285 Port Royal Road
Springfield, VA 22161

13. SUPPLEMENTARY NOTES
NREL Technical Monitor: Richard Matson/Fannie Posey-Eddy

14. ABSTRACT *(Maximum 200 Words)*
This report describes the University of California, Berkley's study to gain a fundamental physical understanding of the transition metal related defects in PV-grade multicrystalline silicon by elucidating the pathways of their introduction into solar cells, their chemical state and distribution within mc-Si, their interaction with structural defects, and to assess the possibility of reducing detrimental impact of these defect clusters on cell performance via defect engineering.

15. SUBJECT TERMS
PV; silicon; mc-Si; aluminum gettering; lattice; metals; thermal stability; solar cells; ingot grown; clusters; low cost; high-purity; structural defects; optical microscope image;

16. SECURITY CLASSIFICATION OF:			17. LIMITATION OF ABSTRACT	18. NUMBER OF PAGES	19a. NAME OF RESPONSIBLE PERSON
a. REPORT	b. ABSTRACT	c. THIS PAGE			19b. TELEPHONE NUMBER (*Include area code*)
Unclassified	Unclassified	Unclassified	UL		

Standard Form 298 (Rev. 8/98)
Prescribed by ANSI Std. Z39.18